Final Report
August 1, 2006 – May 31, 2008

SECA COAL-BASED SYSTEMS PROGRAM

DOE/NETL Cooperative Agreement
DE-FC26-05NT42614

Matthew J. Alinger
Principal Investigator
518-387-5124 (telephone)
518-387-5576 (fax)

Submitted to
United States Department of Energy
National Energy Technology Laboratory
Morgantown, WV

August 2009

GE Global Research
Niskayuna, NY 12309-1027

DISCLAIMER

TABLE OF CONTENTS

EXECUTIVE SUMMARY

This report summarizes the progress made during the August 1, 2006 - May 31, 2008 award period under Cooperative Agreement DE-FC26-05NT42614 for the U. S. Department of Energy/National Energy Technology Laboratory (USDOE/NETL) entitled "SECA Coal Based Systems". The initial overall objective of this program was to design, develop, and demonstrate multi-MW integrated gasification fuel cell (IGFC) power plants with >50% overall efficiency from coal (HHV) to AC power. The focus of the program was to develop low-cost, high performance, modular solid oxide fuel cell (SOFC) technology to support coal gas IGFC power systems. After a detailed GE internal review of the SOFC technology, the program was de-scoped at GE's request. The primary objective of this program was then focused on developing a performance degradation mitigation path for high performing, cost-effective solid oxide fuel cells (SOFCs). Highlights of the main technical activities conducted during this award period are summarized below:

SOFC system development and design

- A cost of electricity (CoE) model has been developed for stationary SOFC systems and used to evaluate the effect of system size on the allocation for SOFC stack cost. Initial results suggest that system sizes >20-50 MW are required in order to compete successfully with incumbent combined cycle gas turbine (CCGT) technology.

- Two concepts were selected as the baseline and alternative baseline: (i) Baseline (BL): Radiant Syngas Cooler (RSC), CO_2 isolation after SOFC, once thru syngas (ii) Alternative Baseline (ABL): RSC, CO_2 removal before SOFC.

- For the BL system without CO_2 isolation, the overall efficiency is estimated to be about 50.4%. In this system, the largest element is the SOFC producer at about 31% of the coal HHV; the gas turbine (GT) and steam turbine (ST) produce 14% and 11% of the coal HHV. The largest parasitic consumption is attributed to the oxygen generation and compression for a total of about 5% of the coal HHV. In order to down-select, a Pugh Matrix was utilized with the identified criteria. The ABL was selected as the baseline for the IGFC system concept. A preliminary model result for the IGFC at 0.8 V, 150 C air temperature rise, and 80% fuel utilization indicates an efficiency of 43.1%.

- The natural gas hybrid system concept includes multiple SOFC stacks with a steam reforming fuel processor, a GT, a cathode recycle compressor, an anode recycle ejector, a recuperator, an inverter and other components. Natural gas is usually provided pressurized and it is used to drive the anode recycle ejector. A heat recovery steam generator

(HRSG)/ST is added to produce power from the waste heat of the hybrid system exhaust. Based on certain assumptions, the SOFC hybrid and SOFC combined cycle (SOFC CC) system efficiencies are 65.8% and 69.8% respectively. The effect of stack operating parameters (operating parameters are pressure, temperature and stack temperature gradient, cell voltage, fuel utilization, leakage rate and percentage of internal reforming) on hybrid system performance was analyzed.

Stack technology development and design

- During this award, work on tape calendering process was focused on two main areas, rolling process modeling and simulations and sintering yield improvements. For rolling process, the results are summarized below:

    - The current green materials, without any composition modification, have good visco-plasticity behavior when the production temperature (> 60 °C) is higher than the glass transition temperatures; such behavior is very importance for low cost and high volume production of cell sheets.
    - The proposed continuous rolling process is feasible for low cost and high volume production of SOFC cells.
    - The developed finite element, transient, fully-coupled thermal and stress model (ABAQUS Explicit) includes all the physics in rolling.
    - From the work that has been done to date on the sintering yield the following conclusions can be drawn:
    - The current cost model uses a sintering yield of 64% as a baseline. From the analysis of the data it appears that this can be achieved, and even increased to a by improving temperature uniformity in the furnace and by eliminating the use of PAL3 rework in the bilayers or remedying the root cause of the failures related to recycled material.

- The deposited YSZ mechanical properties were characterized for the first time using a four point bending test.

- A number of atmospheric plasma sprayed (APS) cells were tested during this reporting period. These were nominal 4 inch cells: from AFF-series, T-series, and MR-series. High fuel utilization (>80%) and excellent power density (up to 510 mW/cm2 at 0.7V) were observed for AFF series cells.

- During this award, validation of the SOFC 2D model was explored on the following cases: Case1: Validation: SOFC-2D vs. a selected publish work, Case 2: Effect of Inlet Temperature, Case 3: Effect of Internal Reforming.

- Experiments were conducted to examine the evolution of glass due to reaction between glass seals and the interconnect material. The formation

of $BaCrO_4$ was observed. This formation eventually results in a separation between the sealing glass and interconnect due to the stress related to CTE mismatch and compromises the interface.

System and stack demonstration

- A new 5 kW SECA prototype with improved/modified design (referred to as NETL prototype) was built and tested during this reporting period. A major design change in this prototype was the use of a single stack instead of 4 stacks as in the previous system.
- A number of tests were conducted before the so-called commissioning test (Gen 2 system test) including component tests, cold tests, hot tests, and Gen 1 system test (system test with a short stack).
- A plan for the commissioning test was developed. The system was successfully tested and shipped to NETL in September 2006 for validation testing.
- The system achieved a DC efficiency of 49.6% under the following conditions:
    - Fuel utilization of 79.5%
    - Current of 112.6 A (184 mA/cm2)
    - Average cell voltage of 0.783 V
    - Gross DC power of 3.52 kW (144 mW/cm2)
    - Net DC power of 3.27 kW
- The system achieved a net DC power of 5.62 kW under the following conditions:
    - Fuel utilization of 63.7%
    - Current of 242.2 A (395 mA/cm2)
    - Average cell voltage of 0.639 V
    - Gross DC power of 6.11 kW (249 mW/cm2)
    - DC efficiency of 32%

Manufacturing downselect

- A down selection of the manufacturing technology process was performed in November 2006. This process reviewed a sintering and a deposition approach to manufacture solid oxide fuel cells. A multidisciplinary committee was formed to assess current and projected risk of each technology and recommend a path forward.
    - The committee assessment results indicated that in both cases, assuming technical success of the program, no significant differentiation between the manufacturing approaches could be identified.
    - The major risks related to SOFC technology development are not related to cell fabrication, but are related to the capability of the technology to meet degradation and performance metrics compatible with the cost model assumptions.

- As such, the SOFC technical development redirected focus on material activities to address the degradation challenge of high performance SOFC material sets.

Experimental capabilities

- During the course of this program, significant improvements were made in regard to laboratory testing capabilities.
  - A 2x2" alumina test vehicle for controlled measurement of cell performance and degradation under realistic conditions was designed, built and used for testing.
  - An off-line ASR measurement test was designed, experimentally verified and used as a tool for direct measurement of contact resistance change over time.
  - In addition, a test vehicle to directly measure anode-side ohmic degradation, under realistic SOFC operating conditions, has been designed and built and used.
  - Several modifications to the button cell 6-gun rigs were implemented:
    - Replacing the stainless steel air supply lines in the furnace hot zones with quartz tubing to minimize potential chromium contamination.
    - Cell weights were made from a ceramic.
  - Modifications to the humidification system were performed to avoid water condensation in the fuel lines.
  - The voltage and current leads to the cells were shortened and shielded to improve AC impedance spectroscopy.

Degradation mitigation

- Button cell and 25cm^2 testing indicate that, in order to maintain high performance, LSCF cathode stability is critical.
  - Test results on the stabilized cathode indicate dramatic improvement in degradation behavior.

- Contact resistance testing has verified the ohmic stability of the LSC bond paste as well as the LSCF cathode material over extended time at 800^{o}C under a 0.5A/cm^2 load with gold current collectors.

- In addition, contact resistance measurement has confirmed that the use of MCO coated GE-13L stainless steel in contact with LSC results in very low ohmic degradation.

- Degradation tests performed using the 25 cm^2 ceramic test vehicle were performed on sintered anode supported cells with LSCF based cathodes.

- The lowest degradation test had a very high initial performance at 0.7V of 1.34 W/cm^2 with a corresponding ASR of 143.0 mΩ-cm^2.
- Degradation of the cell yielded a time average linear ASR degradation rate of 15 mΩ-cm^2/1000h with a corresponding power density degradation rate of 2.2%/1000h.
- Repeat tests of this configuration were reasonable, but not as successful.
    - The greater degradation rates of these cells is attributed to variable quality Mn,Co spinel coating on the cathode interconnect.

1 INTRODUCTION

This report summarizes the progress made during the August 1, 2006 - May 31, 2008 award period under Cooperative Agreement DE-FC26-05NT42614 for the U. S. Department of Energy/National Energy Technology Laboratory (USDOE/NETL) entitled "SECA Coal Based Systems". The initial overall objective of this program was to design, develop, and demonstrate multi-MW integrated gasification fuel cell (IGFC) power plants with >50% overall efficiency from coal (HHV) to AC power. The focus of the program was to develop low-cost, high performance, modular solid oxide fuel cell (SOFC) technology to support coal gas IGFC power systems. After a detailed GE internal review of the SOFC technology, the program was de-scoped at GE's request. The primary objective of this program was then focused on developing a performance degradation mitigation path for high performing, cost-effective solid oxide fuel cells (SOFCs).

2 PROGRAM OVERVIEW

There were two initial major objectives in this program. These were:

1. Develop and optimize a design of a >100 MWe integrated gasification fuel cell (IGFC) power plant;
2. Resolve identified barrier issues concerning the long-term economic performance of SOFC.

The program focused on designing and cost estimating the IGFC system and resolving technical and economic barrier issues relating to SOFC. In doing so, manufacturing options for SOFC cells were evaluated, options for constructing stacks based upon various cell configurations identified, and key performance characteristics were identified. Key factors affecting SOFC performance degradation for cells in contact with metallic interconnects were be studied and a fundamental understanding of associated mechanisms was developed using a fixed materials set. Experiments and modeling were carried out to identify key processes/steps affecting cell performance degradation under SOFC operating conditions. Interfacial microstructural and elemental changes were characterized, and their relationships to observed degradation identified. Mitigation strategies, including innovative coatings and bond layers, were developed, evaluated and down-selected to improve degradation rates. Focus was on microstructural stabilization and minimization of the ASR contribution from Cr_2O_3 scale growth and other interactions at electrode/interconnect interfaces evaluated during electrochemical testing and advanced microstructural characterization. Novel long-term and accelerated testing techniques were developed and conducted under standard operating conditions to demonstrate capability to meet targeted degradation rates.

3 RESULTS AND DISCUSSION

3.1 SOFC system development and design

3.1.1 Product roadmap and initial selection

Significant analysis has been performed and previously reported by GE regarding the optimal market and strategy for SOFC power systems. Some market analysis is presented in Table 3.1. Results indicate that central power generation is the best market to target long-term, including generation from natural gas and especially coal. This result is consistent with the objective of this program, to design a coal-based central generation power plant based on SOFC technology.

Table 3.1 Market analysis for SOFC power systems

	GenCo		DisCo	Industrial Energy User
Fuel	NG	Coal	NG	NG
Mode	85% Load Factor	85% Load Factor	70% Load Factor	>80% Load Factor
Incumbent Technology	CCGT	IGCC & PC	Small GT & Recip	Grid, Recip, Small GT
Emissions Benefit	>20% CO2	>20% CO2 100% NOx, SOx	~45% CO2	20% CO2 100 NOx, SOx
Relative Opportunity Size	3x	> 20x	1x	
Barriers	Adoption of New Technology	Adoption of New Technology	"New" Application & Technology	Interconnection & Technology Adoption
Enablers	GHG emissions regulations/trading	GHG emissions regulations/trading	Technology Validation Regulatory	Net Metering Standards

A cost of electricity (CoE) model has been developed for stationary SOFC systems and used to evaluate the effect of system size on the allocation for SOFC stack cost. This model is being refined with improved cost and reliability data on all system components, but initial results suggest that system sizes >20-50 MW are required in order to compete successfully with incumbent combined cycle gas turbine (CCGT) technology (see Figure 3.1). The stack cost allocation, unsurprisingly, continues to increase with system size, as benefits of scale accrue in the non-stack system components (gas turbine, etc.). As a result, the end products envisioned by GE are quite large, on the order of 100's of MW, consistent with the size of incumbent technology and with the needs of coal gasification.

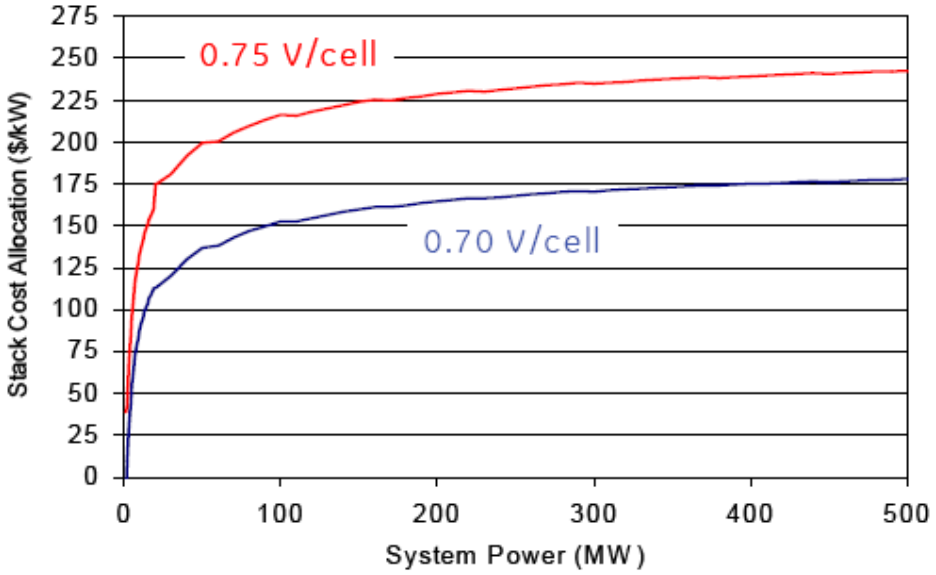

Figure 3.1 Results of CoE analysis, indicating SOFC stack cost allocation as a function of system power. Above ~20 MW system size, stack allocations exceed $175/kW, considered an absolute minimum for actual stack cost.

The strategy and roadmap for moving from kW scale demos to MW-scale products is still under development. In general, the plan is to develop small- and intermediate-scale systems, either as demo systems or entry-level products in the 1-50MW range. These products should use the full-scale building-block stack (estimated to be between 500kW and 1MW in power) and the same stack module architecture as the full-size systems, minimizing the need to redesign the stack subsystem as system scale increases. Since coal systems make little economic sense at such small sizes, it is expected that these systems will operate on natural gas. For this reason, effort is being expended on this program to design and analyze these intermediate systems as well as the full-scale IGFC system.

3.1.2 IGFC system development

3.1.2.1 System options identification

Screening of IGFC Preliminary Concept was conducted in prior analysis. Of the concepts identified, the following were selected as the baseline and alternative baseline:

- Baseline (BL): Radiant Syngas Cooler (RSC), CO_2 isolation after SOFC, once thru syngas
- Alternative Baseline: RSC, CO_2 removal before SOFC

Figure 3.2 shows the basic configurations and features of each. An un-pressurized SOFC will also be analyzed as part of a pressure sensitivity analysis for both the BL and ABL. In addition, a down-selection between the BL and ABL is given in this report.

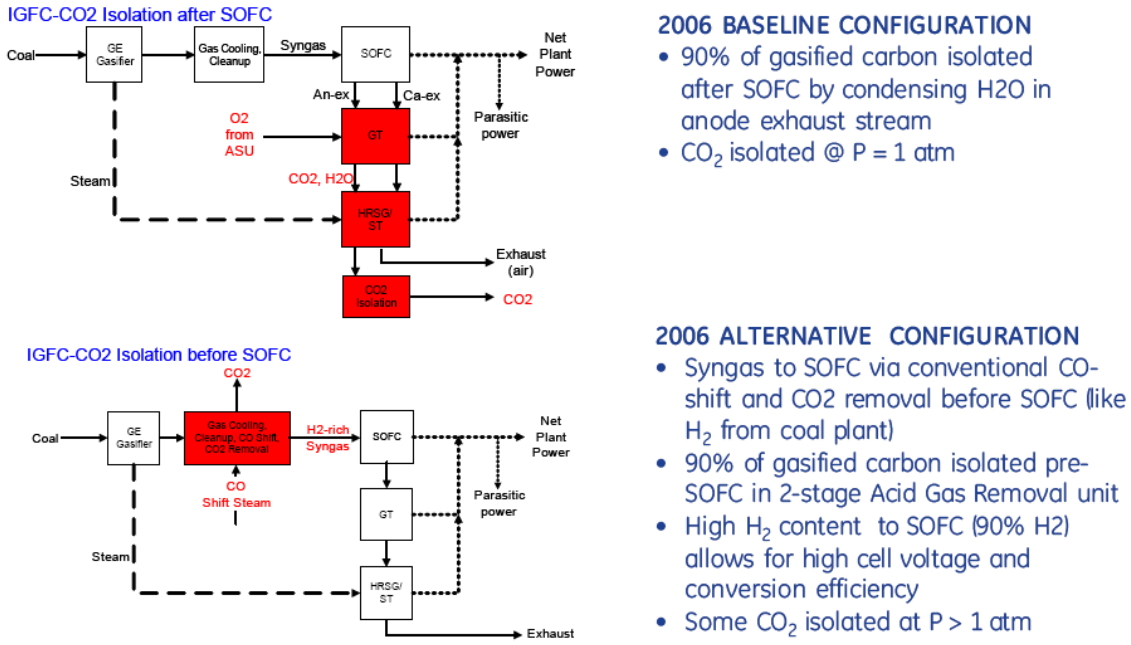

Figure 3.2 BL and ABL IGFC Concept Configurations

3.1.2.2 System requirements definition

The IGFC system requirements, as reported earlier, are as follows:

- 600 MW net power
  - Most common coal plant size (600-700 MW) proposed in US
  - Cost economies of scale
- 50% HHV efficiency
- 90% CO_2 isolation
- $400/kW for power producing blocks
- Bituminous coal, 10% moisture

The IGFC requirements were derived from the Phase III DOE Minimum requirements as shown in Table 3.2 except for the plant size; this size is similar to GE's Integrated Gasification Combined Cycle reference design power rating. The 600 MW size was selected for the IGCC reference design as it achieves economies of scale and is the most common coal plant size proposed for all power plants [1].

Table 3.2 DOE SECA Coal Program Technical Requirements

DOE MINIMUM REQUIREMENTS Fuel Cell Coal-Based Systems			
	PHASE I	PHASE II	PHASE III
COST	$600/kW	$400/kW	$400/kW
SYSTEM EFFICIENCY (HHV)	40%	45%	50%
STEADY STATE TEST @ NORMAL OPERATING CONDITIONS	1500 hours Δ Power# 4.0% degradation/ 1000 hours	3000 hours Δ Power# 2.0% degradation/ 1000 hours	>25,000 hours Δ Power# 0.2% degradation/ 1000 hours
TRANSIENT TEST	10 cycles Δ Power# 1.0% degradation after 10 cycles.	10 cycles Δ Power# 0.1% degradation after 10 cycles.	2 thermal cycles Δ Power# 0.1% degradation after 2 full thermal cycles.
TEST SEQUENCE	1) Steady State Test - 1000 hours 2) Transient Test 3) Steady State Test - 500 hours	1) Steady State Test - 2000 hours 2) Transient Test 3) Steady State Test - 1000 hours	1) Steady State Test - 25,000 hours 2) Transient Test TBD
FUEL TYPE	Gas composition identical to or simulating that proposed for the Phase III proof-of-concept system.		Coal-derived syngas
MAINTENANCE INTERVALS	Design aspects should not require maintenance at intervals more frequent than annually.		
DESIGN LIFETIME	> 40,000 operating hours.		

IGFC Plant Conceptual Design

POC System Demonstration

SOFC Stack Demonstration

Two bituminous coals have been identified as shown in Table 3.3.

Table 3.3 Coal compositions

Coal Properties	Units of Measure	Performance Coals	
		Illinois #6	Pittsburgh #8
Ultimate Analysis, dry basis			
Carbon	wt %	69.94	73.21
Hydrogen	wt %	5.00	4.94
Nitrogen	wt %	1.50	1.38
Sulfur	wt %	3.23	3.30
Oxygen	wt %	7.90	4.85
Ash	wt %	12.25	12.23
Chloride	ppmw	1,800	900
As Received Moisture	%	10.00	10.00
HHV Coal*	Btu/lb dry	12626	13236

* Calculated from Perry's 7th edition

Analysis of the two down-selected concepts, Baseline or BL (CO_2 removal after SOFC) and Alternative Baseline or ABL (CO_2 removal before SOFC) systems, was performed. Thermodynamic system models were created using ASPEN PLUS and GateCycle™ modeling platforms for the BL System without CO_2

isolation. System net power is 527 MW; when the final designs are defined, the system will be scaled to yield a net 600 MW.

The power summary results are plotted in Figure 3.3 to compare relative values of the different elements of power producers and consumers. As can be seen, the largest element is the SOFC producer at about 31% of the coal HHV; the gas turbine (GT) and steam turbine (ST) produce 14% and 11% of the coal HHV. The largest parasitic consumption is attributed to the oxygen generation and compression for a total of about 5% of the coal HHV.

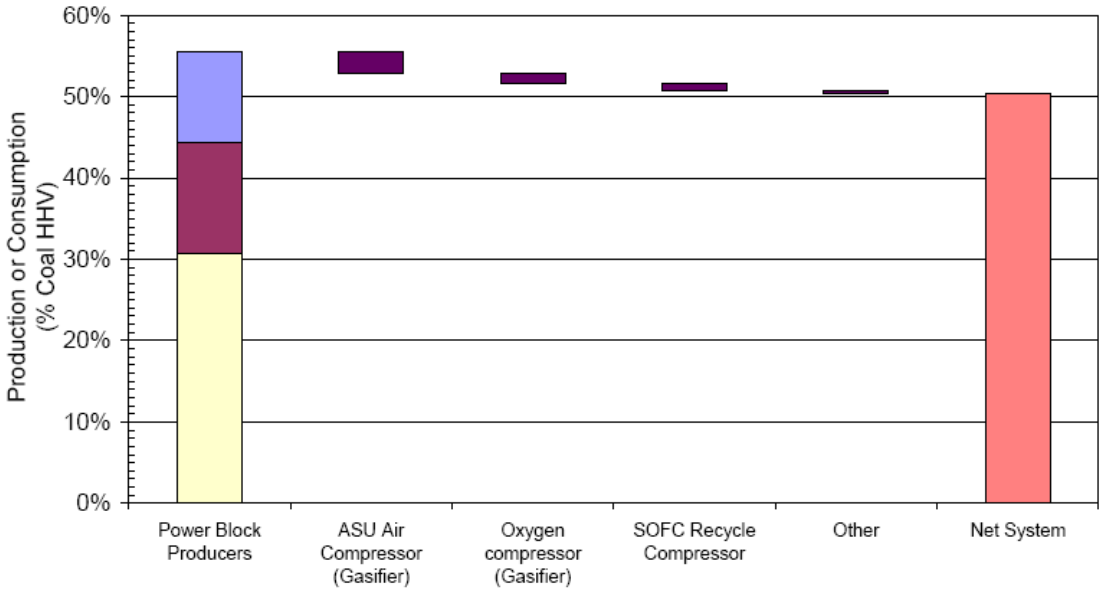

Figure 3.3 BL (without CO_2 Isolation): Comparison of Producers and Consumers

BL Concept
System performance models were created as follows:

• An ASPEN PLUS model to simulate gasification, air separation units, syngas cooling and cleanup, the SOFC and GT power blocks, and the CO_2 separation from the anode exhaust stream after it passes through the heat recovery steam generator (HRSG).

• A GateCycle™ model to simulate the Heat Recovery Steam Generator (HRSG) and Steam Turbine (ST) power block; in addition, steam and boiler feed water (BFW) interfaces from the gasification and syngas clean-up are simulated as sinks or sources. For the BL, there are 2 HRSG trains.

• Equivalent net parasitic requirements (steam and power) were estimated for a sulfur removal from the system; a conventional Selexol-type Acid Gas Removal (AGR) system is used to remove H_2S from the dirty syngas stream. The net

parasitic requirement includes the AGR, Sulfur Recovery Unit (SRU) and Tail Gas Cleanup Unit (TGCU) that converts the sulfur in the coal to elemental sulfur.

System efficiency sensitivity to the air temperature rise and the cell voltage are plotted in Figure 3.4.

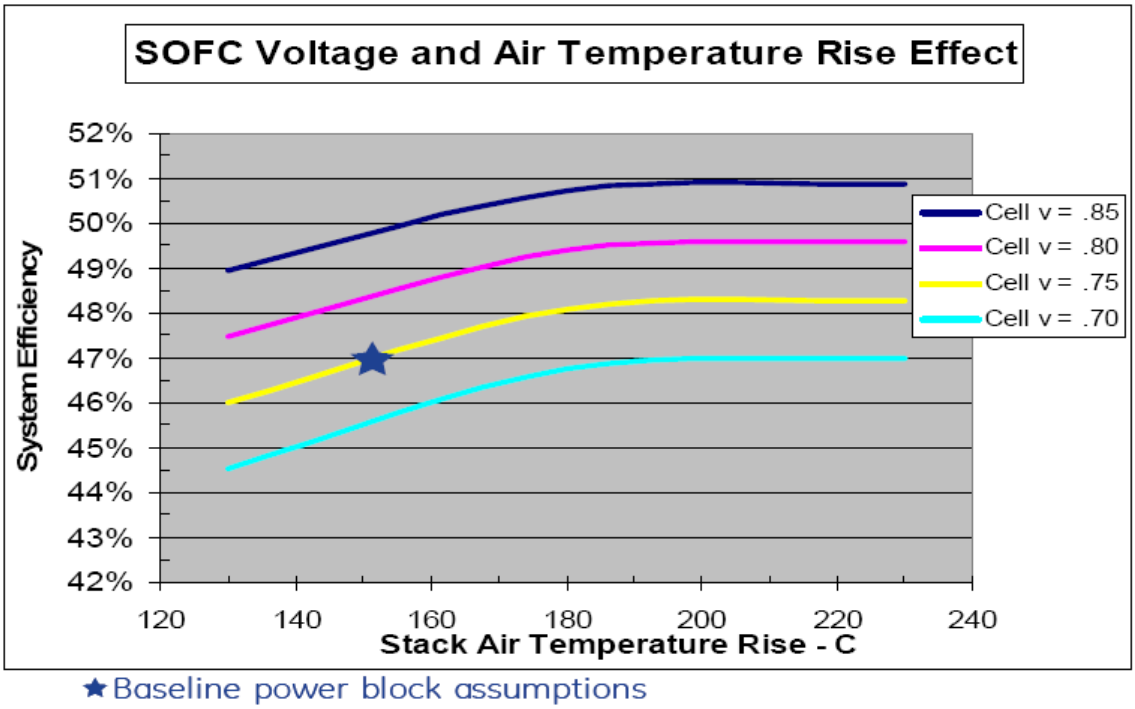

Figure 3.4 BL System Efficiency Sensitivity

ABL Concept
System performance models were created as follows:

• An ASPEN PLUS model to simulate gasification, air separation unit, CO-shift, syngas cooling and cleanup, and the SOFC and GT power blocks

• A GateCycle™ model to simulate the HRSG and ST power block; in addition, steam and BFW interfaces from the gasification and syngas clean-up are simulated as sinks or sources .

• Equivalent net parasitic requirements (steam and power) were estimated for sulfur removal and CO_2 isolation from the system; a conventional Selexol-type AGR system is used to remove H_2S and isolate CO_2 from the dirty, shifted syngas stream. The net parasitic requirement includes the AGR, Sulfur Recovery Unit (SRU) and Tail Gas Cleanup Unit (TGCU) that converts the sulfur in the coal to elemental sulfur.

System efficiency sensitivity to the air temperature rise and the cell voltage are plotted in Figure 3.5; for the baseline parameters of the fuel cell (150 C air

temperature rise, average cell = 0.75V, 80% fuel utilization), the system efficiency as modeled is near 46%.

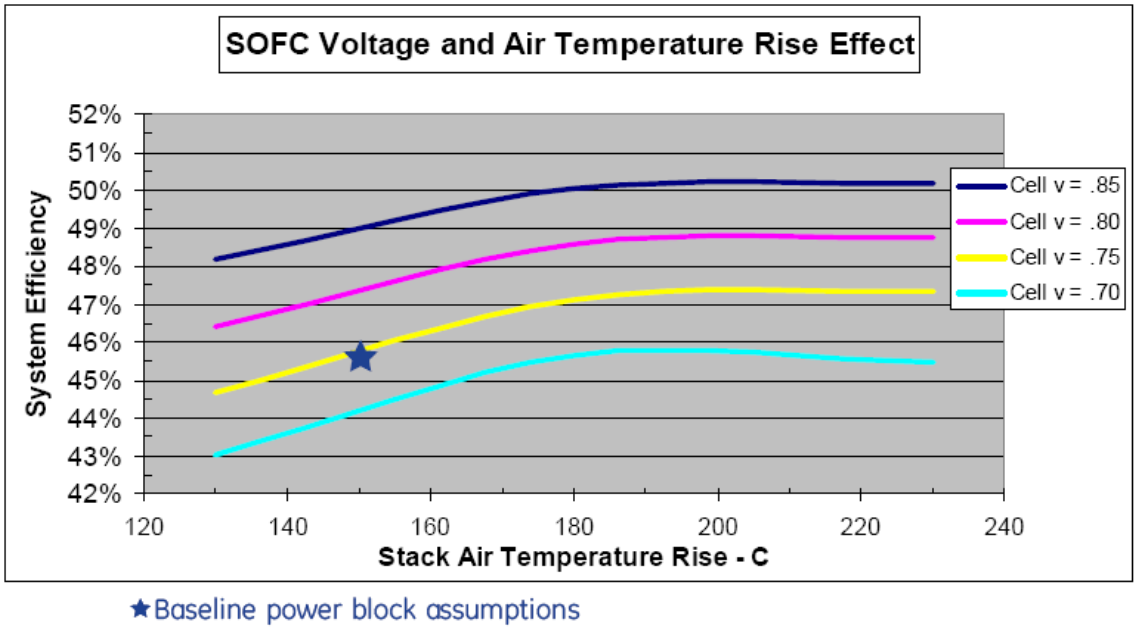

Figure 3.5 ABL System Efficiency Sensitivity

Down-Selection: BL vs. ABL

In order to down-select, a Pugh Matrix was utilized with the following criteria:
- System efficiency potential (>=50%)
- CO_2 Removal potential (>= 90%)
- Power blocks cost potential (< $400/kW)
- Technology feasibility risk
- Stack compatible with GE goals
- Power blocks availability
- Total IGFC cost
- Total IGFC availability
- Design compatible with IGCC development
- CO_2 Sequestration readiness (pressure)

System Efficiency potential (>=50%): A summary of the analysis presented above is as follows:
- At comparable stack performances (air temperature rise, cell voltage, fuel utilization), BL and ABL have similar efficiencies
- Improvements needed to reach 50% without stretching stack requirements beyond feasible limits: the approach will be to investigate improving other technology efficiencies such as coal gasification, gas processing, inverter, etc. moderately
- Improved stack performance can be expected with ABL fuel

As the H_2 mole-fraction for the ABL is near 0.9 compared to the BL cases, it should be possible to increase the assumed cell voltage while still maintaining a similar power density compared to the BL system. To support this assumption, analysis was done to determine a potential voltage advantage of the ABL vs. the BL case including the following assumptions:

- Area Specific Resistance (ASR)
  - o 0.19 ohm-cm^2 is a goal
  - o A H_2-rich stream can have an ASR advantage over a CO-rich +H_2-stream (similar to the BL gases) of 20% (ASR = 1.2 x 0.19 = 0.228 ohm-cm^2); in some tests, a higher advantage has been observed
- Effective Nernst
  - o Calculated as the average of inlet and outlet anode and cathode gases
  - o Calculated from the partial pressures of O_2, anode and cathode
- Steam to carbon (S/C) ratio
  - o As the BL has a high quantity of CO, carbon deposition is possible in spots where the gas must be heated to the SOFC temperature. The syngas from the Selexol system exits at about 38 C and must be heated to 650 C before entering the stack. A S/C of 1.0 is assumed here
- Power densities of greater than 0.5 W/cm^2 are required to meet cost goals.

.

Assuming the ABL can achieve an average of 0.8 V/cell at similar power densities for the BL case at 0.75 V/cell (or a 50-mV advantage), the system efficiency of the ABL is over 47%. Hence, given the cell voltage advantage of the ABL over the BL, the overall system efficiency of the ABL could be higher than the BL.

<u>CO_2 Removal potential (>= 90%)</u>: Both concepts are technically capable of isolating 90% or higher of the CO_2.

<u>Power blocks cost potential (< $400/kW)</u>: A count of the major units in both systems is shown in Table 3.4. As the BL has 2 turbines, including a high-temperature turbine for the anode gas combustor with pure oxygen, and 2 HRSG units, the ABL should have a cost advantage.

Table 3.4 Component comparisons

SUBSYSTEM		BL	ABL
GASIFICATION	Gasifier	x	x
	Radiant Syngas Cooler	x	x
	Convective Syngas Cooler	x	x
ASU	For gasifier	x	x
	For anode gas combustor	x	----
SHIFT REACTOR		----	x
GAS CLEANUP	COS Hydrolysis	x	x
	Acid Gas Removal		
	H2S	x	x
	CO2	----	x
	Sulfur Plant	x	x
	Tail Gas Cleanup	x	x
	H2S Polish	TBD	TBD
SOFC	Pressure SOFC modules	x	x
	Flow Control Devices	x	x
	Cathode Recycle Compressors	x	x
	Invererter	x	x
GT	Air Compressor	x	x
	Combustor	x (hi T)	x
	Combusted Gas Turbine	x (hi T)	x
	Vitiated Air Turbine	x	----
HRSG-ST	Combusted Gases	x	x
	Vitiated Air	x	----
EXHAUST CONDENSER		x	
# MAJOR SUBSYSTEMS/COMPONENTS		20	18

Conventional technology
Additional, conventional technology
Major technology development
Engineering technology develoment

Technology feasibility risk: Table 3.4 shows a qualitative description of the technology development required to realize the IGFC system goals. The highest risks are associated with the SOFC stacks and the flow control devices to those stacks. Both also have engineering technology developments required but at this time are not considered risks that could be judged an advantage of one concept over the other.

Stack compatible with GE goals: Both are similarly in line with GE goals. Compared to a natural gas fueled system, one major difference for both concepts is the lack of methane in the anode feed gas that represents potential for internal reforming.

Power blocks availability: While the BL has more power block components, which usually implies less availability, the components are in parallel. No clear advantage can be seen at this time.

Total IGFC cost: While there is an advantage of the power blocks cost for the ABL as noted above, further analysis would have to be done to ascertain any overall system cost advantage.

Total IGFC availability: Further analysis would have to be done to ascertain any overall concept advantage.

Design compatible with IGCC development: As GE's plan for an IGCC with CO_2 sequestration capability is very similar to ABL, ABL has an advantage over BL. CO_2 Sequestration readiness (pressure): As the ABL can flash some of the CO_2 off at pressures higher than atmospheric pressure, ABL has an advantage over BL.

The summary of the down-selection is presented in Table 3.5. As noted the ABL score is higher than the BL; for 2007, the ABL now is the baseline IGFC system concept.

Table 3.5 Down selection Pugh Matrix

Key Criteria	*Importance Rating*	BASELINE	ALTERNATIVE BASELINE
System efficiency potential (>=50%)	5		+
CO2 Removal potential (>= 90%)	5		S
Power blocks cost potential (< $400/kW)	4		+
Technology feasibility risk	5		S
Stack compatible with GE goals	5		S
Power blocks availability	2		S
Total IGFC cost	2		S
Total IGFC availability	2		S
Design compatible with IGCC development	2		+
CO2 Sequestration readiness (pressure)	1		+
Sum of Positives			4
Sum of Negatives			0
Sum of Sames			6
Weighted Sum of Positives			12
Weighted Sum of Negatives			0
TOTAL WEIGHTED SCORE			12

Concept Selection Legend	
Better	+
Same	S
Worse	-

3.1.3 Natural gas system development

3.1.3.1 System concept definition

The natural gas hybrid system concept includes multiple SOFC stacks with a steam reforming fuel processor, a GT, a cathode recycle compressor, an anode recycle ejector, a recuperator, an inverter and other components. Natural gas is usually provided pressurized and it is used to drive the anode recycle ejector. A

heat recovery steam generator (HRSG)/ST is added to produce power from the waste heat of the hybrid system exhaust (Figure 3.6).

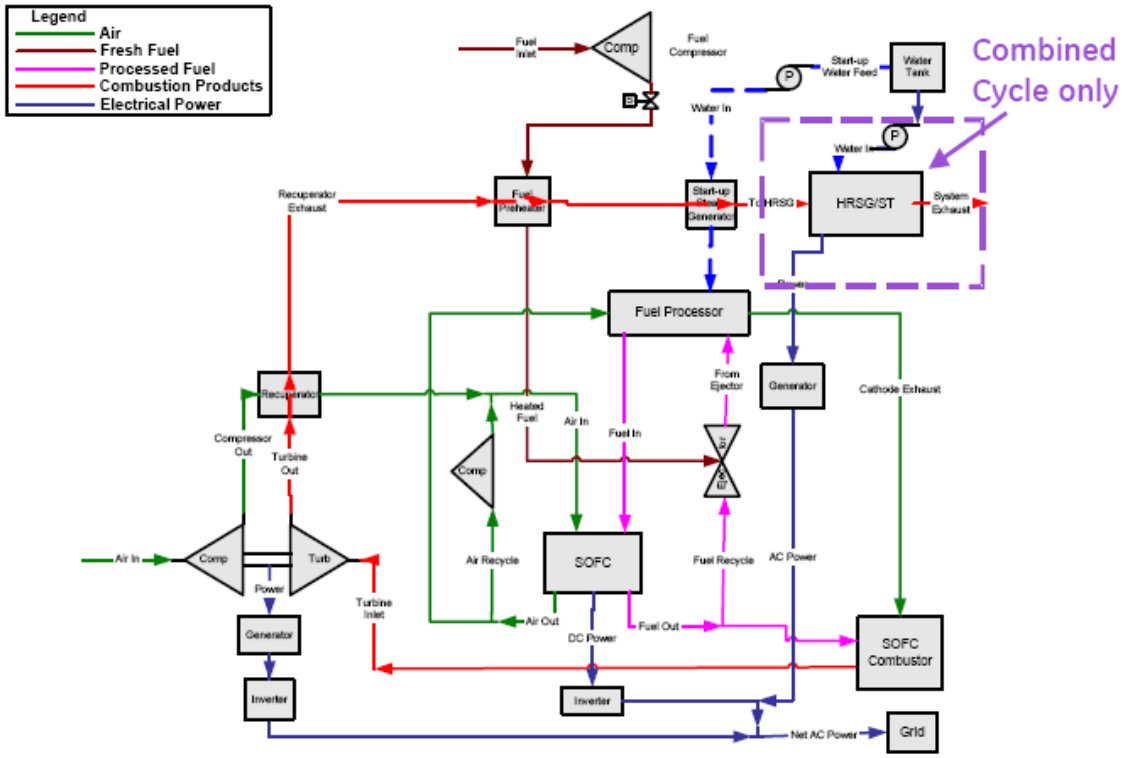

Figure 3.6 Baseline SOFC Hybrid System

The gas turbine compressor supplies pressurized air to the SOFC stacks. Air to the SOFC provides the reactant O_2 as well as controls the average SOFC temperature and temperature rise. The air is preheated to the SOFC operating temperature by heat exchange with the GT exhaust and by recycling part of the cathode exhaust stream. The natural gas fuel is compressed to the system pressure, preheated and mixed with an anode gas recycle stream before entering the steam reforming fuel processor (FP). The FP, partially converts the fuel to a hydrogen-rich gas (reformate) and supplies it to the SOFC stacks. Unconverted fuel from the FP is internally reformed within the stack (internal reforming). The preheated air and pre-reformed fuel streams electrochemically react in the SOFC to provide DC power and waste heat. Upon integration in a combined cycle configuration the exhaust heat is captured by a three-pressure Heat Recovery Steam Generator (HRSG) to produce superheated steam and run a condensing steam turbine. The system performance simulation has been developed using Aspen Plus™, and GateCycle™ heat and mass balance analysis tool. The system model calculates the heat and material balances around the system components with appropriate component performance parameter assumptions. Using these assumptions, the SOFC hybrid and SOFC combined cycle (SOFC CC) system efficiencies are 65.8% and 69.8% respectively.

3.1.3.2 Analysis results and discussion

The principal planar SOFC operating parameters are pressure, temperature and stack temperature gradient, cell voltage, fuel utilization, leakage rate and percentage of internal reforming. The effect of these parameters on hybrid system performance is analyzed as follows:

Effect of SOFC average temperature and temperature rise: The maximum air temperature rise through the stack is fixed. This assumption drives the airflow requirement through the stack. The air temperature rise is considered from the stack inlet air manifold to the stack outlet air manifold. The air temperature rise is usually limited by the cell temperature gradients. The relationship between the air temperature rise (or the airflow) and the maximum allowable cell temperature gradient is highly dependent on the stack and cell design. All of the parameters trade-offs discussed in this paper were carried out for a stack exit temperature of 800°C. The absolute level of stack exit temperature has some effect on the system efficiency as it affects the turbine inlet temperature and thus gas turbine performance. High temperature gradients lead to higher SOFC average temperature and higher turbine inlet temperature resulting to an increase on efficiency as shown in Figure 3.7.

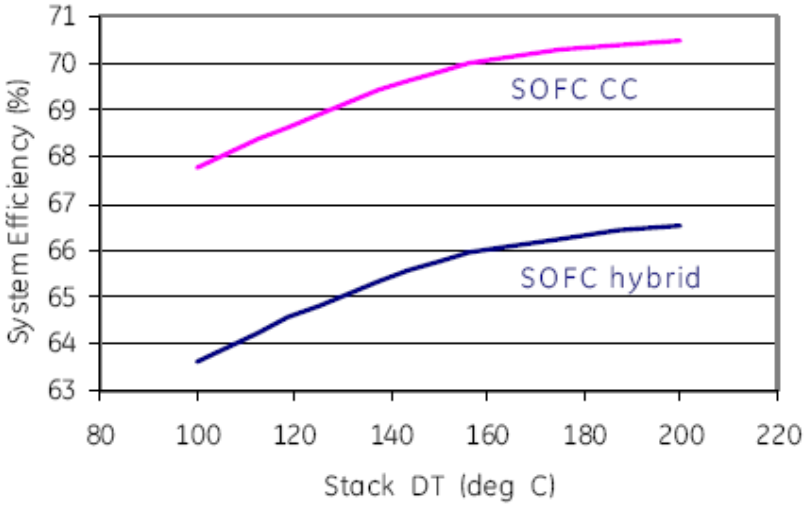

(a)

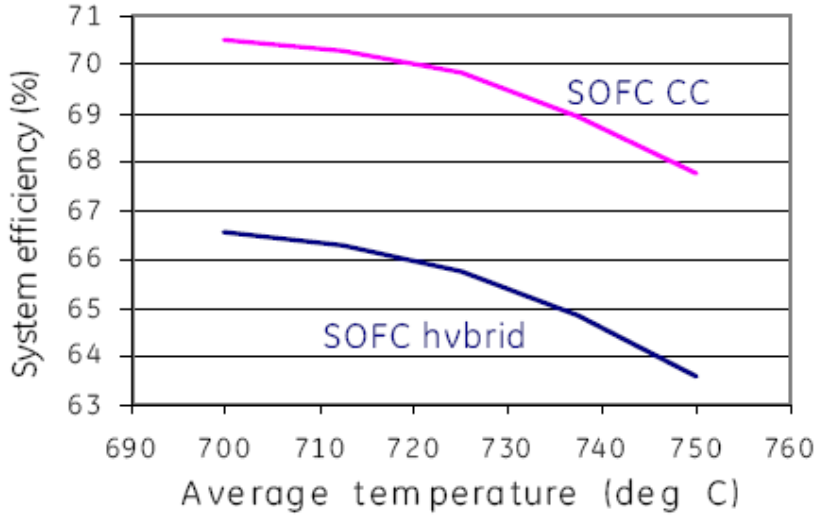

(b)

Figure 3.7 (a) Effect of temperature gradient at 0.75V, 80% fuel utilization and PR 15. (b) Effect of average fuel cell temperature at 0.75V, 80% fuel utilization and PR 15.

Effect of operating voltage: The baseline average single-cell voltage at full load is 0.75 V. The single-cell voltage drives the SOFC stack and the overall system efficiency. Higher voltage leads to higher fuel cell power output (at a fixed fuel utilization) and as a result higher system efficiency as shown in Figure 3.8.

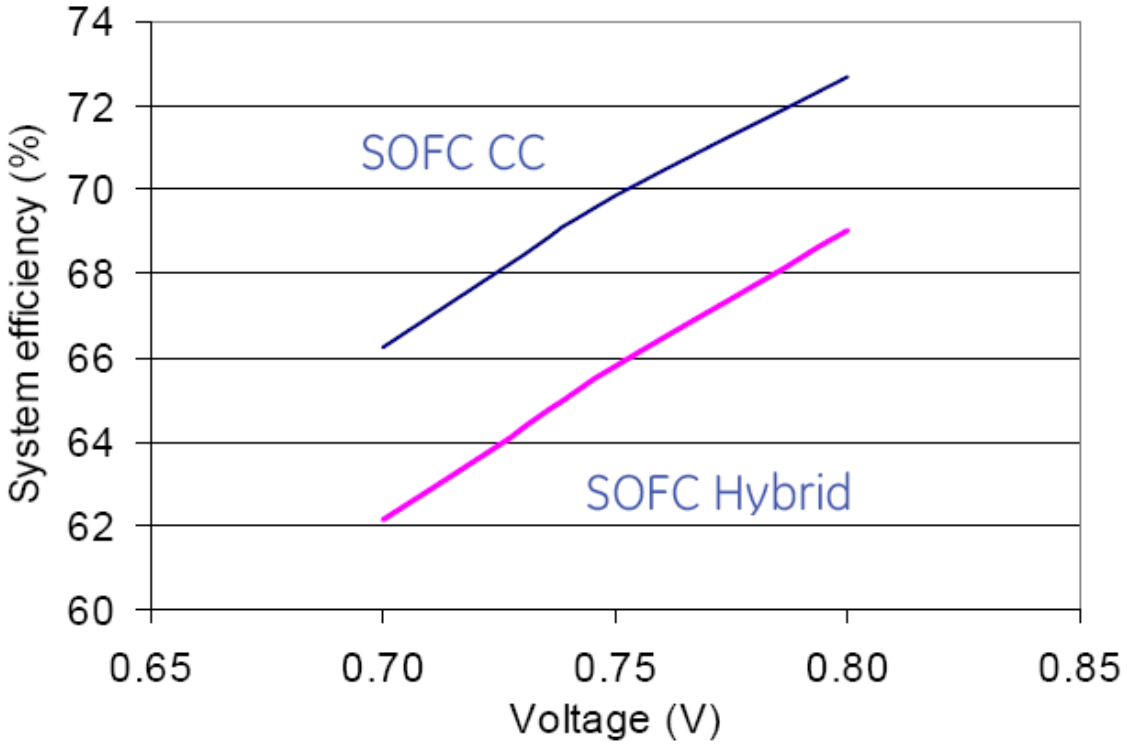

Figure 3.8 Effect of cell voltage on system efficiency at 150 degrees stack DT , 80% fuel utilization and pressure ratio PR 15.

However, higher voltage operation requires a larger overall SOFC active area, as power density is reduced. The single cell voltage must be traded with the SOFC power density to achieve the most favorable system efficiency – cost balance.

Effect of Internal reforming: A percentage of pre-reforming occurs prior to the fuel cell. Pre-reformers require a minimum amount of steam in the feed that corresponds to a steam-to-carbon (S/C) ratio of 1.5 ensuring that carbon deposition reactions are avoided. The fuel processor is assumed to be in chemical equilibrium. A high percentage of internal reforming has a positive impact on the overall system efficiency by providing a cooling effect to the SOFC, thereby allowing a reduction of the SOFC air feed rate; the impact is significant as shown in Figure 3.9.

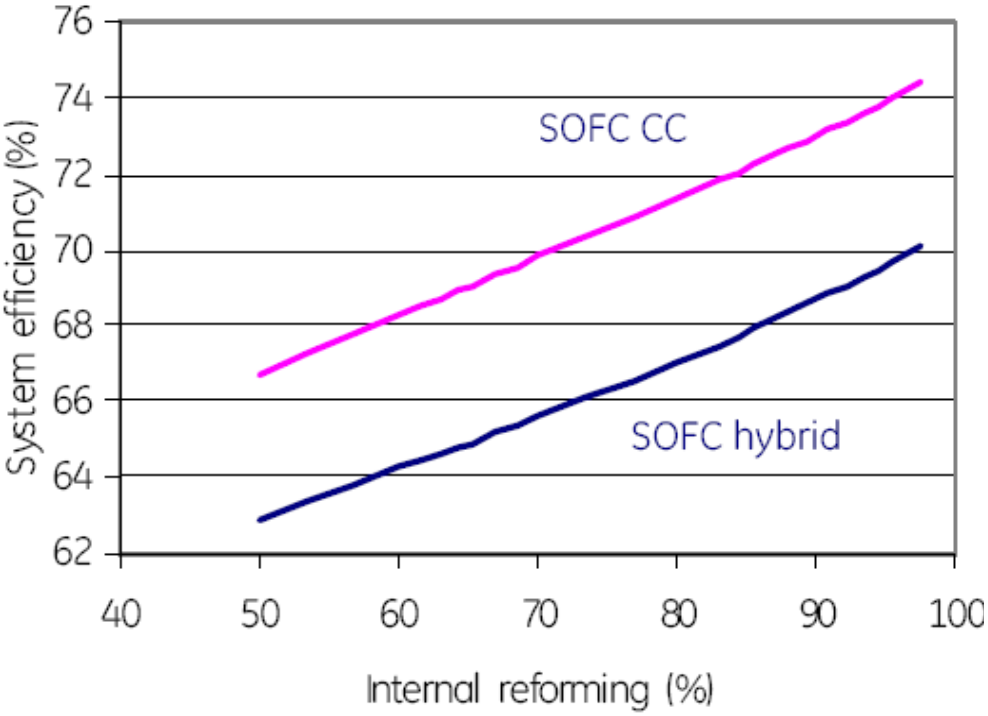

Figure 3.9 Effect of internal reforming at 0.75V, 80% fuel utilization and PR 15

Effect of fuel utilization: The effect of fuel utilization in the overall system performance is shown in Figure 3.8. While higher fuel utilizations lead to better system performance, this parameter must be traded against the power density and resulting stack cost (similar to the voltage case). As fuel utilization increases, the general effect is to lower the cell voltage due to polarization and Nernst voltage losses. In the present analysis, these effects are not accounted thus the increase in utilization is monotonic.

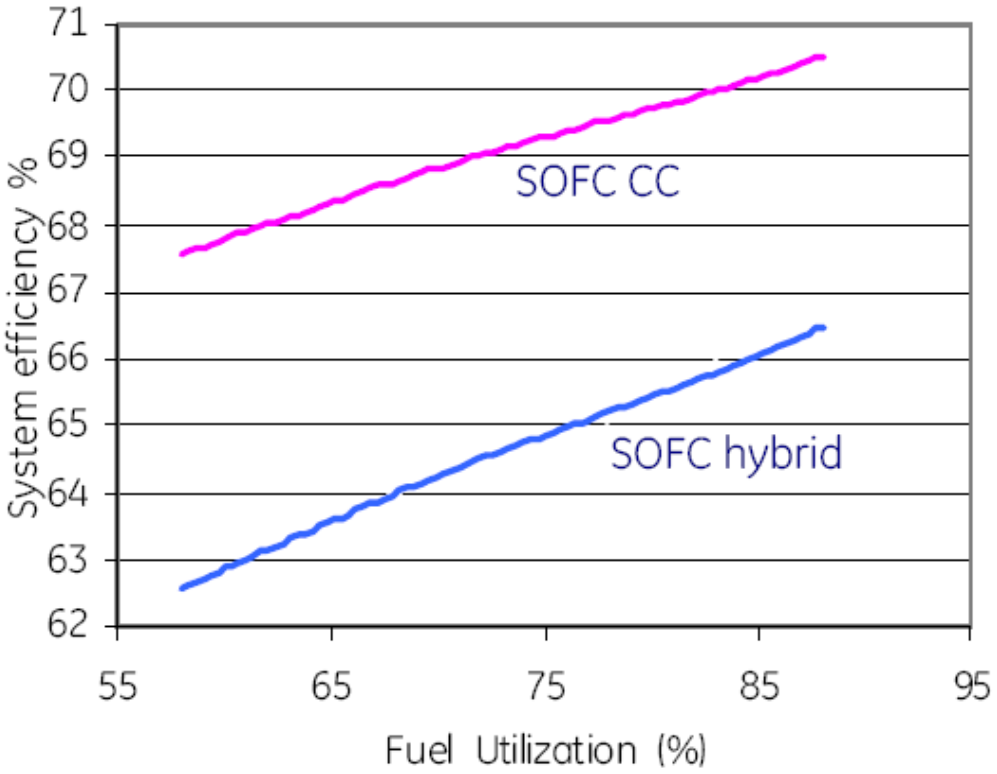

Figure 3.10 Effect of fuel utilization at 0.75V, 150 degrees stack DT and PR 15

Effect of fuel leakage: Depending on the fuel cell stack design fuel leakage is possible from the fuel cell anode. The leaked fuel can react with the hot cathode exhaust and burn with several detrimental effects. Localized leakage tends to increase degradation and damage fuel cell materials. The chemical heating of the leaked fuel increases stack temperature gradients and requires increased cooling airflow, lowering overall system efficiency. The effect of fuel leakage on the overall system performance is shown in Figure 3.11. The current analysis shown that 1% of fuel leakage reduces approximately 1% the system efficiency.

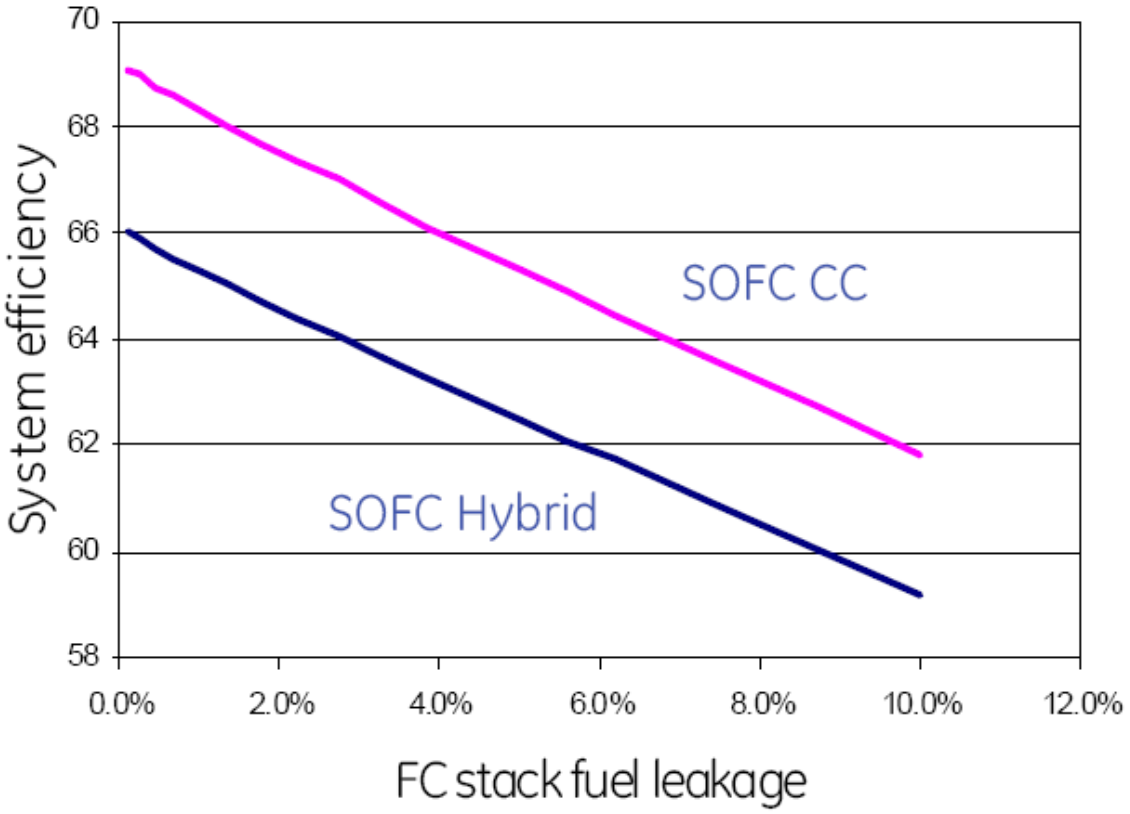

Figure 3.11 Effect of fuel cell fuel leakage at 0.75V, 80% fuel utilization and PR 15

Effect of pressure: The optimum GT and SOFC operating pressures are not necessarily the same. Thus pressure optimization of the overall hybrid system fuel cell gas turbine is important. The results of the pressure optimization study are shown in Figure 3.12. Based on the assumptions, the maximum efficiency for the hybrid system occurs at pressure ratio 8. When the system is integrated in a combined cycle configuration then the optimum pressure ratio is 9. The estimated maximum system efficiency is about 70%. The pressure drop assumed for the SOFC stack is 2% of the overall system pressure.

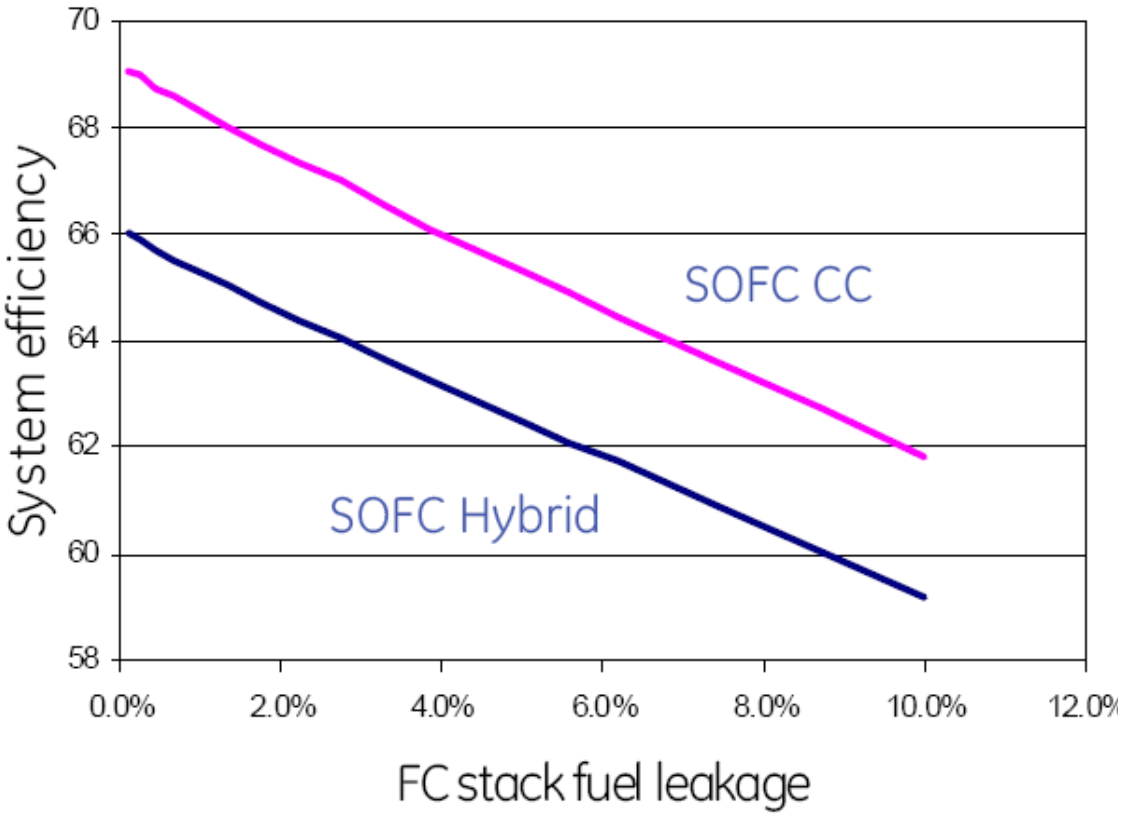

Figure 3.12 Effect of pressure at 0.75V, 150 degrees stack DT and 80% fuel utilization

The above analysis was carried out to determine system performance under various fuel cell stack operating conditions. The natural gas hybrid plant performance depends on component efficiencies, pressure drops, and heat losses. Using projected component efficiencies, the hybrid system efficiency derived was approximately 66.5 percent. Upon integration in a HRSG/ST bottoming cycle, the hybrid system efficiency increases by 4% to approximately 70%. The most important parameters impacting the system efficiency are the fuel cell voltage, the percentage of internal reforming and the percentage of fuel leakage from the fuel cell.

3.1.4 System and stack demonstration – NETL prototype

3.1.4.1 System assembly

The switch to a single 40-cell stack composed of 12” cells required the design of a new stack enclosure and stack interface. To take advantage of the new stack enclosure design, the balance of plant components were also repackaged.

Significant effort went into redesigning the new stack enclosure and the new balance-of-plant configuration to meet the system volume reduction and provide

a product like appearance. Ultimately the balance-of-plant was housed in the bottom half of the stack enclosure below the stack.

Efforts during this reporting period focused on assembling the new stack enclosure and supporting balance-of-plant components. Construction of the stack enclosure and thermal management system was completed.

The size of the stack enclosure was determined by using a heat transfer model developed to determine insulation thickness and the affects of various insulation arrangements. The insulation down-selection process evaluated materials on price, performance, manufacturability and impacts to other system components. For example, a lower performing material may have been cheaper, but when weighed against the increased size of the stack enclosure shell, increased heat loss and other factors, the micro-porous insulation proved the best choice. The insulation thickness and stack girth thus determined the stack enclosure shell inside diameter.

The need to redesign for the single stack presented an opportunity to utilize the same basic thermal management components repositioned inside the stack enclosure. This reduced thermal loses, allowed the gas connections to be reconfigured to design around hot gas interfaces. The new design has all gasses entering the stack enclosure cold. As a result, all the interfaces are maintained at relatively low temperatures improving seal reliability. For control as well as data collection a significant number of temperature and pressure sensors are imbedded in the balance-of-plant, leading to a number of passes through in the vessel.

The original prototype was designed with flexibility and accessibility in mind, which lead to a package that did not necessarily make the most efficient use of the footprint of the unit. With a smaller stack enclosure and internalized hot gas components, it was possible to significantly reduce the overall volume of the prototype. Specifically, the original unit had a volume of 10 m^3 whereas the new power plant is expected to fit within about 2.6 m^3. The prototype system that was tested can be seen in Figure 3.13.

Figure 3.13 SECA NETL Prototype System

3.1.4.2 Test results

The results of the 120-hour commissioning test will be discussed in the following sections. The peak efficiency and peak power performance of the NETL prototype system exceeded the SECA Gen 2 system, and were well above the SECA minimum requirements. The performance demonstration portion of the test is presented in Figure 3.14.

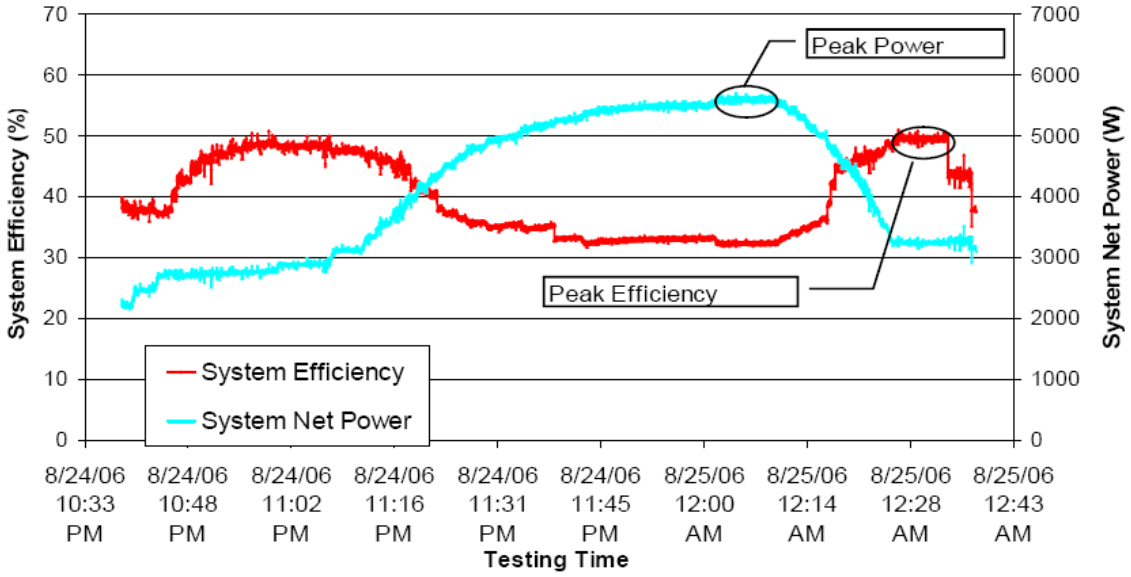

Figure 3.14 NETL Prototype Test Data

Peak efficiency

The peak efficiency was measured over a steady state period on August 25, 2006. After some exploration in changing various set points, especially oxygen-to-carbon ratio in the system, the peak efficiency settings were determined. Since this is a commissioning test, some system operating parameters were not fully explored in order to protect the stack and the system. The system achieved a DC efficiency of 49.6% under the following conditions:

- Fuel utilization of 79.5%
- Current of 112.6 A (184 mA/cm2)
- Average cell voltage of 0.783 V
- Gross DC power of 3.52 kW (144 mW/cm2)
- Net DC power of 3.27 kW

The overall system was stable for the peak efficiency period with no abnormalities with the system or the test facility. The individual cell voltages were stable with no sign of fuel distribution issues or cell starvation. The cell voltages for the SOFC stack can be seen in Figure 3.15. The cell voltage distribution is smooth across the stack. A histogram of all of the cell voltages can be seen in Figure 3.16. The mean voltage is 0.783 V with a standard deviation of 0.0194 V. All of the cells remained above 0.7 V at this test condition.

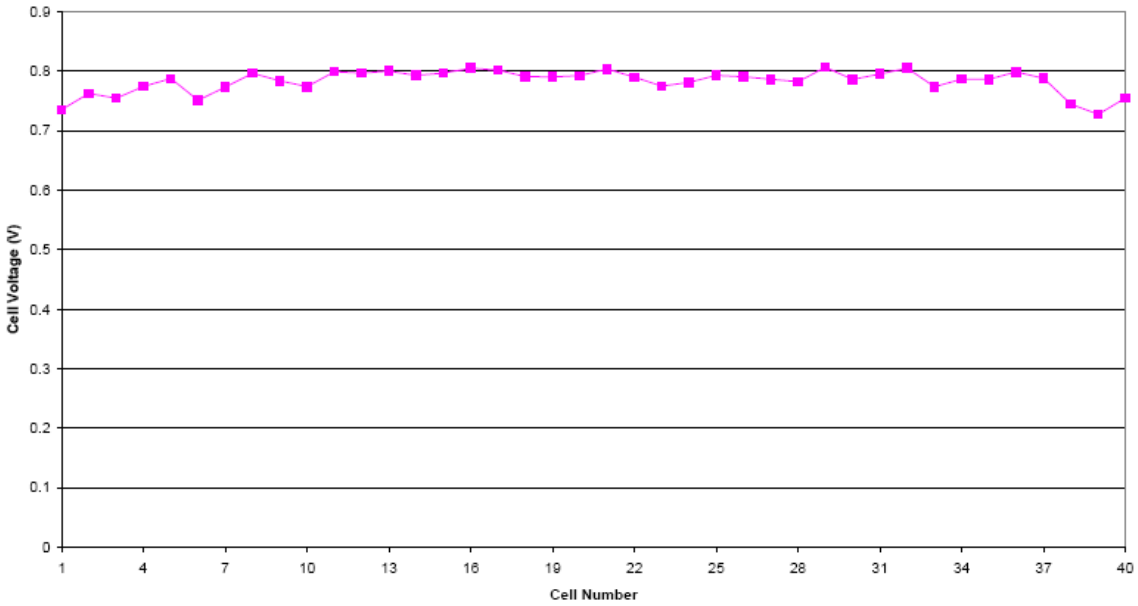

Figure 3.15 Cell Voltages at Peak Efficiency Point.

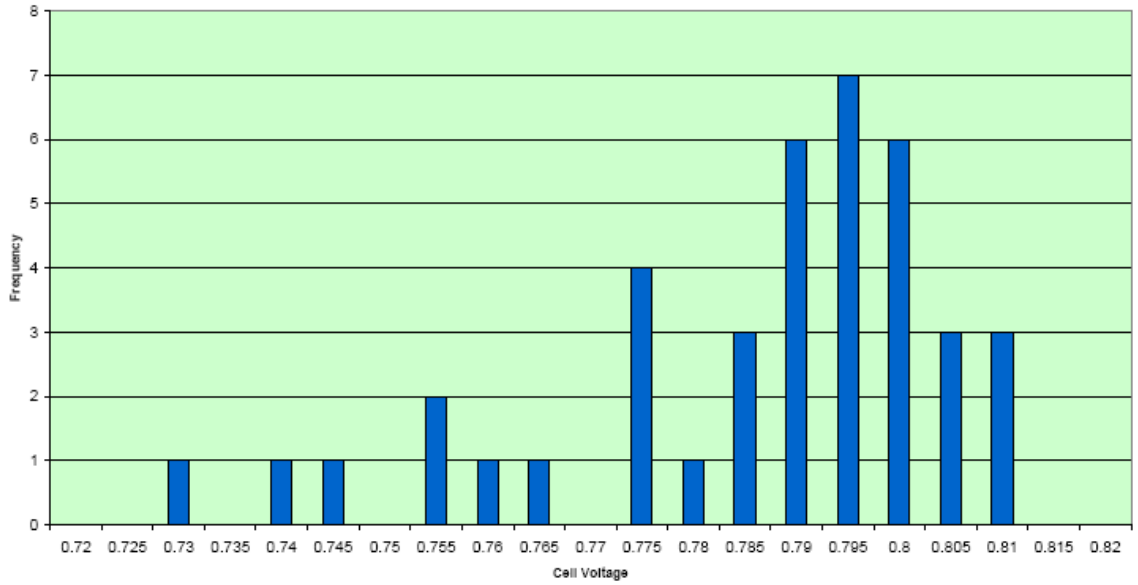

Figure 3.16 Histogram of all Cell Voltages at Peak Efficiency Point.

The temperature distribution within each of the four stacks can be seen in Figure 3.17. The thermocouple for cell 4 was not functional during the test. The trends show higher temperatures in the center cells of the stack and that the top of the stacks are at a higher temperature than the bottom of the stacks. The stack assembly was at an average temperature of 808°C.

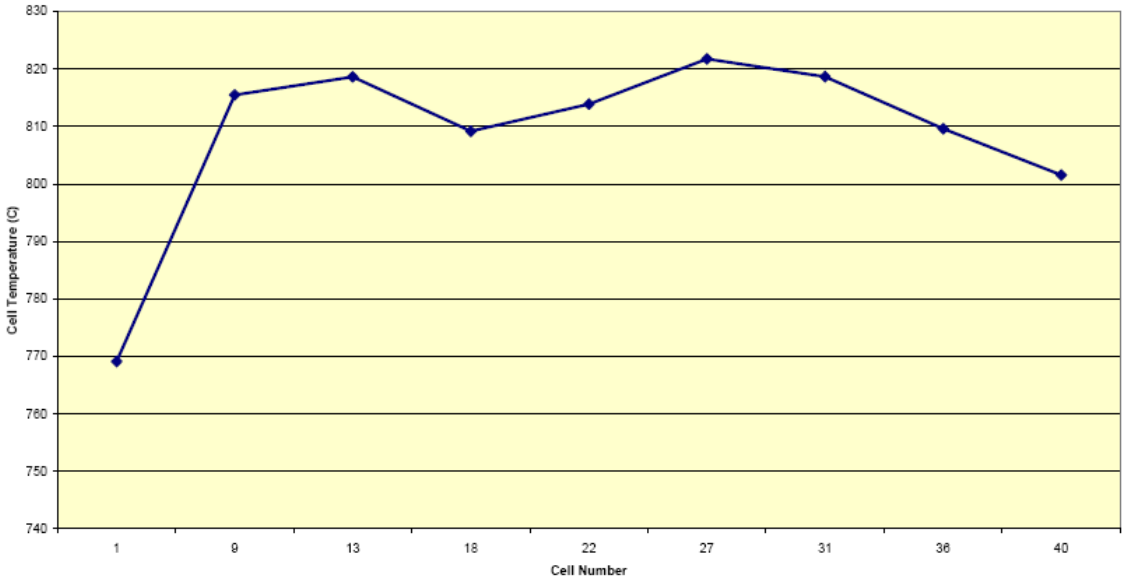

Figure 3.17 Stack Temperature Distributions at Peak Efficiency Point.

Peak Power

The peak power was measured over a steady state period on August 25, 2006. After some exploration in changing various setpoints in the system, the peak power settings were determined. Since this is a commissioning test, some system operating parameters were not fully explored in order to protect the stack and the system. The system achieved a net DC power of 5.62 kW under the following conditions:

- Fuel utilization of 63.7%
- Current of 242.2 A (395 mA/cm2)
- Average cell voltage of 0.639 V
- Gross DC power of 6.11 kW (249 mW/cm2)
- DC efficiency of 32.4%

The overall system was stable for the peak power period with no abnormalities with the test facility. The individual cell voltages were stable with no sign of fuel distribution issues or cell starvation. The cell voltages for the SOFC stacks can be seen in Figure 3.18. The typical end effects can be seen on the stack due to temperature distributions within the stack. A histogram of all of the cell voltages can be seen in Figure 3.19. The mean voltage is 0.639 V with a standard deviation of 0.0446 V. The majority of the cells remained above 0.6 V, and only a small percentage of cells were between 0.5 V and 0.6 V.

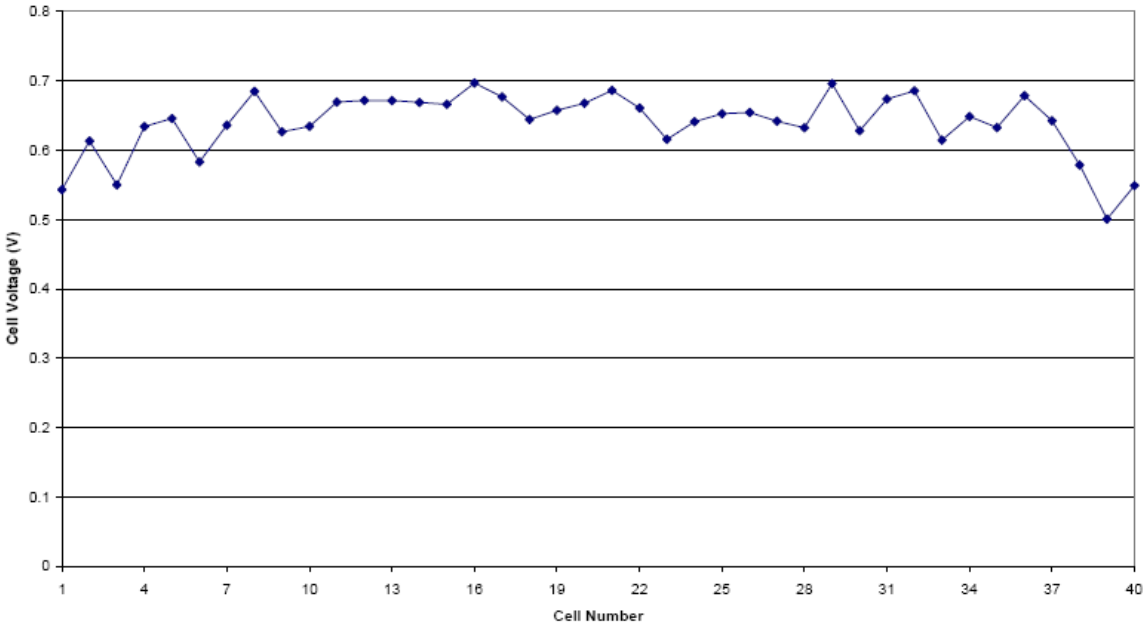

Figure 3.18 Cell Voltages at Peak Power Point.

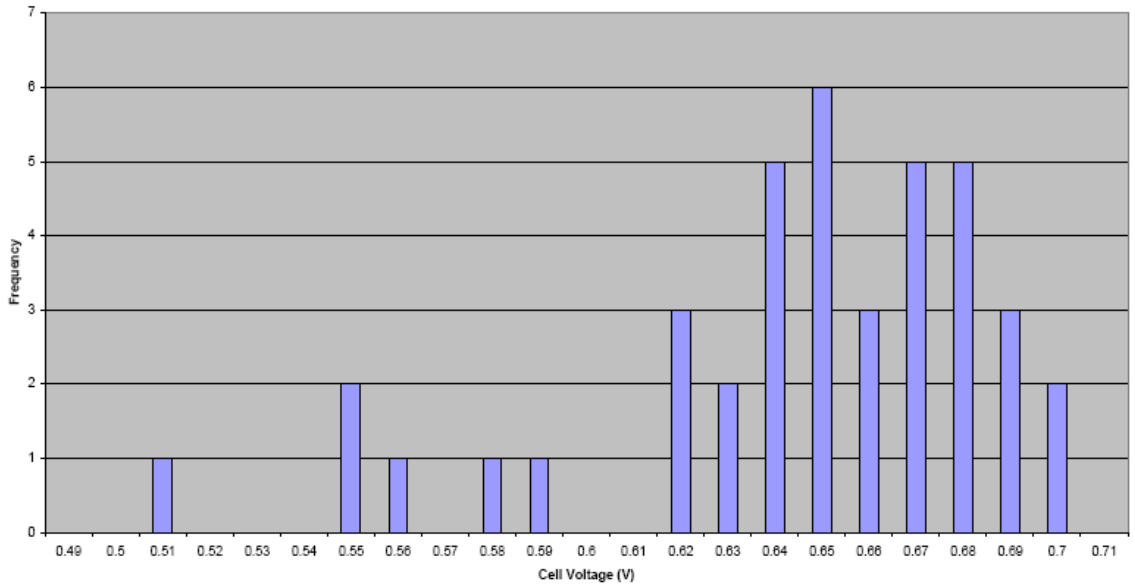

Figure 3.19 Histogram of all Cell Voltages at Peak Power Point.

The temperature distribution within each of the four stacks can be seen in Figure 3.20. The stack assembly was at an average temperature of 815°C.

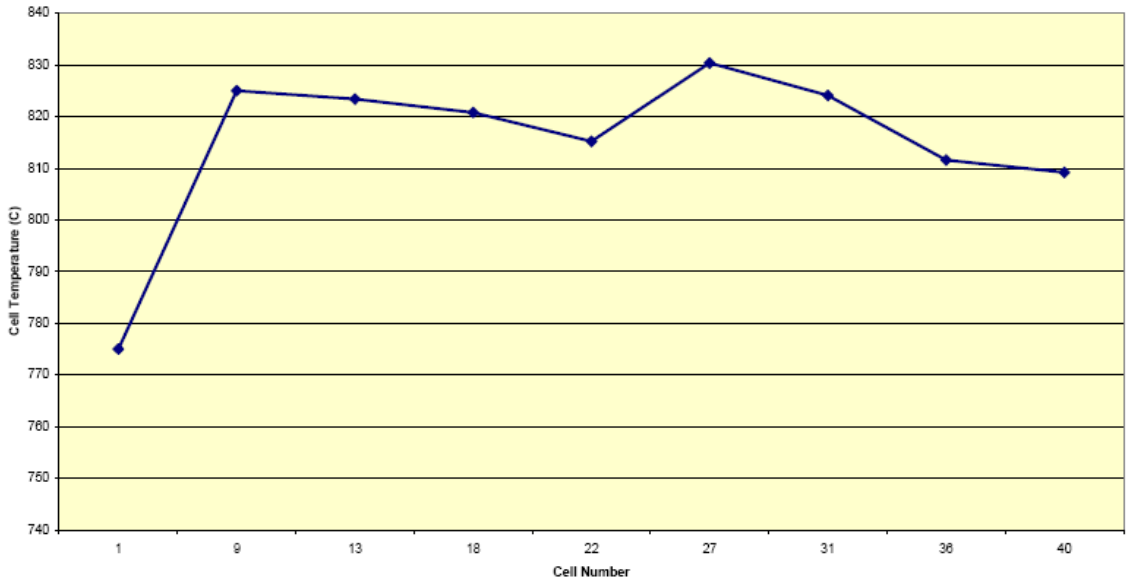

Figure 3.20 Stack Temperature Distributions at Peak Power Point.

3.2 SOFC Stack design

3.2.1 Flow field configuration

One of the key design features of a fuel cell stack is the flow field configuration. A summary of the attributes of cross, counter and co-flow configurations is presented in Table 3.6 for externals and internally manifolds.

Table 3.6 Trade-off for flow and manifold configurations

	Advantages	Disadvantages
External manifold	• Manifold can be integrated with enclosure • Decouple manifold from IC • Easy to scale up for stack footprints or heights • Low risk of crossover manifold leakage • Easy integration of features for internal reforming/cooling Cross flow • Simple manifold design • Simpler low cost IC design Co-flow • Low ΔT, good for performance and stack long term stability • Possible low cost IC design	• Challenge for sealing manifold onto the stack ▪ Dielectric seal ▪ Caulking ▪ CTE mismatch (sliding) ▪ Stack alignment ▪ Uniform compression Cross flow • High ΔT may impact performance and stack long term stability Co-flow • Challenge for flowfield design • Challenge for arrangement of external manifold
Internal manifold –Co-flow	• Easy preseal process • FlexArm manifold can take compliance • Low ΔT, good for performance and stack long term stability	• Critical cell alignment • Thermal mismatch between stack core & manifold • High risk of crossover manifold leakage • Additional metal content ~$30-40/kW • High metal scrap ratio for ICs • Challenge for the integration of features for internal reforming/cooling

All the three flow fields were considered for large SOFC stacks. Cross-flow has the lowest pressure drop but the temperature field associated with that configuration leads to large temperature gradients and stresses in the cell. Co-flow was predicted to have the smallest temperature gradients.

3.2.2 Manifold consideration

One of the key design characteristics of SOFC stacks is the type of manifold used and the method of sealing the manifold to the stack. Two common approaches used in small SOFC stacks and large MCFC stacks are internal and external manifolds. Internal manifolds are constructed by aligning gas ports that pass through each cell interconnect. In a stack in which cells are oriented horizontally, the aligned gas ports create a manifold that passes vertically through the stack connecting all the cells. The gas ports are sealed with a glass or compression gaskets between adjacent interconnects. These seals must prevent gas leakage and electrical shorting between cells.

External manifolds are plenums that connect the gas inlets and outlets for the stack of cells. In externally manifolded stacks the flow field inlets and outlets extend to the edge of the cell interconnects. These manifolds cover the respective inlets and outlets for fuel and air. The seals for external manifolds are critical. They must accommodate for the unevenness of the stack sealing surfaces, which are comprised of the edges of individual cells. The seals must also be good electrical insulators, because the manifold can form a conduction path from the top to the bottom of the stack with a potential difference of several hundred volts.

The key advantages of internal manifolds are that the seals are between smooth metal surfaces, the cell-to-cell alignment tolerance is less critical than for external manifolds and the potential across each seal is only the cell voltage (<1V). The disadvantages of internal manifolds are the greater amount of metal required, and the much greater seal length compared to external manifolds. GE cost models estimate additional cost for internally manifolded stacks.

In addition to lower cost and minimum seal length, external manifolds have the advantage that the manifold compression is decoupled from the active area compression in the stack. This avoids the major challenge of internally manifolded stack of independently loading the manifold seal and the active area. The key disadvantages to external manifolds are the uneven sealing surfaces and difficulty in assembly if ceramic caulks are used to fill the uneven surfaces.

3.2.2.1 External manifold testing stack

<u>Objectives</u>

The objectives of designing and manufacturing a testing stack were to 1) validate the concept of external manifold, and 2) develop a process for sealing external manifold (caulking, seal tape thickness, compression pressure, etc.).

Stack sizing

The size of the stack assembly including manifolds, compression systems, piping, electrical connections, etc. is constrained by the furnace in which it will be tested. In order to leave minimum 0.5" clearance inside the furnace of 18" ID (red circle), all the stack components were so designed to fit in a virtual cylinder of 17" OD (green circle) as shown in Figure 3.21.

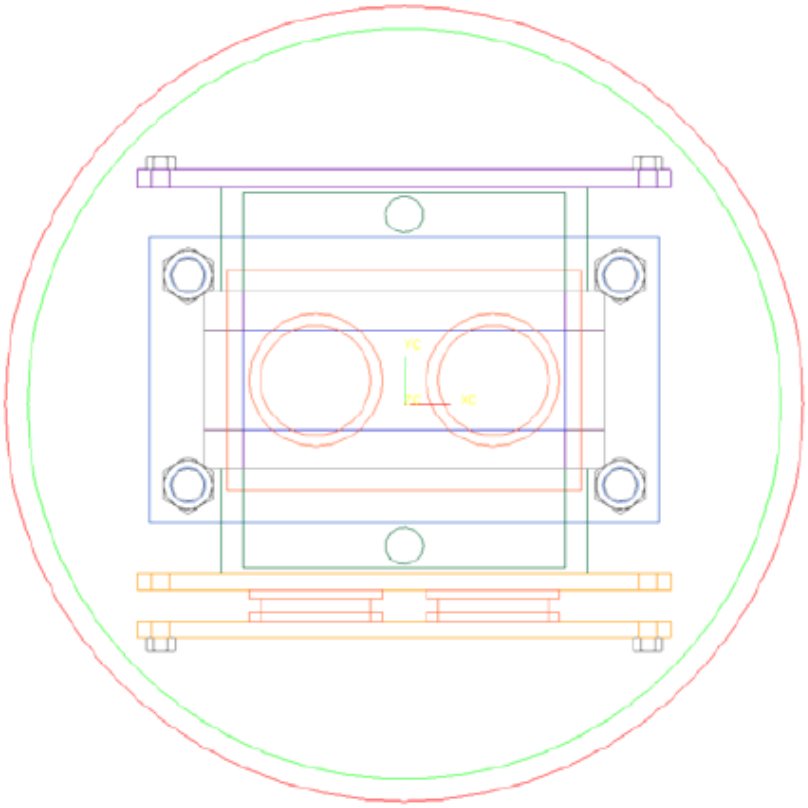

Figure 3.21 Furnace for manifold test stack and top view layout.

External Manifold

A simple 5-sided box was designed for the external manifold. In addition to its depth that distributes adequate flow, the width of its footprint on the stack is important for sealing the manifold. The wider the manifold landing zone, the longer the leakage path and thus the better the seal would be.

Manifold seal materials

The main functions of the seal are to limit the loss of fuel and air supplied to the stack and to prevent combustion that could degrade the stack. The seal for an external manifold of solid oxide fuel cell is required to provide both low leakage and long term stability over extended operation time up to 40,000 hrs and at high

temperature up to 900 C, yet the seal should be sustainable through multiple thermal cycles from high operation temperature to room temperature.

For a tall, full-size stack, the manifold seal has to isolate the high voltage as well as the high current between the manifold and the stack. A most important character of the seal is the CTE match to the materials with which it is in contact. If the seal has a significantly different CTE than the stack, the thermal expansion at the operating temperature (~ 800^{o}C) will cause the seal to crack and produce large leaks.

Compression Systems

Compression is required in a stack for adequate cell contact in the active area and seal in the cell perimeter to prevent gas leakage. When using external manifolds, the stack assembly is complicated by the second compression system required to seal manifold against the stack. Common choices for cell and manifold compression systems are mechanical bolting, cabling and pneumatics. Tie rod systems have been proven in the past experiences. However, to be able to vary the pressure on cell and on manifold seal during the test, stack was designed to have pneumatic systems (bellows) in both the vertical (stack compression) and horizontal (manifold) directions.

Flow field and interconnect (IC)

For the purpose of testing external manifold design, stack performance is not one of the requirements or CTQ's (Critical-to-Quality). Cross flow was the obvious choice. To further increase active area, this stack incorporated only two manifolds respectively for fuel in and out. Metallic interconnects were designed to have at least 3 components, bipolar plate, and anode and cathode flow fields and manufactured by a metal process such as cutting and brazing in this case. One of the objectives for this stack design is the minimum amount of metal for IC.

Stack assembly

The final stack designed for validating external manifold concept included a set of external manifolds for fuel and two sets of bellow systems respectively for cell and manifold compression.

3.3 Modeling

The SOFC-2D model was developed and a benchmarked with existing codes. Further validation was explored on the following cases:
Case1: Validation: SOFC-2D vs. Companari et al. [2]
Case 2: Effect of Inlet Temperature
Case 3: Effect of Internal Reforming

3.3.1 Validation: SOFC-2D vs. Companari et al. Results

The cell geometry is a 100 mm x100 mm cell. Simulations were carried-out for co-flow configuration under atmospheric pressure and 30 Amps (0.3 Amp/cm^2) and inlet temperature of 900 C. The fuel composition (mole fraction) H_2=26.26%, H_2O=49.34%, CH_4=17.1%, CO=2.94% and CO_2=4.36%.

Figure 3.22 shows cell temperature maps for co-flow configuration from SOFC-2D code (top) and Campanari et al (bottom). The max cell temperature predictions for both codes were very comparable (1020 C) leading to a cell deltaT of 120 C.

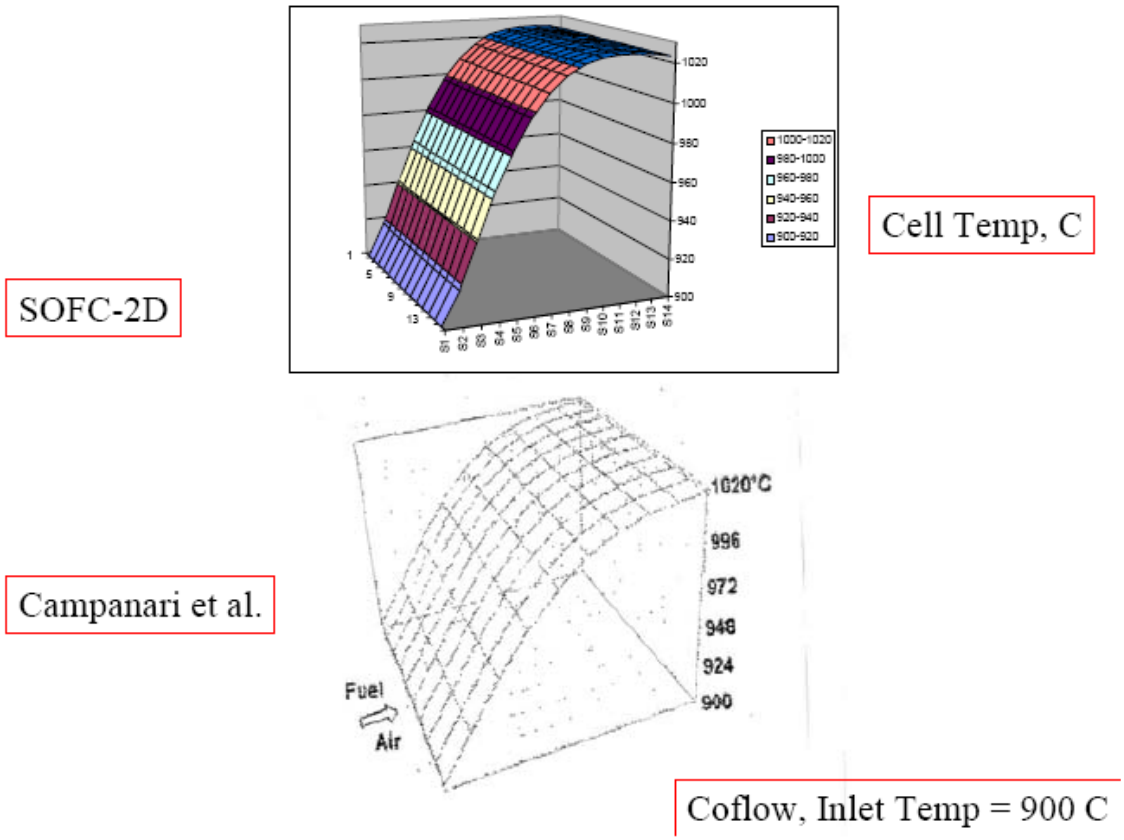

Figure 3.22 Cell temperature maps, co-flow.

Figure 3.23 shows current density maps for co-flow configuration from SOFC-2D code (top) and Campanari et al (bottom). Both codes predict a max current density near inlet. Note that SOFC-2D code predicts a higher current density peak value compared to Campanari et al.

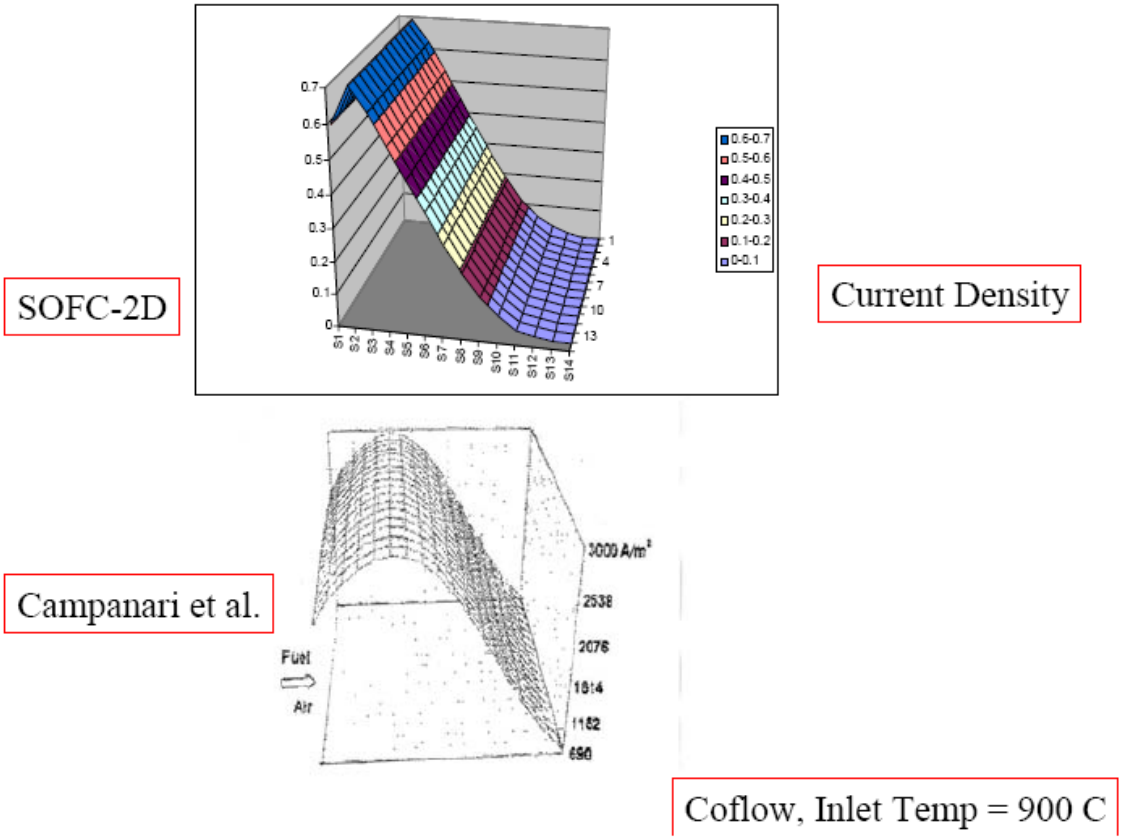

Figure 3.23 Current density maps, co-flow.

Figure 3.24 shows current CH4 mole fraction profile along the cell for co-flow configuration from SOFC-2D code (top) and Campanari et al (bottom). Both codes predict a total CH4 consumption in the first 20% cell length.

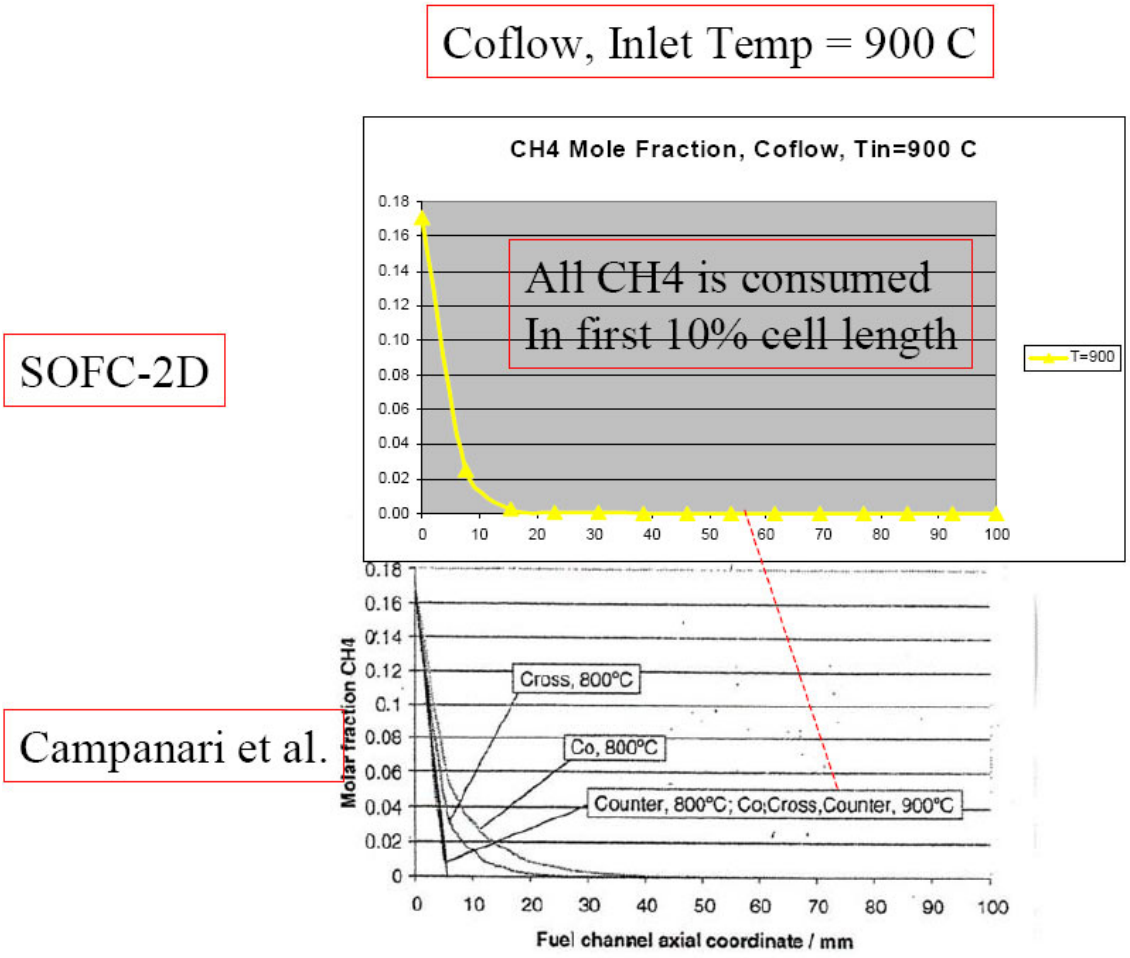

Figure 3.24 Along-cell CH4 mole fraction profile, co-flow

Figure 3.25 shows current H_2O mole fraction profile along the cell for co-flow configuration from SOFC-2D code (top) and Campanari et al (bottom). Both codes predict H_2O mole fraction to decrease at the cell entrance due to steam reforming reaction to reach a bottom and then starts increasing, as electrochemistry reaction is more dominant to reach 80% mole fraction at the exit.

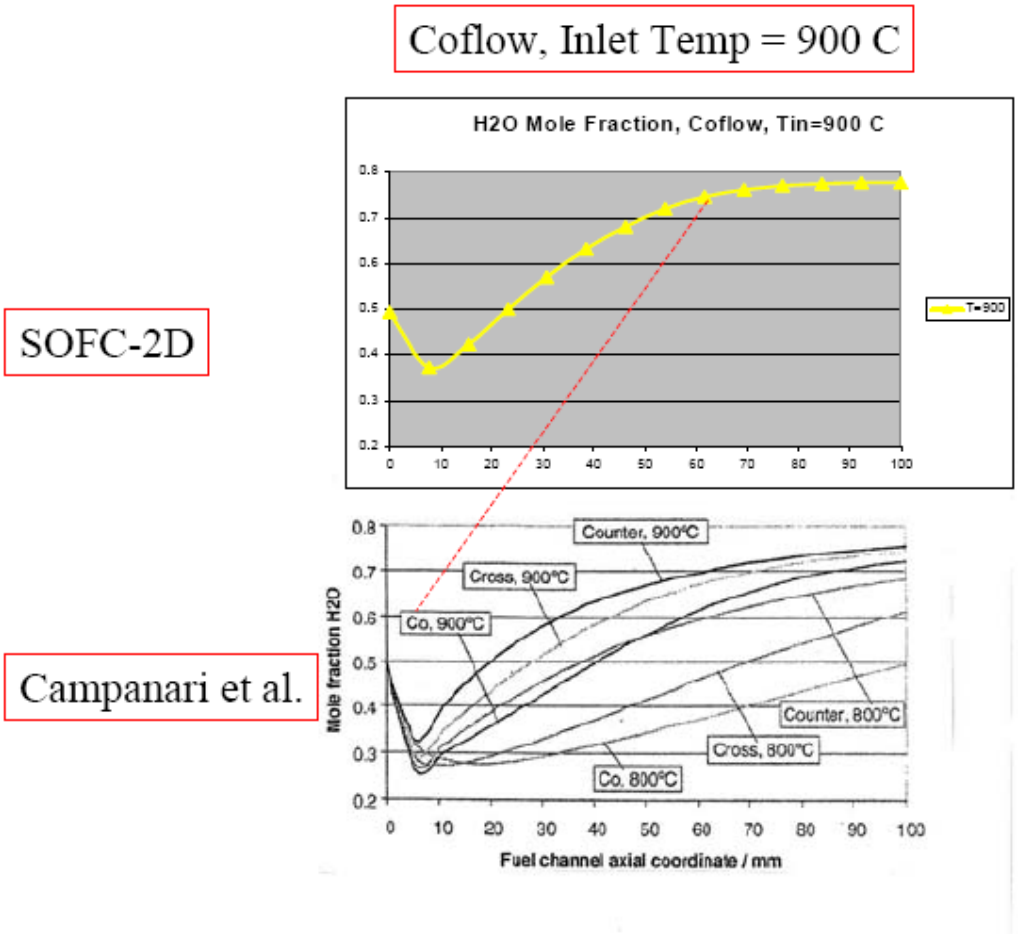

Figure 3.25 Along-cell H_2O mole fraction profile. Co-flow.

Figure 3.26 shows current H_2 mole fraction profile along the cell for co-flow configuration from SOFC-2D code (top) and Campanari et al (bottom). Both codes predict an increase of H_2 mole fraction near inlet (due to steam reforming) to reach a max value in the first 10% of cell length then to decrease as steam reforming reaction ends and H_2 is consumed in electrochemistry reaction.

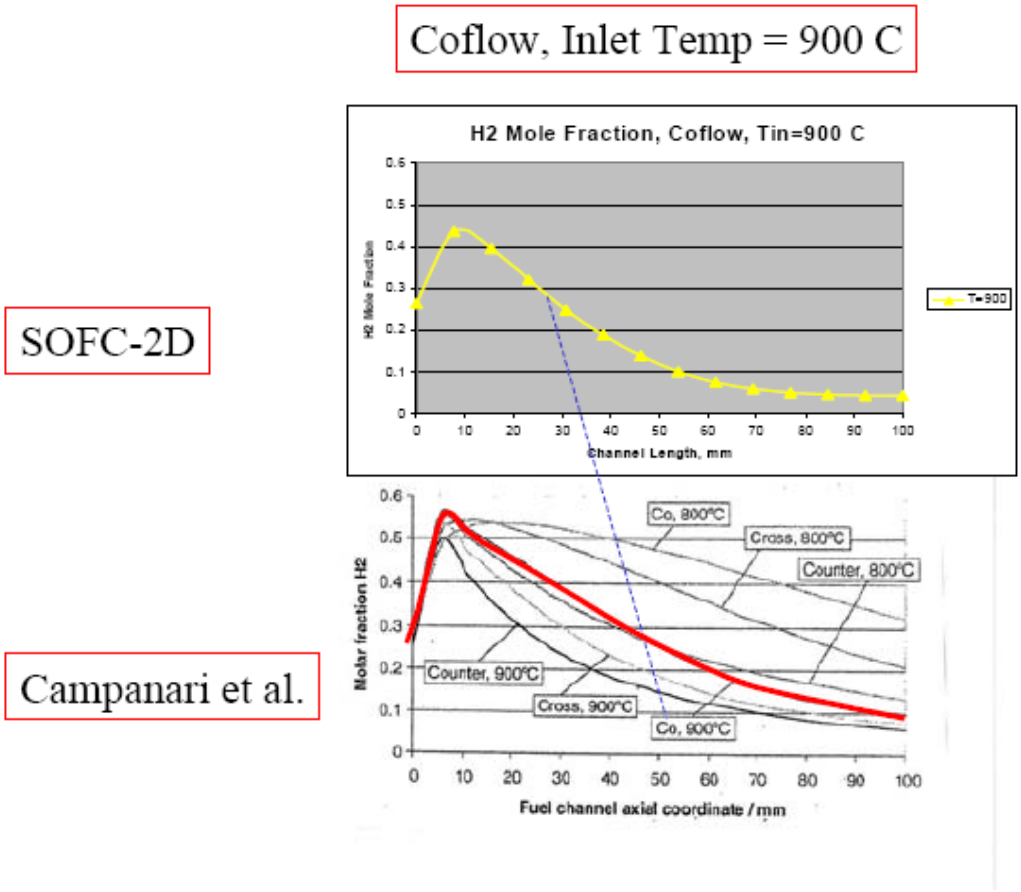

Figure 3.26 Along-cell H_2 mole fraction profile. Co-flow.

In summary

- SOFC-2D predictions compare very well with Campanari et al [2] work qualitatively and quantitatively.
- Peak values and locations also are close to literature predictions.

3.3.2 Effect of inlet temperature

The simulated cell is 100 x 100 mm = 100 cm^2 in a co-flow configuration. Anode and cathode inlet temperatures were 650, 800 and 900 C respectively. The fuel utilization was 85% while air utilization was 14%. The pressure is 1 atm, and the gas composition was H_2=26.26%, H_2O=49.34%, CH_4=17.1%, CO=2.94% and CO_2=4.36%. This type of reformate is relatively low in H_2 fraction (26.26%).

Figure 3.27 (top left) shows cell temperature profiles for different inlet temperatures. Note that increasing inlet temperature leads to a higher exist temperature but comparable cell dTs (122 C, 130 C and 129.5 C for inlet temp of 900, 800 and 650 C respectively.) The top right figure shows that @ 900 C inlet temperature, methane is completely consumed and faster compared to lower inlet temperatures, leading to higher H_2 peak values and production (bottom right

figure), but a lower fuel utilization (bottom left figure.) Note that in this simulation, current density (bottom left figure) reached a near zero value which is mainly due to the absence of CO electrochemistry in our model as evidenced in the high amount of CO (see Figure 3.28 top right).

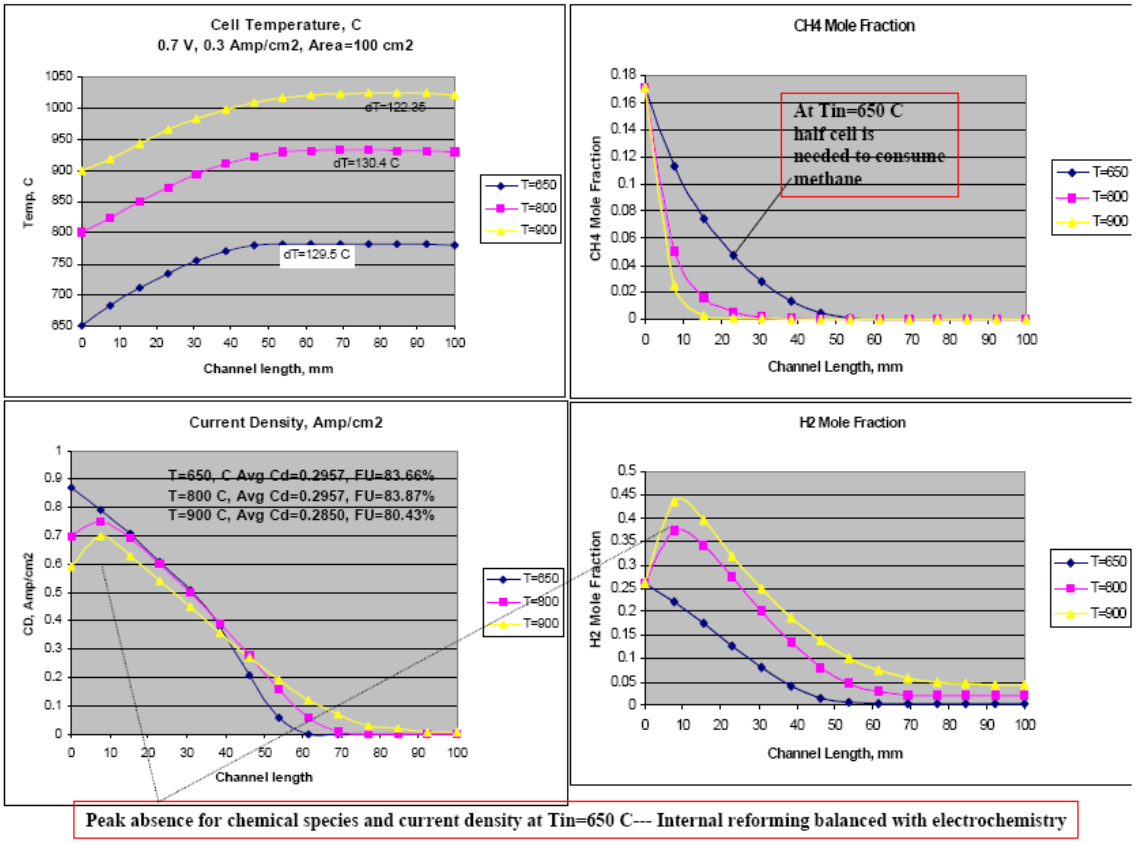

Figure 3.27 Effect of inlet temperature on Cell temperature (top left), Current density (bottom left), CH4 mole fraction (top right) and H_2 mole fraction profiles.

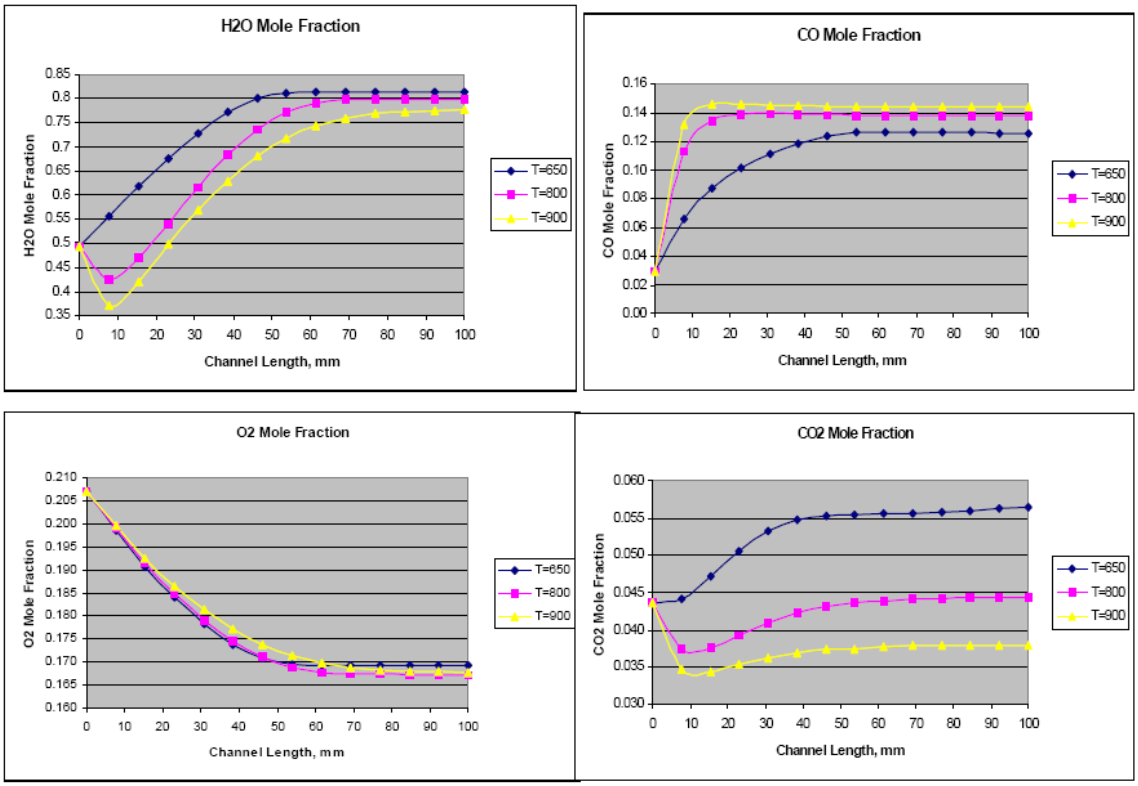

Figure 3.28 Effect of inlet temperature on H_2O (top left), O_2 (bottom left), CO (top right) and CO_2 mole fraction profiles.

In summary

- Higher inlet temperatures lead to higher cell temperature. However, the best performance (average current density and fuel utilization are obtained at lower inlet temperature—650 C)
- At 650 C inlet temperature, half-cell length is needed to consume all methane against only 15% cell length @ 900 C inlet temperature.

3.3.3 Effect of Internal Reforming

In this case the cell has a square geometry: 24" x 24" in a coflow configuration operating at a atmospheric pressure. Cathode and anode inlet temperatures is 650 C. The cell is simulated under 0.7 V with a fuel utilization of 80% and air utilization of 17%. The different gas compositions are included in the table below.

Figure 3.29 shows current density profile for different fuels showed n table above. The highest average current density (0.436 A/cm2) was obtained with reformate containing (53% H_2, 13.28% CH_4, 23.61% H_2O an 3.79% CO) followed by 0.433 A/cm^2 obtained with a mixture of 64% H_2 with N_2. Those two cases led to highest cathode air exit temperatures (870 C) as shown in Figure 3.30, compared to 810 C to 830 C for other fuels.

Mole Fraction %

Composition	H2	CH4	H2O	CO	CO2	N2	Cd (A/cm2
H2 - N2	64					36	0.433
CH4-H2O-N2	0	26.58	35.44	0	0	50	0.390
CH4-H2O	0	42.86	57.14	0	0	0	0.391
CH4-H2O	0	52.94	47.06	0	0	0	0.419
Reformate	53.11	13.28	23.61	3.79	2.41	3.79	0.436

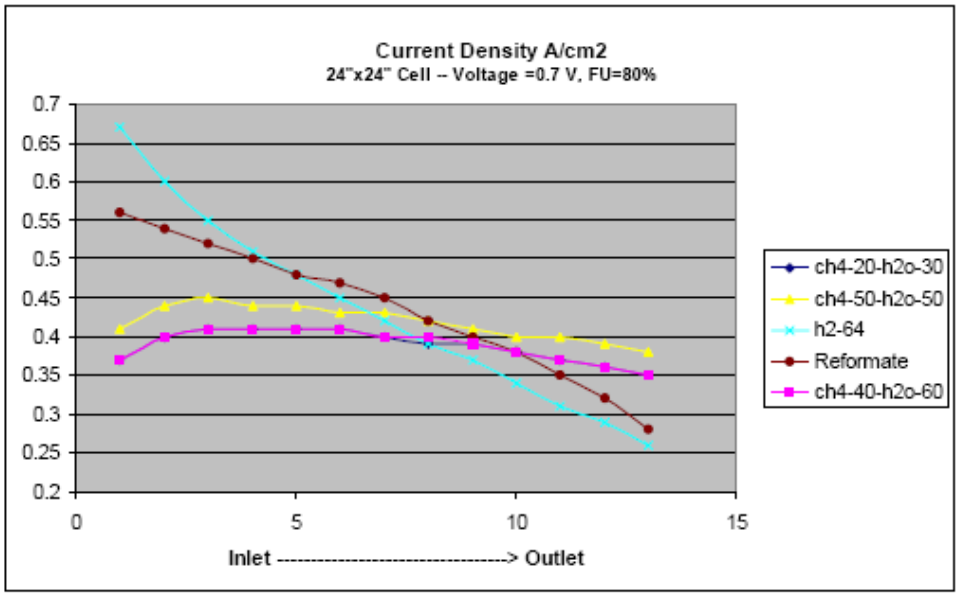

Figure 3.29 Current density profiles for different inlet gas composition.

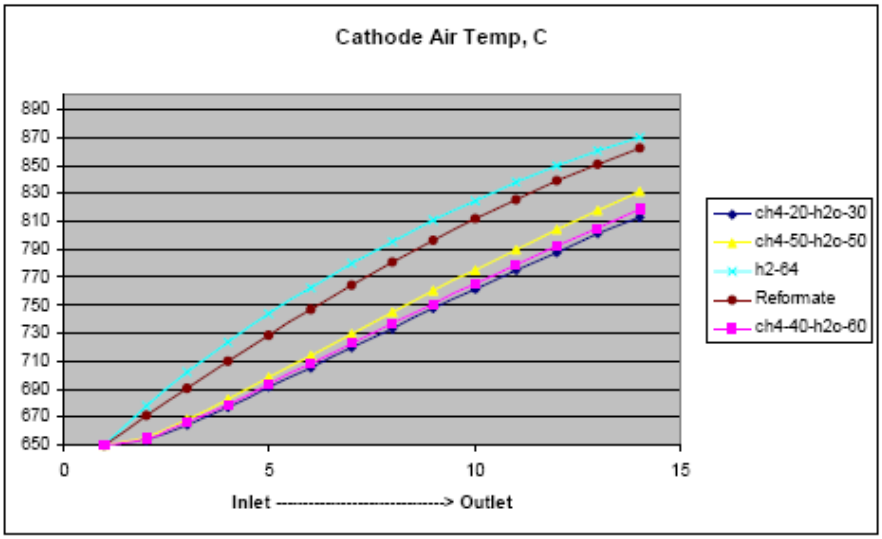

Figure 3.30 Air temperature profiles for different inlet gas composition.

In Figure 3.31, it can be seen that in all fuels containing methane, the conversion of CH4 was higher than 90% in all cases.

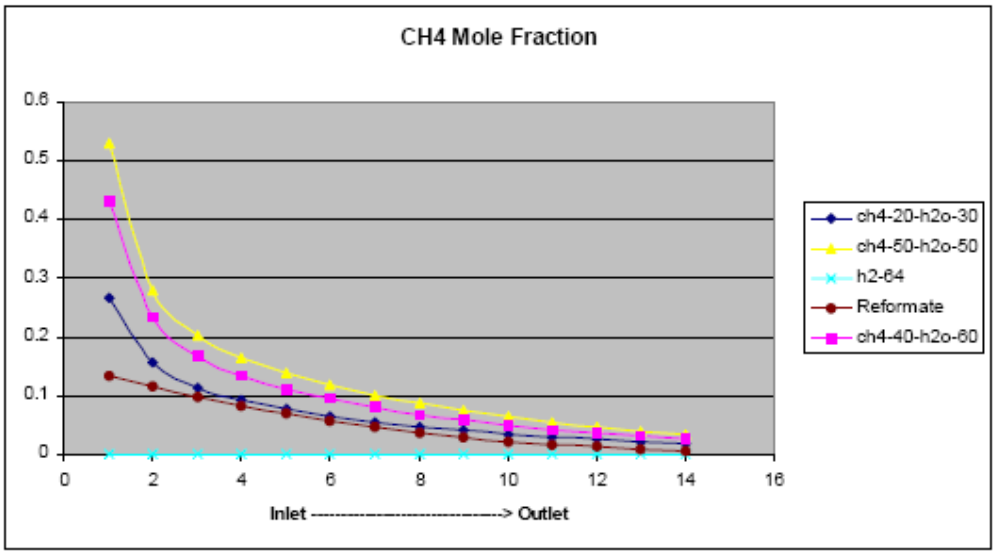

Figure 3.31 Methane mole fraction profiles for different inlet gas composition.

In summary

- Best performance are obtained with following gas composition (mole %): 53% H_2, 13% CH_4 and 24% H_2O.
- However a similar performance can be obtained with 64% H_2 (N_2 balance)

3.4 Cell manufacturing

3.4.1 Sintered cell manufacturing

Work was focused on three main areas, extrusion demonstration/validation, process modeling and sintering improvements. All of these area are key in the manufacturing process of SOFCs and both can have significant impact on the cost of a manufactured stack.

3.4.1.1 Extrusion

Work focused demonstrating the processibility of wide and thin ceramic sheets using direct extrusion at a scale on the order of that required by the proposed manufacturing process plan. There are several requirements referred to as Critical-to-Quality or CTQs addressed through this work, namely:

- Continuous, single step process to eliminate current batch mixing step
- Process feasibility for handling both mixing and shaping functionalities
- Process versatility to meet dimension requirements

The major challenges are primarily related to the material systems used for the cell fabrication. They are polymer systems highly filled with ceramic powers. Such highly filled polymer systems could cause equipment wear, dimension

instability and poor mixing quality in the final parts. In addition, the dimension requirement on the extruded sheets is a challenge as well. The extruded sheets for electrolyte have to be 24” wide and 0.012” thick while anode sheets need to be 24” wide and 0.037” thick.

In order to understand the material behavior and help determine the optimal process conditions and requirements on extrusion equipments (single or twin screws), we have organized the task into three areas:

1. Rheology characterization:
2. Modeling
3. Extrusion experiments

The primary finding based on comprehensive rheology tests and extrusion experiments is that extrusion as a continuous process is proved to be suitable process for manufacturing thin and wide electrolyte and anode layers. The twin-screw extrusion has been proved to be very stable, allowing high volume production and the produced sheets meet all targeted dimension requirements. It is also worthwhile to note that the current material system has been used without any modification in the extrusion process, which eliminates needs of costly material modification for better processibility.

Rheology measurement

Rheology is of critical importance for this task as it will provide us the material flow behavior under shear rates and temperatures that the material experiences in the extrusion process. It also provides an optimal temperature range within which material can flow easily without risk of degradation. The temperature and shear rate dependency of the flow behavior will guide us to determine the best process conditions under which we can achieves the best combination of flow and dimension stability. Another important material behavior, the visco-elasticity, can be also revealed by rheology test. The visco-elasticity can play an important role in final part dimensions. In sheet or profile extrusion, it often results the expansion at the die exit, also referred to as “Die Swell”. One has to understand and quantify this phenomenon to ultimately optimize the die design for highly elastic materials.

Generally, rheology tests can be classified into two categories, one deals with high shear rate and the other with low shear rate although both tests have some overlapping shear rate ranges. The high shear rate data are typically 22
obtained by capillary tests. They are used mainly to determine the viscosity of materials as functions of temperatures and shear rate. The low shear rate data has different purposes. The test is often done using parallel plate rheometry that involves oscillatory motions of one plate against a stationary plate. By controlling the frequency of the rotation, one can obtain very useful data on visco-elasticity of the material being tested. Three types of data can obtain by parallel plate rheometry:

• Viscosity as function of frequency which can be translated into shear rate under Cox assumptions
• Loss modulus which represents the viscous nature of the material
• Storage modulus which represents the elastic nature of the material

The rheology of the material systems developed for SOFC is quite complex. It's behavior is mainly driven by the high volume of ceramic loading. Normal thermoplastic materials typically exhibits shear thing behavior and reaches a plateau at the low shear rate at temperatures above Tg. At contrary, the highly filled polymers does not have a very defined melting temperature. In addition, the melt viscosity may increase exponentially as shear rate decreases.

Extrusion demonstration

An extruder manufacturer with a demonstration lab and the appropriate equipment was identified to run the extrusion trials. The company has significant experience in the design and manufacture of twin-screw extruders. Using the rheology data collected on the baseline materials a screw and port configuration was selected.

Electrolyte tape and a surrogate for the support anode (since the vendor was not equipped to handle nickel oxide powders, zirconia powders of similar particles size distributions were substituted for the nickel oxide in the tape formulation) were successfully extruded at widths of >10" and thicknesses ranging from 0.012" to 0.035". The upper limit on the thickness was controlled by the die design (maximum die opening) and the lower limit is in the range of the current calendering process output for electrolyte tapes. Photographs of the extruded tapes are shown in Figure 3.32. One important thing to note is that during these trials the formulation of the tape was not intentionally modified, due to feeder variations the ratios may be off at any one instance but the overall average feed rates were inline the required recipe. The only process change was that the material was mixed and extruded at a temperature higher than that which is currently used in the batch mixing process in the lab. The extruded samples did not show any deleterious effects of the higher processing temperature, but tests are planned to insure that this assumption is correct.

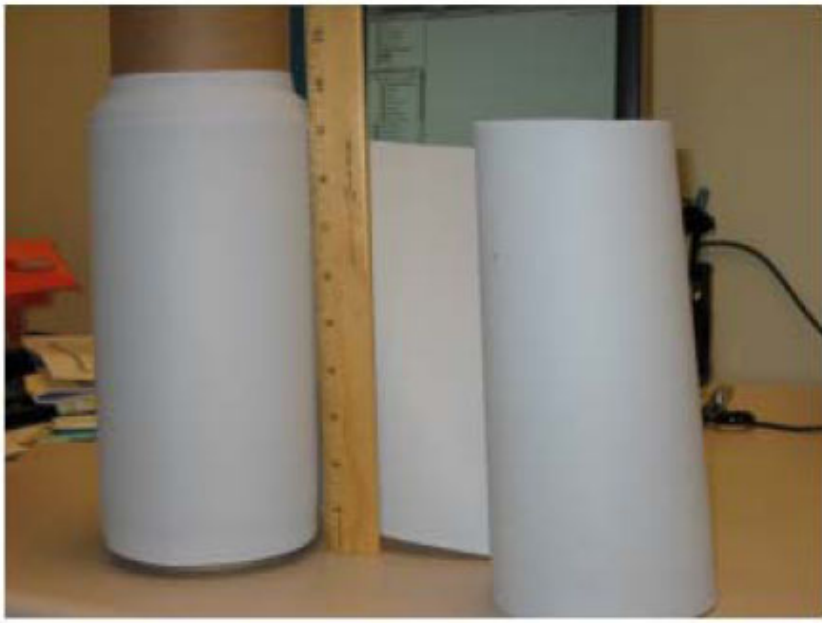

Figure 3.32 Extruded tape

One area of concern in this regard is bubble formation in the green tape. Bubbles are seen in the lab processed tapes and so a set of experiments relating to tape bubble formation has been completed. During the processing of laminated layers that make up the bilayers, bubbles form in anode and electrolyte material. These bubbles are visible to the naked eyes, with some as large as ½ inch in diameter. While the consequences of the bubbles remain uncertain, such as impact on manufacturing yields and cell performance, they require additional and/or modified processing to reduce/remove them. Due to these additional manufacturing steps, throughput and labor content is increased. In addition, the process requirements for extrusion and rolling in a high volume process may also exacerbate their formation. The focus of this study is to understand how these bubbles form in order to minimize their effects on downstream operations.

A series of experiments were performed to determine the root cause bubbling in anode and electrolyte tape during the calendering process. Three primary causes were examined; 1) Organic burn-off, 2) Moisture evaporation, 3) Air entrapment. To understand organic burn-off, thermal gravimetric analysis (TGA) and gas chromatography- mass spectrometry (GCMS) was used. TGA data was also used to understand moisture behavior in the material. Finally, the results from two different tape-manufacturing processes were compared to understand the plausibility of air entrapment in bubble formation.

The first theory was that during the mixing and rolling process, the organics in the tape were prematurely vaporizing/decomposing, thus causing bubbles to form. From the TGA and GCMS data, it is unlikely that organic burn-off occurs at the low mixing/calendaring temperature when the onset of bubble formation is observed. That is not to say that bubbles can’t form at higher temperatures when

organic burn-off occurs. These experiments only focused on the bubbles formed at the mixing/calendar processing conditions.

The first study was to determine if organic burn-off is the cause of bubble formation in the tapes. Both the anode and electrolyte tape contains organic compounds, such as binder and plasticizer (and other additives). It is possible for the binder and plasticizer to vaporize during tape processing. This vapor could build up in pockets in the tape to form bubbles. This scenario seems likely due to the relatively high vapor pressure of both the plasticizer and binder decomposition constituents From the results obtained during this reporting period, it is concluded that the tape bubbles most likely did not form from organic vaporization. With organic burn-off ruled out as a cause of bubble formation at processing temperature, we look at moisture as a possible cause.

To determine whether moisture is the cause of bubble formation, it is first to need to determine whether moisture exists in the tape. It is second to need to isolate whether the moisture is causing the bubbles. Performing TGA on several samples of material, starting with the raw material constituents to the final bilayer tape, achieves the first objective. A tell-tale sign that moisture is being driven from the material is an initial weight loss at low temperature from the TGA data. The hydroscopic material(s) is identified (if it exists at all) and substituted with a non-hydroscopic material. This should remove the formation of bubbles, if moisture is indeed the sole cause.

Several different materials were examined to determine their tendencies to absorb and retain moisture. The focus was on certain organic materials and everything that use. Two methods were used to determine the level of moisture content in the material. The first is a standard TGA, with some heat up rate (°C/minute). Weight loss at low temperature up to 200°C is a good indicator of moisture, since that is the temperature range when water evaporates. A second method cycles humid/dry air to the sample. The sample was dried under a ~0% relative humidity (RH) nitrogen purge at 150°C then cooled to 30°C. The sample was then cycled from ~0%RH (liquid nitrogen boil off) to ~45% RH at hourly intervals. If the sample is hydroscopic, then it will gain weight from picking up moisture from the humid air. Finally, to confirm any moisture findings, Pyrolysis mass spectra is used to detect moisture that is driven off the sample as it is heated.

From all of the TGA and GCMS data, it can be concluded that certain organic materials used in tape formulations are hydroscopic. This is true for extruded and non-extruded material. With this information, some conclusions can be drawn between moisture content and bubbles in the material. Moisture may contribute to the bubble problem, but it cannot be the sole cause behind it. A possible explanation lies in how the material is processed. Processing tape in a way that traps air pockets in material may be contributing to the formation of the bubbles. There must be another mechanism for bubble formation, if not the only

mechanism in this study. This mechanism may be air entrapment during the processing of the tape, specifically the mixing and calendaring processes. 25 Experimental observations will show that air entrapment is the primary cause for bubble formation.

Thus far, data has shown that organic burn-off is probably not the cause of bubble formation. Moisture is also ruled out as the sole cause of the bubbles because even non-hydroscopic material has them. The key is seen in two tape samples that were processed differently. One tape is done with the standard mix and calendar process. We'll call this the non-extruded sample. The other is extruded from a two-screw extruder. Both samples have the same organic composition. Both are hydroscopic.

In the extruded anode tape, no bubbles are initially visible. Since the tape is hydroscopic, bubbles should eventually form if moisture is a cause of the bubbles. The extruded tape is calendered, without folding, from a thickness of 32 mils to 20 mils. If this were non-extruded anode, bubbles would be present by now. This is not the case for the extruded anode tape, as it remained bubble-free after calendaring. Only when the extruded anode tape was folded and calendared, did bubbles begin to form. The tape was folded several times and thinned down to the starting thickness of 32 mils. The folding of the bubbles initiated the formation of the bubbles.

This experiment was repeated with an extruded electroltye tape with 12 mils initial thickness. This tape is not hydroscopic. Like the extruded anode tape, the extruded electrolyte tape did not have any visible bubbles initially. Like the extruded anode tape, the bubbles formed only when the tape was folded and calendared.

These experimental observations indicate that air entrapment is the likely cause of tape bubbles. Extruded tapes do not have bubbles initially because the high pressure of the extrusion process displaces any existing bubbles in the material before it comes out of the die lip. The bubbles are only re-introduced back into the tape by the folding and subsequent calender process. The folding process entraps air in pockets formed by the folded material.

The second area of focus this period was focused on reducing the sintering cycle time since sintering cycle time have a significant impact on manufacturing plant capital cost. Many factors must be considered when designing a sintering cycle such as, moisture removal, organic burnout, phase changes and thermal. The sintering cycle must be tuned for each event takes so that they occur a rates that prevent the green part from cracking or warping during the sintering process.

The current firing cycle used for large cells (12" final size) is quite long. Failures due to binder removal are seen using this long cycle, indicating that the program needs to be modified. Also, this long cycle is not feasible in a scaled up process

as shown by the current cost model. The focus of this study was to understand each critical reaction that takes place in the ceramic cell during sintering and to optimize the firing cycle to account for these reactions.

Thermogravimetric analysis (TGA) was used to generate a thermal fingerprint of each raw component and the calendared bilayer tape. The results of the thermal analysis study were used to modify and shorten the firing program with successful results. However, further program modification is possible and should be continued in the future.

Based on the thermal analysis data, it became evident that the firing cycle could be modified to closely match the actual binder removal of the sample. This should allow the parts to be sintered in a reduced amount of time without negatively affecting yield.

The current firing cycle for 12” bilayers has been successfully used in both electric and gas furnaces. The furnace is programmed for 151.5 hours cold-to-cold, however the furnace cannot cool down as quickly as programmed. Therefore, the true cycle time is closer to 170 hours cold-to-cold. For test purposes the focus was only on optimizing the heat up and soak portion of the cycle. From historical data, the ceramic cells can tolerate aggressive cool down rates and the final cool down program will be based on the sensitivity of the kiln furniture rather than the cells.

During this period, three samples were prepared with different cycles. All three samples were successfully sintered. Although the parts were 100% intact, some discoloration was visible. This anomaly has not been seen before, and further analysis is needed to understand the nature of the discolorations.

3.4.1.2 Rolling development

The objective was to understand the better understand the rolling process in order to predict the production cost and throughput while maintaining the required quality of the green laminated tape. What was done to address this is:

- A new rolling process was proposed; that is, using the continuous rolling (instead of the manual rolling) to fabricate the layered cell sheets.
- Feasibility of the continuous rolling process was studied.
- Thermal and mechanical behavior of all the four green cell materials was investigated.
- The finite element, fully-coupled thermal and stress models (ABAQUS Explicit) for both the current rolling operations and the continuous rolling were built.
- Computer models were used to investigate the rolling behavior of the cell materials.
- The full design of experiment (DoE) method and the computer models were used to design the process windows of the continuous rolling lamination.

3.4.1.3 Investigation of Green Cell Material Properties

To study the feasibility of the continuous rolling process, it is needed to investigate the mechanical and thermal properties of the green tape of all the four cell materials (Electrolyte, PAL1, PAL2, PAL3) as well as the dependency of the properties on process conditions, such as temperature and velocity.

The properties investigated (and tool/process used) are:
o Visco-plasticity (Tensile & Compressive Tests)
o Visco-elasticity (DMA)
o Density (Scale)
o Thermal expansion (TMA)
o Specific heat (DSC)
o Thermal conductivity (Laser Flash Analyzer)
o Glass temperature (DSC)

Since the visco-plastic behavior is most important property to the continuous rolling process, only the tensile and compressive tests will be discussed.

The tensile samples are depicted in Figure 3.33. They were fabricated by water-jetting and the tensile tests were performed using a MTS machine. For each of the four green cell material, the tensile tests have done under five test temperatures (RT, 35 °C, 50 °C, 60 °C, 80 °C) and three test speeds (0.00025in/s, 1 in/s, 10 in/s). The typical tensile true stress-strain curve is shown in Figure 3.34.

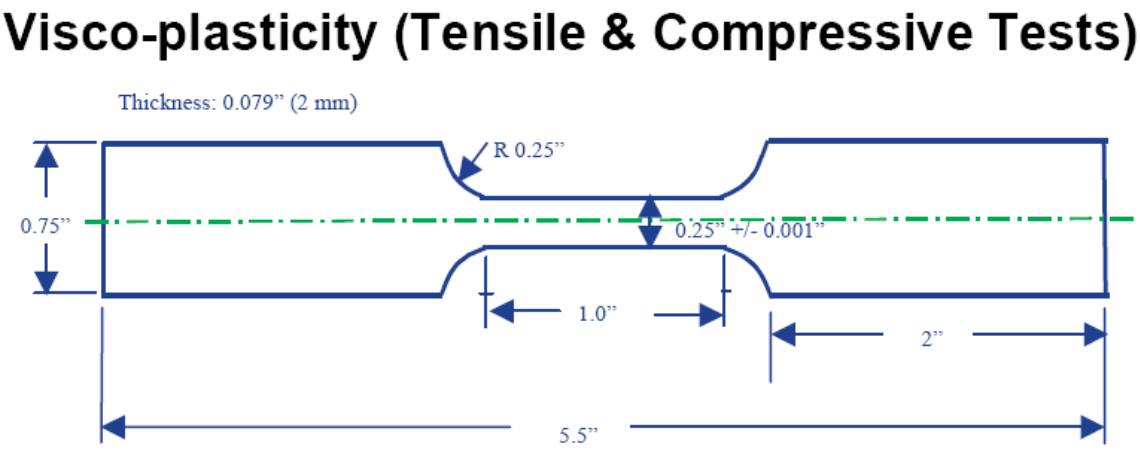

Figure 3.33 Tensile sample

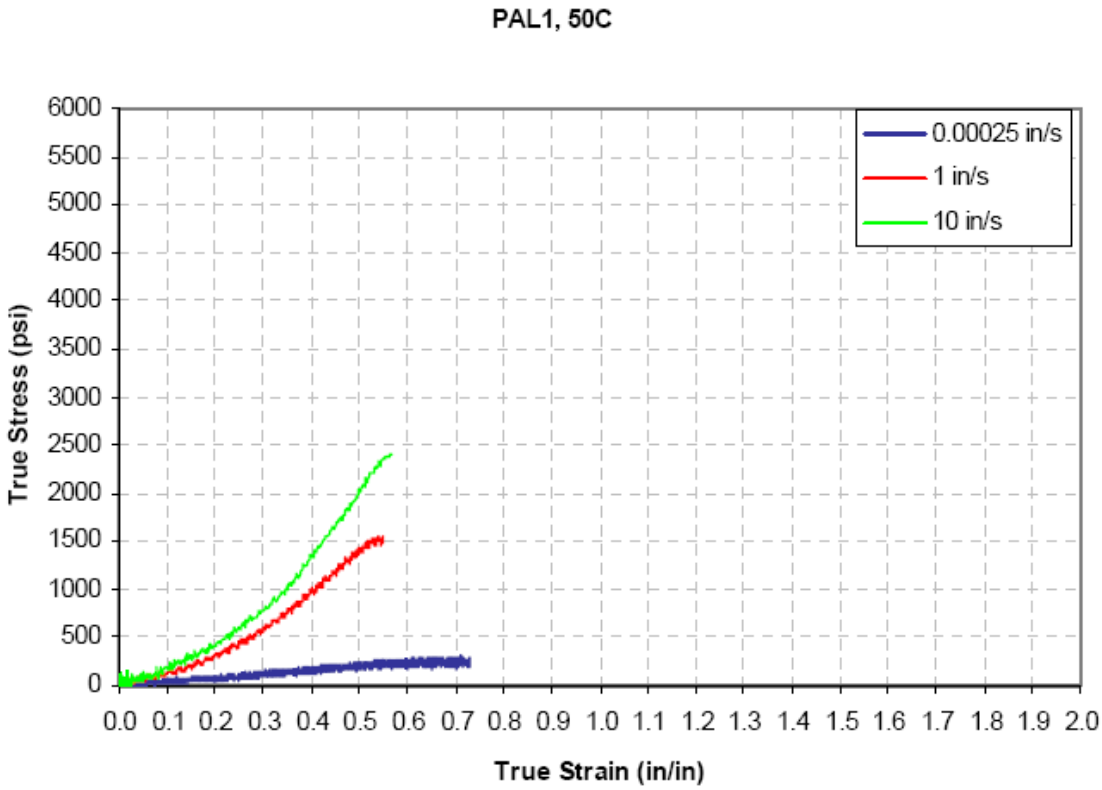

Figure 3.34 Typical tensile true stress-strain curve

It is found from the tensile tests that the current green materials, without any composition modification, have good visco-plasticity behavior when the test temperature (> 60 °C) is higher than the glass transition temperatures; such behavior is very importance for low cost and high volume production of cell sheets. Particularly, the electrolyte samples exhibit super-plasticity when temperature is higher than 60 °C (see Figure 3.35).

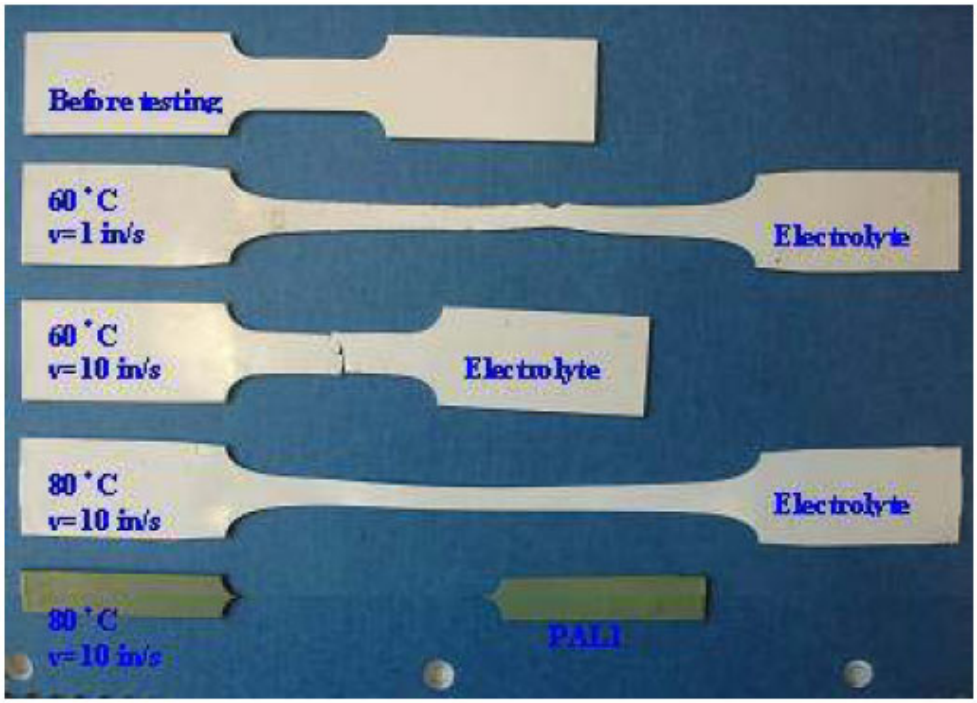

Figure 3.35 Super-plasticity Behavior

The compressive tests were also done using the MTS machine under test conditions of five test temperatures (RT, 35 °C, 50 °C, 65 °C, 80 °C) and five test speeds (0.00025in/s, 0.025 in/s, 0.25 in/s, 1 in/s, 2 in/s). The sample diameter is about 0.5 in and the height is about 0.25 in. The typical compressive true stress-strain curve is shown in Figure 3.36.

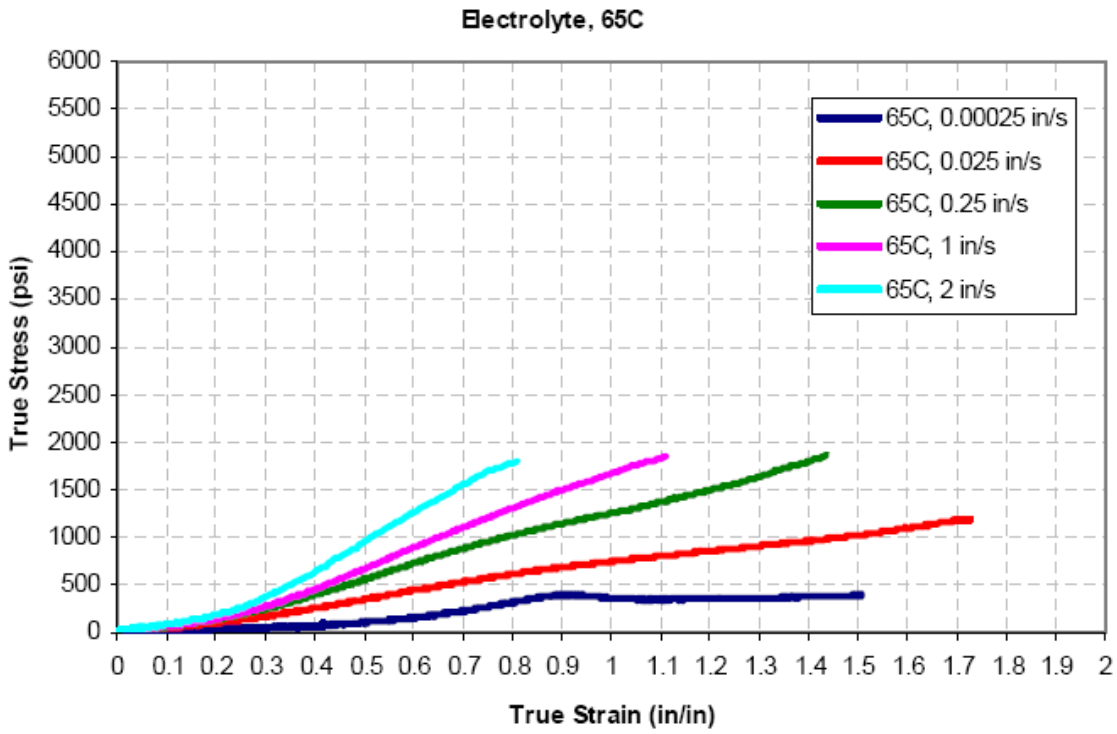

Figure 3.36 Typical compressive true stress-strain curves

Good visco-plasticity behavior of current green materials was also demonstrated by the compressive test when the test temperature (> 60 °C) is higher than the glass transition temperatures The demonstrated good visco-plasticity behavior of the green cell materials is critical to the continuous rolling process of the SOFC cells.

Finite Element Model of the Rolling Processes

Finite element, transient, fully-coupled thermal and stress model (ABAQUS Explicit) has been built for both the current rolling operations and the continuous rolling lamination. The model includes all the physics in rolling, such as:

- o Reduction By Rolling Motion, Elasto-plastic Deformation & Strain Rate Sensitivity
- o Large and Localized Deformation
- o Temperature-Dependent Friction and Contact Between Roller and Plate/Sheet
- o Cracks
- o Heat-up From Friction and Deformation and Heat Exchange With Environment

And by building/using the following corresponding models:

- o Elasto-Visco-Plastic Model
- o Adaptive Local Remesh Technique
- o Friction Model & Kinematic Contact Algorithm
- o Crack Generation Criterion
- o Heat Generation Model from Friction and Deformation & Coupled Heat Transfer-Deformation Modeling

The basic finite element functions are:

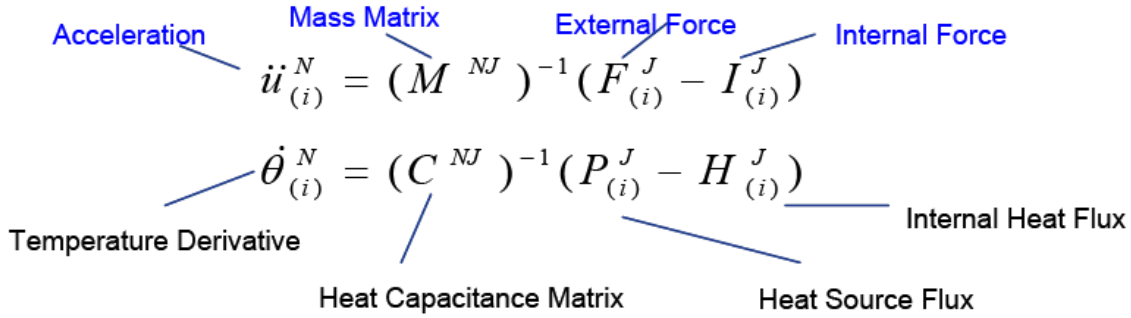

The inputs of the model include:
o Finite Elements and Nodes, Generated from Geometry
o Material Properties (vs. Temperature)
o Mechanical Properties – Elastic moduli, Poisson ratio, Rate-dependent stress-strain curves, Thermal extension coefficient
o Thermal Properties – Specific heat, Thermal conductivity
o Density
o Contact Properties
o Contact Surface Pairs
o Friction Coefficient
o Friction-generated Heat Ratio
o Heat Transfer Coefficient Between Contact Surfaces
o Deformation-Generated Heat Ratio
o External Force/Pressure, if know
o External Heat Source
o Crack Criterion
o Initial and Boundary Conditions
o Constraints
o Speed/displacement
o Temperature
o Heat Exchange with Environment – heat transfer coefficient, radiation emissivity

The model can provide the following outputs vs. time:
o Deformed Shape, Displacement and Velocity Distribution
o Stress, Total and Plastic Deformation Distribution
o Crack Indication
o Total Force/Torque Required
o Temperature Distribution

Process Window Designs of Continuous Rolling of SOFC Cells
Using the DoE method and the developed computer rolling models, the process windows of the continuous rolling operations for fabricating the SOFC cells have been designed. Full DOE design technique was used. The CTQ's of the process window designs of the continuous rolling of SOFC cells are:

o Quality of the rolled tape – No cracks & Maximum temperature less than 91 °C (195 °F), and
o Production cost – The least rolling passes

The crack initiation criteria of each cell material, described in Table 3.7, are based on the critical strains of cracks obtained from the compressive tests.

Table 3.7 Critical strains of cracks

T (°F)	Electrolyte Crack Strain		PAL 1 Crack Strain		PAL 2 Crack Strain		PAL 3 Crack Strain	
122	0.5	0.6	0.79	0.9	0.79	1.1	0.57	0.85
149	1.2	>1.5	0.83	1.2	> 0.79	>1.2	> 0.73	>1.0
176	> 2	>2	> 0.83	>1.2	> 0.79	>1.2	> 0.73	>1.0
Strain Rate (1/s)	> 10	1 ~ 5	> 10	1 ~ 5	> 10	1 ~ 5	> 10	1 ~ 5

Process Windows of Continuous Thinning of Electrolyte Tapes

The initial electrolyte tapes were assumed to be produced from a continuous extrusion process. The full DoE design was used:

• DoE - Xs: Roller/initial plate temp (T)
Rolling speed (V)
Initial thickness (H)
Total passes – 1, 2, 3
• Other Parameters: Roll diameter - 13.375 in
Final tape thickness - 12 mils
Friction coefficient - 0.3
• DoE - Ys: Max. Total rolling force (F)
Maximum temperature (Tm)
Maximum delta temperature (DT)
Maximum Reduction Strain (εy)
Maximum Mises Stress (σm)
Quality

As an example, Figure 3.37 describes the results for the case of 1 mm extruded sheet with a selected roller temperature, roller speed 9.75 in/s and 3 passes.

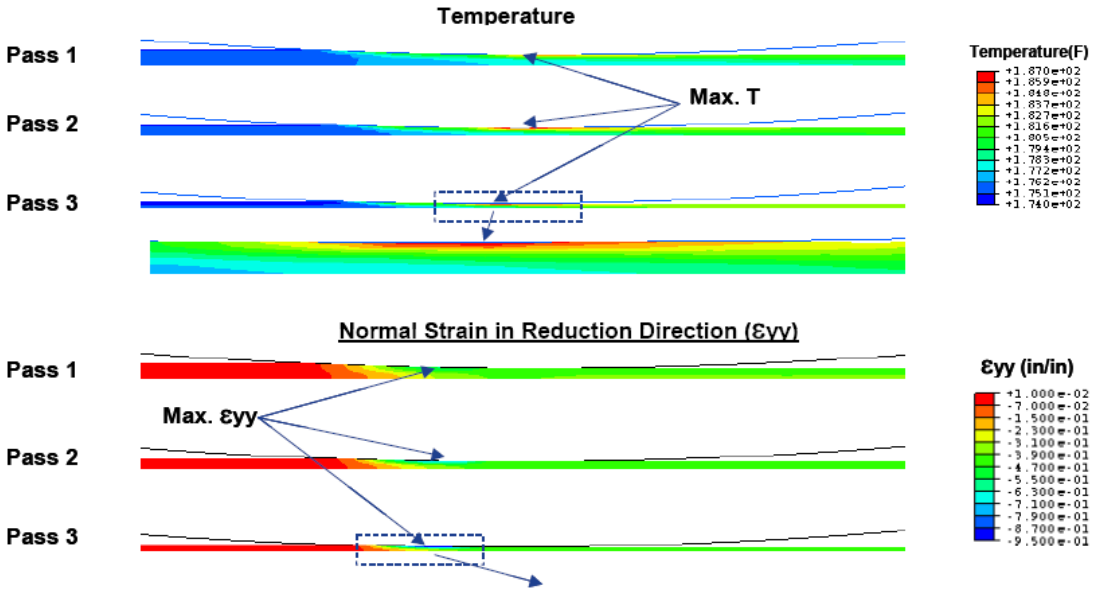

Figure 3.37 An example of the Continuous Thinning of 1 mm Electrolyte Tape

Based on the FEM work, it is concluded that

- o The current green materials, without any composition modification, have good visco-plasticity behavior when the production temperature (> 60 °C) is higher than the glass transition temperatures; such behavior is very importance for low cost and high volume production of cell sheets
- o The proposed continuous rolling process is feasible for low cost and high volume production of SOFC cells
- o The developed finite element, transient, fully-coupled thermal and stress model (ABAQUS Explicit) includes all the physics in rolling
- o Roller temperature is the most sensitive factor to determine the continuous rolling process windows
- o Higher roller temperature is better to both the lower rolling force (lower energy and then lower cost) and more uniform tape temperature (more uniform tape quality).
- o However, the higher roller temperature will lead to the more difficult to handle the tape during the production. To meet such a technical challenge, special designed handling tooling system will be required
- o The quality of the electrolyte is decisive for the process window design

3.4.1.4 Sintering yield

A key goal of the manufacturing process work is to increase sintering yields. Overall sintering process yield for 16.5” green bilayers is currently at 54%. To drastically increase sintering yield the fundamental causes of failure must be understood. Factors that have been studied in this reporting period are furnace, furnace position and recycled material used in anode layers were studied.

Current Process

All bilayers are currently fired on-site in electrically heated.. The furnaces have heating elements hanging on all four sidewalls. The walls are fiber lined and a small exhaust port is in the center of the ceiling. There is only one zone of control, and the control thermocouple is in an upper corner of the back wall. The hearth is also fiberboard, with a one-inch deck between the hearth and the first level of parts. A standard firing cycle used for each firing of large bilayer cells discussed here.

Current Yield

Processing data was collected on all large (16.5" green size) that were manufactured using the rolling process, sized and cut into a circle, and sintered on-site. A good part is defined as a part that is sintered 100% intact. A failure is any sintered part that has cracking, delamination, or edge tearing, regardless if the part can be trimmed after sintering to a usable size. The statistical process control (SPC) charts shown in Figure 3.38 displays the furnace yields.

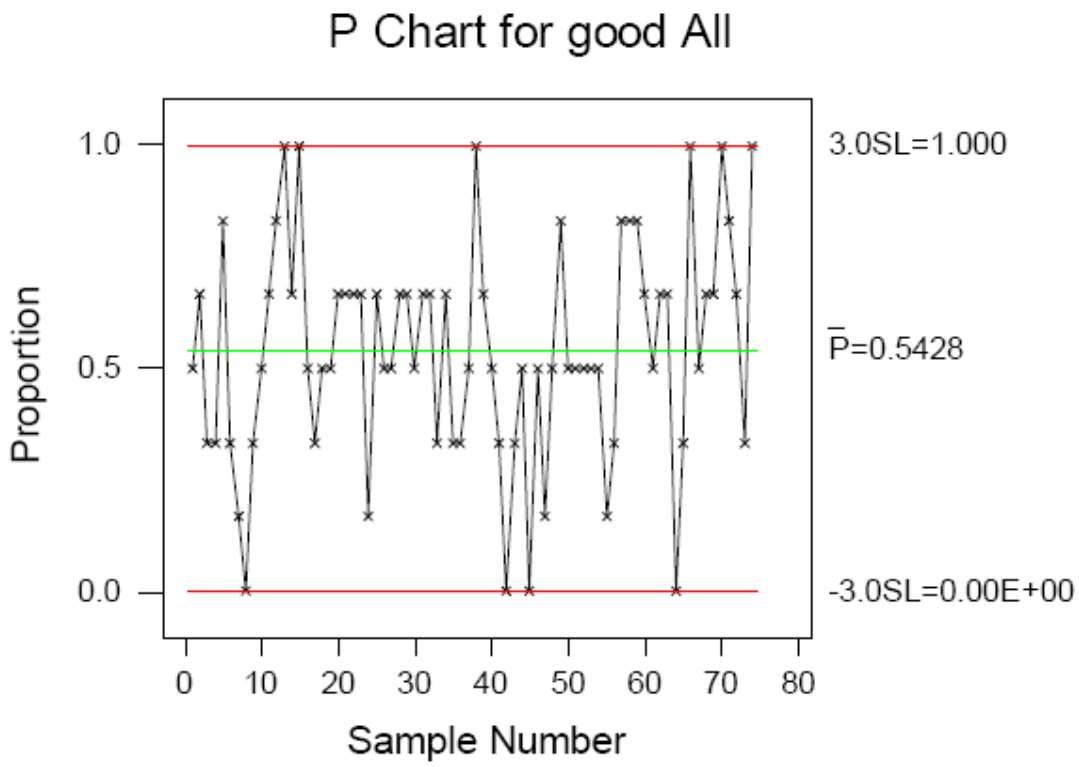

Figure 3.38 P Chart for All Furnaces

As evident from the run charts, overall firing yields were low throughout the year regardless of which furnace was used. The data indicated that which furnace the part was sintered in is not the major driver in yield. A deeper look in to the variables going into the firing step was required and was achieved by data mining the manufacturing database. The database contains parameters of each step of

the manufacturing process are measured and recorded. From this data sophisticated reports can then be generated to analyze the data.

Studies were carried out to investigate temperature uniformity for each firing, yield versus furnace position, and effect of recycled material on yield.

Conclusions from Sintering Yield Work

From the work that has been done to date on the sintering yield the following conclusions can be drawn:

- o Furnace position and rework of PAL3 are significant drive of yield
- o The current cost model uses a sintering yield of 64% as a baseline. From the analysis of the data it appears that this can be achieved, and even increased to a by improving temperature uniformity in the furnace and by eliminating the use of rework in the bilayers or remedying the root cause of the failures related to recycled material.

3.4.2 Deposited cell manufacturing

3.4.2.1 Mechanical characterization of deposited YSZ

This study was aimed at understanding the role of various thermal processes on the electrolyte coating stress during operation in a solid oxide fuel cell (SOFC). Understanding the electrolyte coating stress state is key towards preventing the cracking of the electrolyte layer in a SOFC. The modeling and experiments included in this study involve the air plasma spray (APS) deposited coatings on metal substrates. A series of experiments based on specimen location and temperatures (Figure 3.39) were carried out to characterize the electrolyte coating properties and also the substrate mechanical properties. This was used as an input for the numerical models. A non-linear parametric finite element model of the various layers of the solid oxide fuel cell was developed. The parametric finite element model was used to understand the stress buildup in the electrolyte layer as a function of the thermal loading history. The results from the numerical modeling helped in the understanding of the various mechanical factors involved in inducing thermal residual stresses in the electrolyte layer. The results further indicated the sensitivity of the final electrolyte stress state to the fixturing conditions during the APS deposition. It was found that the predicted maximum stress in the coating at operation changed from a mean value of 82 MPa to 26 MPa, when the fixturing condition during the simulated APS deposition was changed from two-sided support to single-side (cantilever) type of support. The numerical modeling in combination with the experimental strength data of the electrolyte coating indicated a shift in DPMO (defect per million occurrences) from 805,299 to 514,098 as we change the support conditions in the model to single-side support.

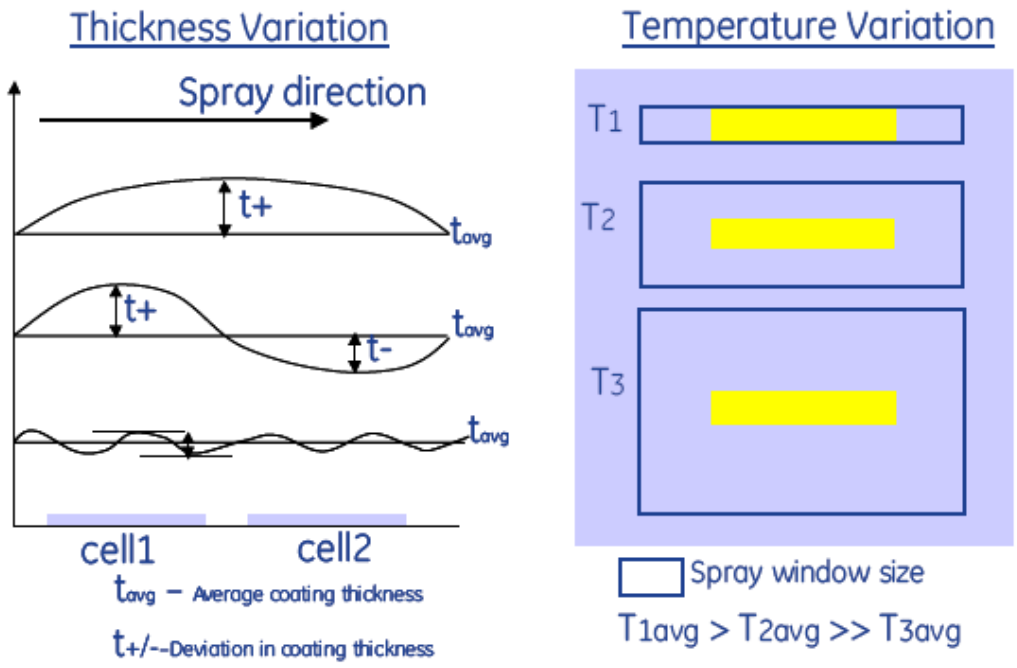

Figure 3.39 Schematic of the strip layout for the part location and part temperature study. In the right side schematic showing the part temperature study row-1(T1) can be varied by having the gun pass over the substrate at varying gun speeds keeping the window size same or the gun speed can be same and the window size changed as in shown in row-2(T1) and row-3(T3).

The deposited YSZ mechanical properties were characterized for the first time using a four point bending test. The YSZ coating was deposited using air plasma spray process onto foam substrates of 6.5mm width and 80mm length. The strips were coated first with a 30micron (1.2mils) anode (Ni-YSZ) and then with 50 micron (2mils) YSZ coating. The foam substrates were subsequently tested at room temperature in an Instron testing machine. The specimen was placed between the two support rollers with a span, L of 80 mm and the test machine crosshead was displaced at a rate of 12 mm/min to apply transverse load. The specimen was held in the test fixture so as to place the electrolyte coating under tension during the 4-point bend test. Before the beginning of the test the total specimen thickness and the length of the specimen were measured using a micrometer screw gauge. The load displacement curve obtained from the test was analyzed to obtain the bending modulus (E_b) and the failure strength of the coating (σ_f) (Figure 3.40).

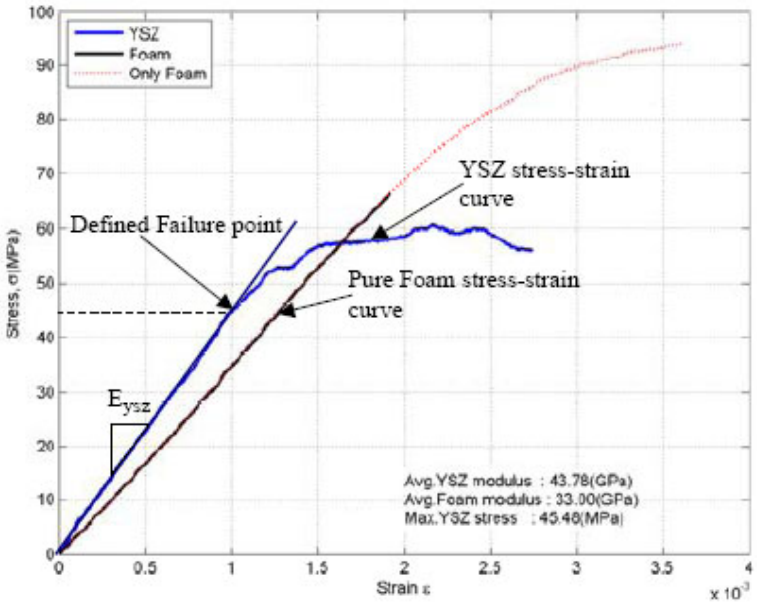

Figure 3.40 Typical Stress-strain response of the YSZ coating as derived from the experimental load-displacement curve of the composite specimen under 4-point bending load.

AFF-Series Summary

The AFF cells that were tested included AFF4, AFF8, AFF7, and AFF12. . Table 3.8 summarizes the performance of the AFF cells. In addition to the short term testing summarized in Table 3.8, both AFF12 and AFF7 underwent long term testing. These data are summarized in Figure 3.41.

Table 3.8 Performance summary for AFF-series cells

Part ID	Date	Power Density at 0.7 V (mW/cm^2)	Maximum Fuel Utilization (%)
AFF4	10/11/06	343	82
AFF8	10/11/06	385	79
AFF7	10/8/06 – 12/01/06	510	81
AFF12	10/08/06 – 10/30/06	410	80

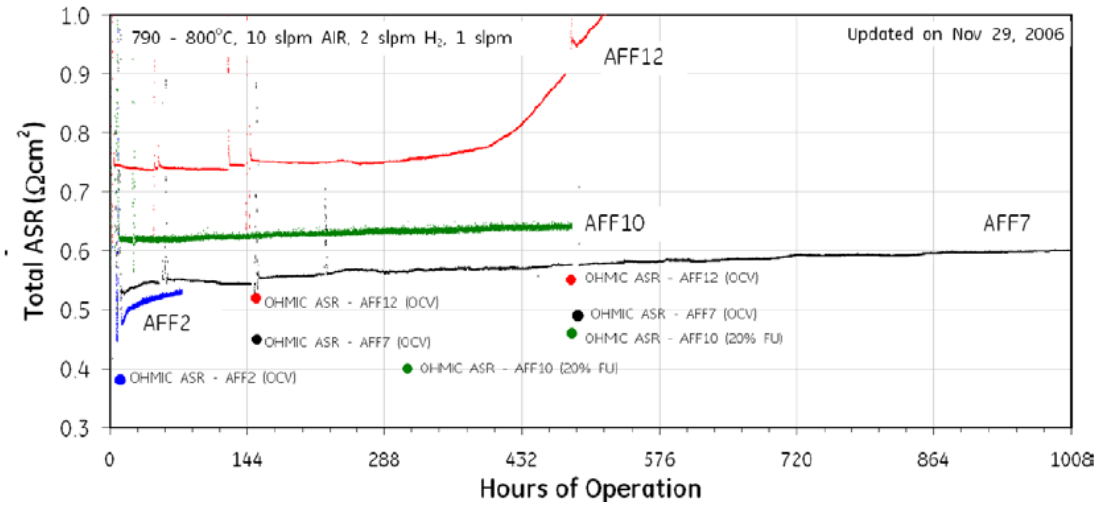

Figure 3.41 Total ASR as a function of time for AFF7 and AFF12. Also included is the ASR for comparable cells AFF2 and AFF10

T-Series Summary

The T cells that were tested included T208, T209, T210, and T211. Table 3.9 summarizes the performance of the T cells. As can be seen, cells T208 and T211 show dramatically better performance than their counterparts in terms of power density.

Table 3.9 Performance summary for TFF-series cells

Part ID	Date	Power Density at 0.7 V (mW/cm^2)	Maximum Fuel Utilization (%)
T208	11/16/06	406	Not taken
T209	11/16/06	105	Not taken
T210	11/21/06	133	Not taken
T211	11/21/06	420	Not taken

3.4.3 Seals

The seals must be chemically compatible with the other SOFC components during operation. Interaction between the seal and other components at fuel cell operating conditions could result in alteration of their physical and chemical properties, which may lead to seal failure affecting the stack performance. To understand the evolution of glass due to reaction between glass and the interconnect material (Ebrite, Allegheny Ludlum, PA), a washer sample (OD: 2.6″, ID: 2″) was prepared as shown in Figure 3.42. Two glass tapes with porous ZrO_2 cloth (ZOK15, Zircar Zirconia, Florida, NY) were sandwiched between two Ebrite plates and cured at 900 °C for 0.5 h in air according to the standard curing procedure. The ZrO_2 cloth had high open porosity, over 90%, and its thickness was 15 mils. Once the glass melts, it flows into the porous cloth and fills the pores because of capillary force, thereby preventing the glass from squeezing out during the heat treatment and forming a composite seal. After curing, the

sample was heated and held at 800 °C in air for 800 hr treatments with six thermal cycles totaling 4900 hrs under a 2 psi dead load.

Figure 3.42 Sample configuration to examine evolution of glass in air

As shown in Figure 3.43, the sandwiched sample was delaminated after the final thermal cycle. The glass – ZrO_2 cloth composite turned yellow, presumably due to the formation of Barium Chromate (BaCrO4). Figure 3.44 and 27 show XRD patterns obtained from the yellowish part (region A), and Ebrite (region B), respectively. The surface of the glass-ZrO_2 cloth mixture was mainly covered by $BaCrO_4$. $BaCrO_4$ is formed by the dissolution of Cr from Ebrite into glass followed by reaction with the Ba in the glass. $BaCrO_4$ formation is a big concern because its linear coefficients of thermal expansion (CTEs) at α_a = 16.5 ppm/K, α_b = 33.8 ppm/K, α_c = 20.4 ppm/K (a,b,c are the three crystal axes) in the temperature range 20 – 813 °C, are much higher than that of Ebrite, ~12 ppm/K or the typical anode-supported ceramic cell. Therefore the formation of $BaCrO_4$ eventually results in a separation between the sealing glass and interconnect due to the stress related to CTE mismatch and compromises the interface. $BaCrO_4$ was also observed with Cr2O3, Fe-Cr compound on the Ebrite (region B) surface as shown in Figure 3.45.

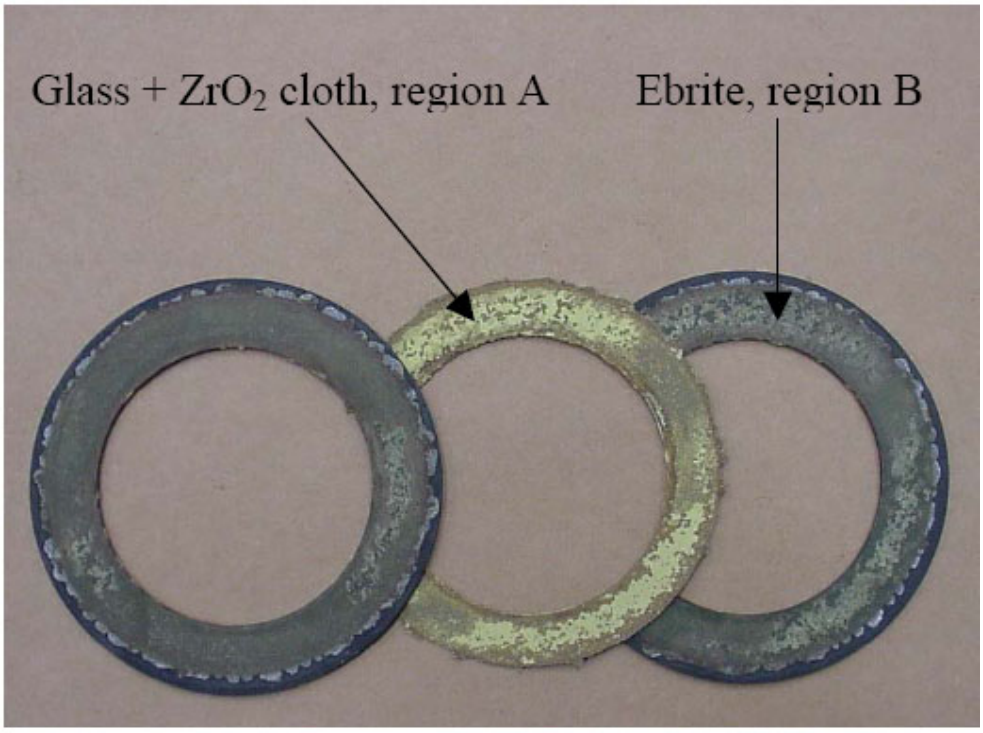

Figure 3.43 Glass – Ebrite sample after 4900 hrs at 800 °C in air

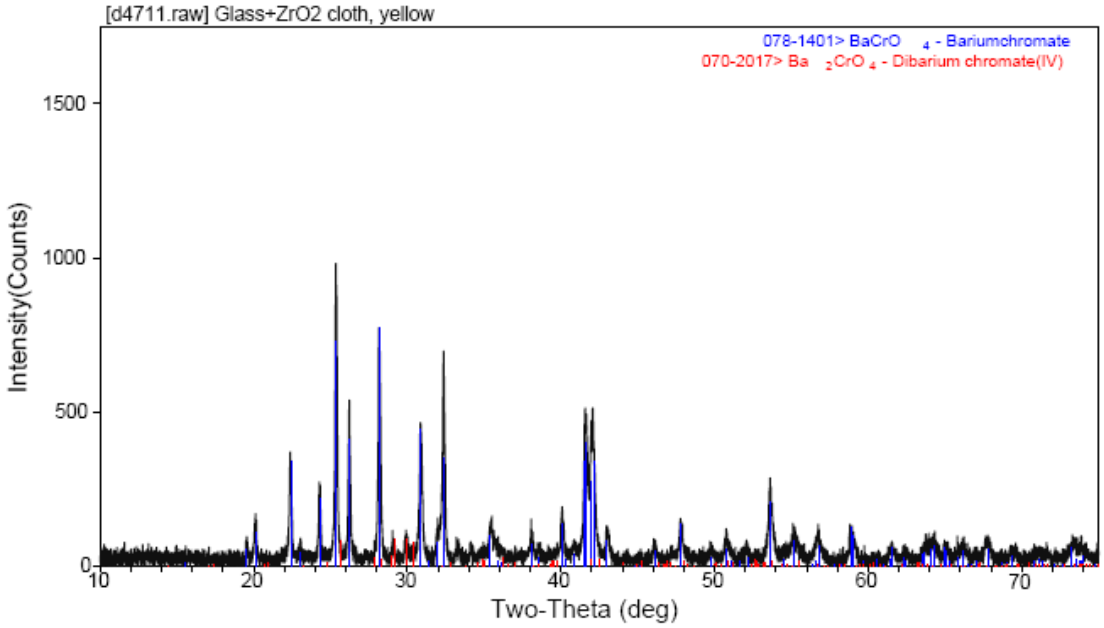

Figure 3.44 XRD pattern of Ebrite plate surface, region A

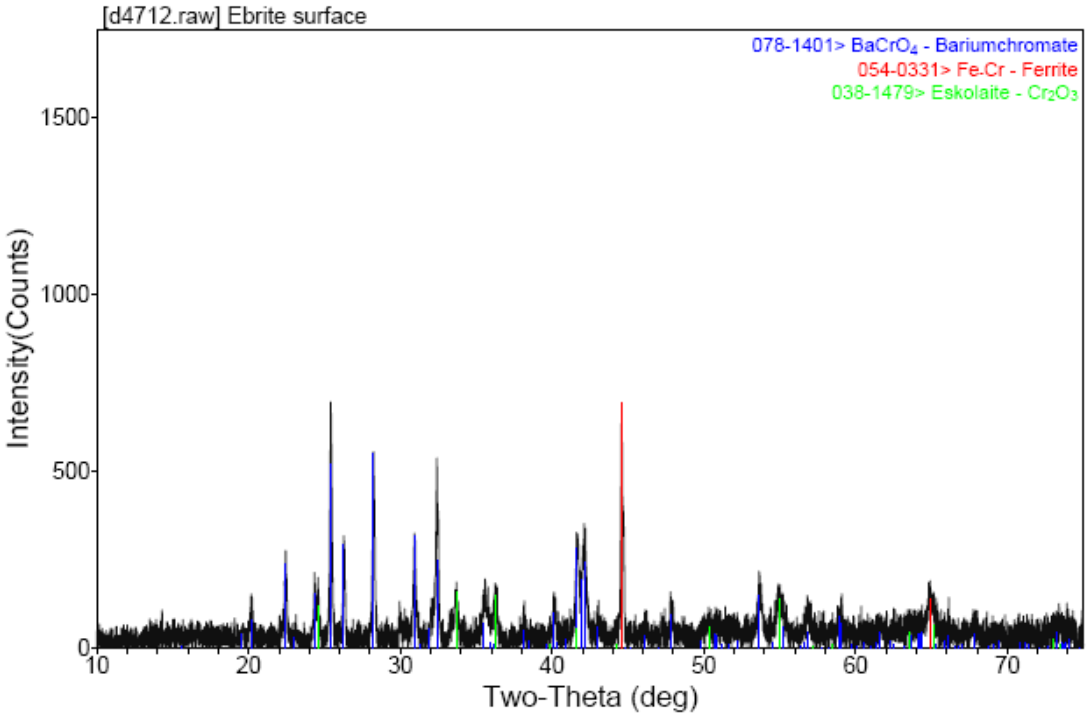

Figure 3.45 XRD pattern of Ebrite plate surface, region B

As a mitigation to prevent the formation of $BaCrO_4$, a yttria stabilized zirconia (YSZ) barrier coating on the interconnect by air plasma spray (APS) was evaluated. Here, prolonged degradation test was performed to evaluate the APS YSZ barrier coating up to 3000 hrs at 800 °C in air. The configuration of samples for the degradation test was similar to one shown above except that YSZ coated Ebrite plates were used. The YSZ barrier coating was about 50 μm thick and prepared using plasma spray by a local vendor. Although phase separation was observed in the sealing glass, $BaCrO_4$ was not found in the glass close to the Ebrite-YSZ coating interface. A BSE image of the sample after 3000 hrs shown in Figure 3.46 did not indicate any $BaCrO_4$ formation in the glass, which usually appears bright. Cr was not observed in the sealing glass as shown in the element mapping results in Figure 3.46, confirming that the YSZ coating prevents any $BaCrO_4$ formation. Presence of glass components detected in the YSZ coating layer is due to penetration of glass into the coating layer that has open porosity. Optimizing the YSZ coating conditions to get denser barrier coating could minimize that. EDS spectra of the regions A, B, and C marked in the figure showed that they are Ba-Mg-Si-O compound, presumably $Ba_2MgSi_2O_7$, Ca rich phase, and glass matrix, respectively.

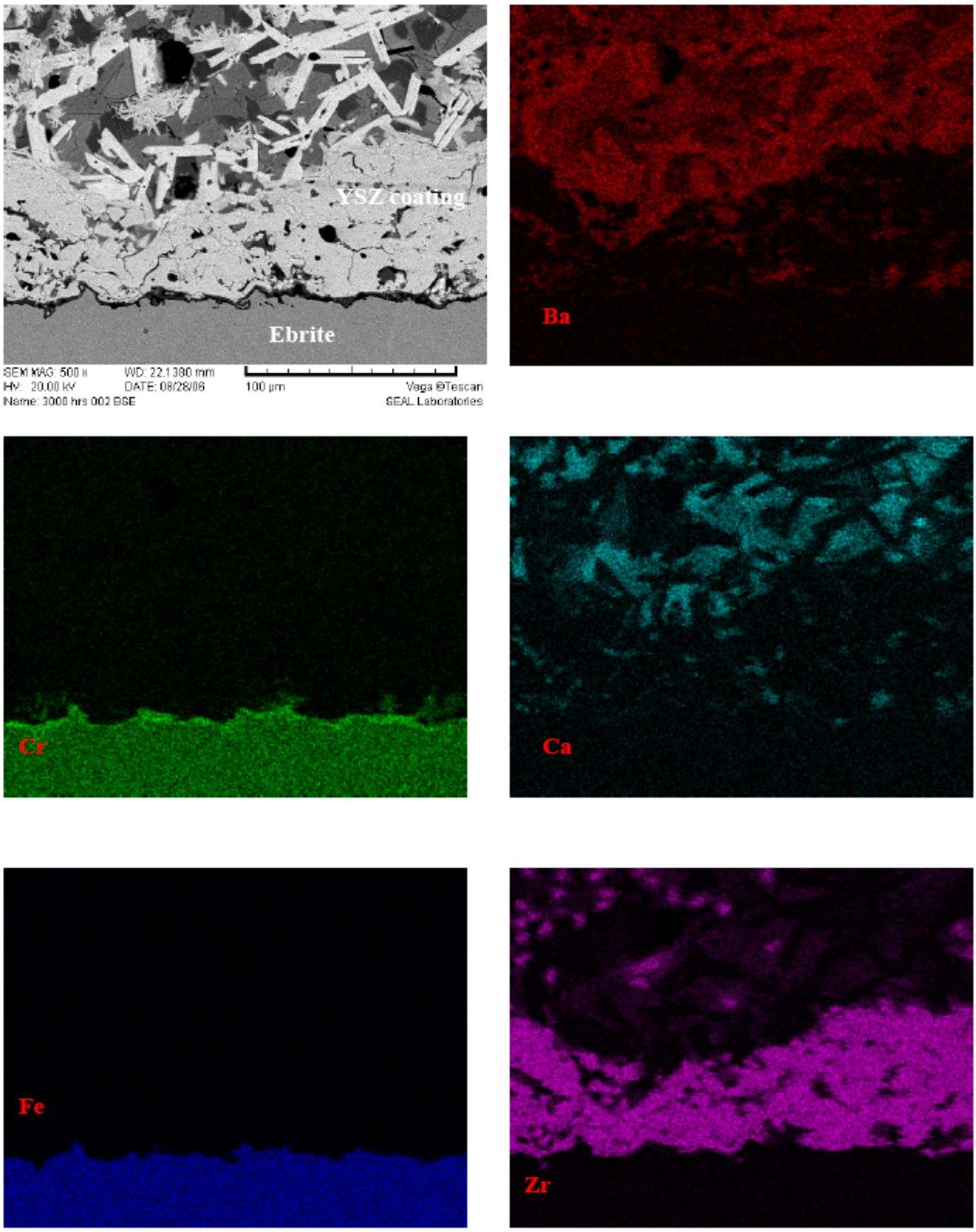

Figure 3.46 BSE image and element mapping results of glass-Ebrite interface after 3000 hrs at 800 °C in air

While the YSZ coating effectively suppressed Cr dissolution into the glass in the middle of the seal region where its continuity was maintained, $BaCrO_4$ was formed at the edge of seal where bare Ebrite is exposed to air as shown in Figure 3.47. The $BaCrO_4$ formation extended to 200 µm inside the sealing glass

from the edge of the seal. It was most likely formed via gas phase transport of Cr from Ebrite that is exposed to air. Local stresses generated due to CTE mismatch in this region may be deleterious therefore requiring a mitigation plan to prevent its occurrence.

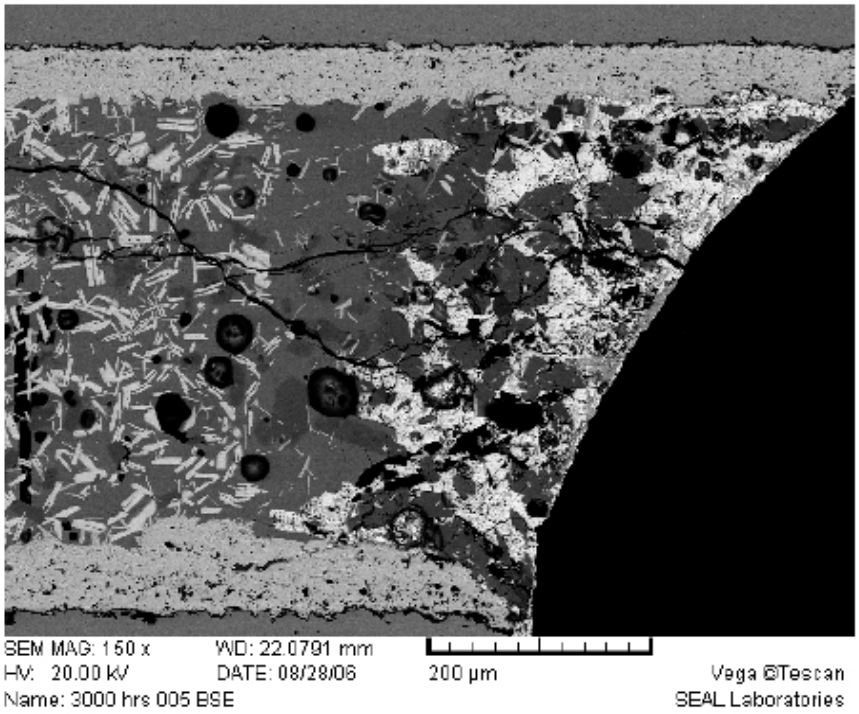

Figure 3.47 BSE image at the edge of seal after 3000 hrs at 800 °C in air. The white phase on the outside is $BaCrO_4$.

3.4.4 Manufacturing approach down selection

3.4.4.1 Introduction

GE Global Research explored two manufacturing processes for SOFC cell fabrication as part of the execution of this project. First, a sintered fabrication approach was pursued for an anode-supported cell with a calendaring approach. Second, atmospheric plasma spray was explored with a metal supported approach. GE conducted a process to down select one approach for the continuation of the program.

3.4.4.2 Manufacturing development towards down selection

Different requirements drive the selection of a manufacturing process: ability to reach technical goals, technical risks, and prediction of consistency of production. Ultimately these requirements roll up to a predicted cost for the stack. The approach used to drive technical activities was therefore to use the stack

cost model to identify how the cell manufacturing processes impact the overall cost. This analysis of current and predicted cost dictated technical activities.

The analysis of the cost model results, with an assumption review, led to the investigation of the following technical points:

Sintered manufacturing:

- Investigate capital cost assumption (number of steps, yields)
- Understand impact of manufacturing on cell performance
- Develop a cell sealing solution compatible with large stacks

APS manufacturing

- Demonstrate feasibility of hermetic electrolyte
- Demonstrate thermal stability of interconnect during APS
- Demonstrate stability of cells (degradation equivalent to sintered)

Some of the requirements to meet the overall cost requirement are actually independent of the manufacturing approach but have to be considered to assess SOFC technology viability as a whole:

- Power density path to requirement
- Degradation path to requirement
- Metal thickness reduction

3.4.4.3 Risk sensing session

A risk sensing session was performed to capture the perception of each technical team on the relative development risk of both manufacturing approaches. This session's goal was not to drive to a consensus among the team but more to clearly identify the divergence of opinions on technical elements. This information could then be used by the technical review team to probe further.

3.4.4.4 Technical team review

The technical team evaluated the two approaches by using a scorecard developed by the program principal investigator and the chief engineer of the project. The presentation material was organized accordingly to answer the key questions in the scorecard.

Presentations were made to the technical team. The general topics were:

1. Current ability to meet technical requirements
2. Projected ability to meet requirements
3. Manufacturability
4. Cost

3.4.4.5 Down selection results

Compilation of the results from the technical review team led to the following results based on the scorecard format:

What is your single greatest concern about the long-term viability of MW-scale SOFC technology?

Cost and degradation.

3.4.4.6 Conclusions and recommendations

These results were used as key input for the decision process. To supplement this information, different sources of information where also used such as:

- Competitive assessment
- Intellectual property assessment
- Technical development program risks and financial evaluation

This information complemented the technical evaluation of the development of SOFC technology to assess the chance of success of each development path. In light of all sources of information, the following conclusions were extracted:

- Both manufacturing approaches present significant risk of achieving a technical level compatible with business and commercial goals.
- In both cases, if the success of the technical program is assumed, no significant differentiation can be identified from a “should cost” perspective under a high volume assumption.
- The major risks related to SOFC technology development are not related to cell fabrication but rather in capability of the basic technology to meet degradation and performance metrics compatible with the cost model.

As a result, GE recommended a refocus of the SOFC technical development on material activities to address degradation challenge of high performance SOFC material sets.

3.5 Degradation mitigation

3.5.1 Degradation mitigation approach

LSCF-based mix-conducting perovskites have shown great potential as high performance cathode materials for intermediate temperature SOFCs [3,4]. Recently, GE reported ~1 W/cm^2 initial power density at 0.7 V and 800°C on 25 cm^2 sintered SOFCs with LSCF cathodes [5]. However, the area specific

resistance (ASR) degraded at a rate of ~110 mΩ-cm^2/1000 h as shown in Figure 3.48. This high degradation rate is not acceptable for SOFC commercial applications. For commercialization of SOFCs for multi-MW power generation, an order of magnitude reduction in degradation rate is necessary.

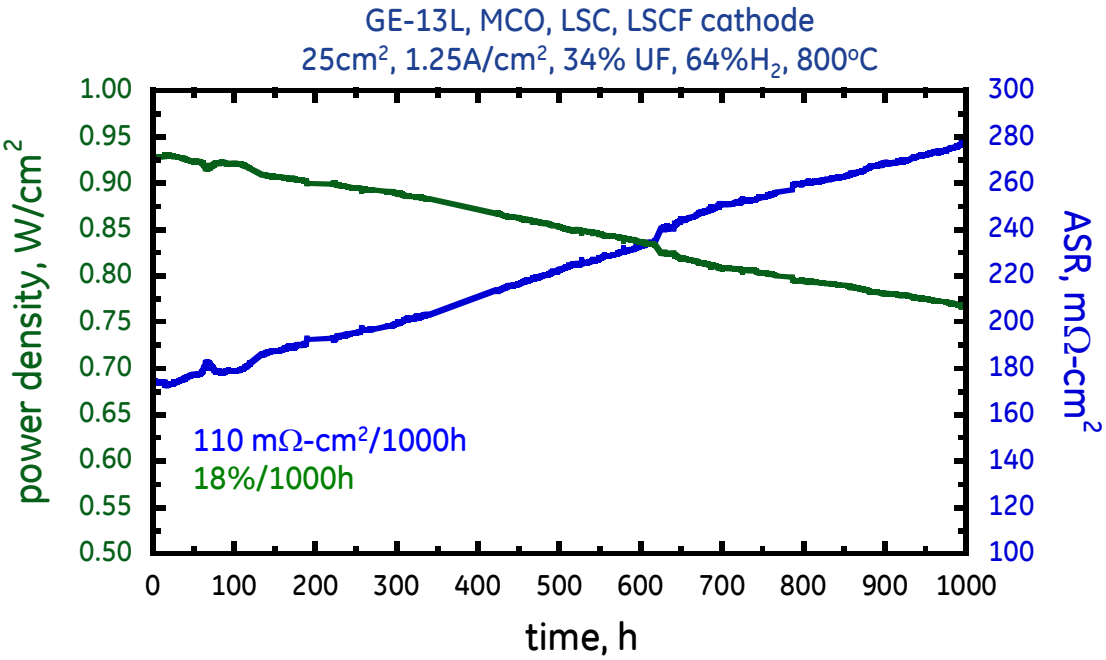

Figure 3.48 Performance degradation of LSCF cathode-based SOFC.

Several investigations have focused on identifying and understanding SOFC performance degradation [6,7,8]. Building on these studies, as well as significant research at GE, the performance degradation mechanisms are outlined, and their corresponding types of degradation are shown in Figure 3.49. Understanding the impact of potential degradation sources is complex and specific mechanisms are influenced by testing vehicle and configurations, material sets and testing conditions. Therefore, a self-consistent research program, utilizing single variable analysis, is essential to understanding and mitigating degradation in LSCF cathodes.

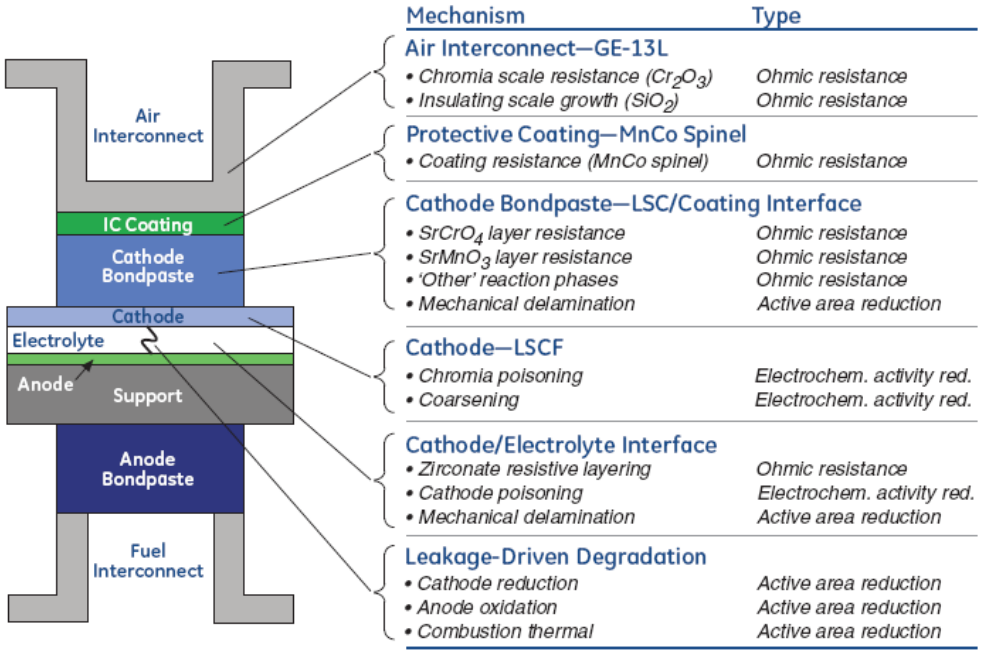

Figure 3.49 Schematic of an SOFC highlighting potential degradation mechanisms.

Based on prior experimental and modeling efforts, the dominant degradation sources have been determined to be cathode side related for SOFCs containing LSCF cathodes. Potential cathode degradation sources can be categorized as either structural or chemical related degradation mechanisms. Structural degradation mechanisms include the in-situ sintering and coarsening of layers, loss of intimate contact between adjacent layers, and cracking. Chemical degradation mechanisms include the formation of reaction layers, chemical poisoning of catalytic sites, and material phase instabilities.

In order to understand the dominant degradation mechanisms and propose cost-effective mitigation solutions, the project focus was limited to a fixed materials set. Limiting the number of variables in this investigation significantly increases the effectiveness of the program at identifying high-impact degradation mechanisms and corresponding mitigation solutions. Minor adjustments to stoichiometry are permitted, but the base system remains constant.

The fixed materials set, flowing from top to bottom in Figure 3.49, is as follows:

Ferritic stainless steel interconnect
Interconnect protective coating based on $(Mn,Co)_3O_4$ spinel
Lanthanum Strontium Cobalt (LSC) cathode bond paste
Lanthanum Strontium Cobalt Iron (LSCF) cathode
Ceria barrier layer
Yttrium stabilized Zirconia (YSZ) electrolyte
Nickel / YSZ active anode
Nickel anode support

The available variables for modification are related to the minor chemistry / stoichiometry, processing conditions and testing conditions.

3.5.2 Degradation rate reporting

In order to identify degradation mechanisms, develop mitigation strategies and predict 40,000 h lifetimes; a solid understanding of the degradation rate is required. Typically, degradation rates are measured and reported as a loss of voltage or power density while driving a cell at a constant current density. This approach may be an appropriate representation of the actual implementation of an SOFC. However, such an approach is not sufficient for developing a detailed understanding of degradation mechanisms leading to predictions of long-term cell life.

3.5.2.1 Degradation rate reporting at constant current Vs voltage

Degradation rate reporting at constant current (galvanostatic) and constant voltage (potentiostatic) conditions result in dramatically different measured power density degradation rates as shown in Figure 3.50. This figure shows a hypothetical high-performance SOFC operating at 800^{o}C with the ASR and power density plotted as a function of time. Starting performance is 1 W/cm^2 at 1.25 A/cm^2 and 0.8V with a corresponding ASR of 128 mΩ-cm^2.

Power densities taken at the corresponding operating conditions (1.25 A/cm^2 – purple and 0.8V – blue) yield very different degradation rates assuming a linear ASR degradation rate of 25 mΩ-cm^2/1000h. A logical conclusion would be that the degradation is very different for the two operating conditions, however, the ASR change for the two conditions is identical. In other words, the fundamental degradation mechanism is the same and the reported power density degradation rates are an artifact of the method for reporting degradation rate.

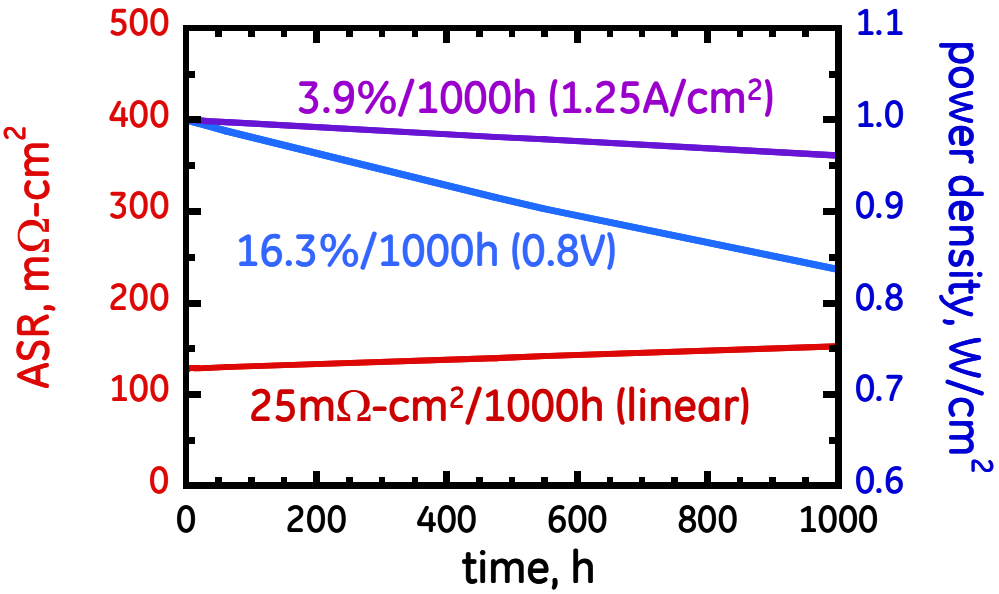

Figure 3.50 Hypothetical ASR and power density plotted as a function of time. Starting performance is 1 W/cm^2 at 1.25 A/cm^2 and 0.8V with a corresponding ASR of 128 mΩ-cm^2. Power densities taken at the corresponding operating conditions (1.25 A/cm^2 – purple and 0.8V – blue) yield very different degradation rates assuming a linear ASR degradation rate of 25 mΩ-cm^2/1000h.

The relationship between the ASR and the operating conditions are shown in Equation 3.1.

Equation 3.1

$$\mathrm{PD}_{\mathrm{V=const}} = \frac{V_{op}\left(OCV - V_{op}\right)}{ASR}$$

$$\mathrm{PD}_{\mathrm{J=const}} = \left(OCV - ASR * j\right)j$$

Where V_{op} is the operating voltage, OCV is the open circuit voltage at representative humidification levels and j is the operating current density.

The source of this mathematical artifact is further illustrated in Figure 3.51. The linear region of the start of test power curve is shown in red, with a slope giving an ASR of 128 mΩ-cm^2. The blue curve shows an ASR of 153 mΩ-cm^2, after 1000h of testing, assuming a 25 mΩ-cm^2 linear degradation rate. The corresponding degradation rates for each operating condition are also shown on the plot.

At very low current densities, the reported degradation rate would be very low, as the change in voltage is only a small percentage of the corresponding operating voltage. However, at high current densities, the degradation rate would appear to be much greater as the change in voltage is a much greater percentage of the corresponding operating voltage. In the constant voltage frame of reference, the change in current density is always the same percentage of the corresponding

operating voltage. Regardless, the actual ASR and change in ASR is the metric that ties the two conditions together and can most easily be quantified and used to measure and study degradation.

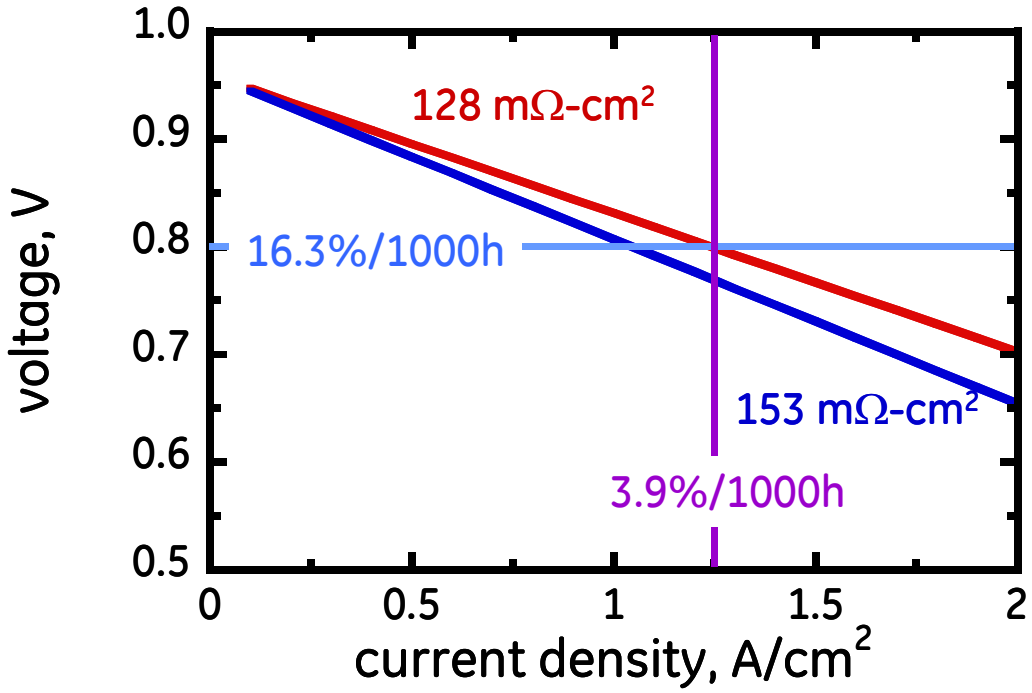

Figure 3.51 Voltage-current, power curves for the hypothetical cell shown above at the start of test (red) and after 1000h (blue) showing a net slope change leading to 25 mΩ-cm^2 ΔASR.

This point is made clearer by noting the equations used to describe the corresponding degradation rates for the two conditions in Equation 3.2. The degradation rate at constant voltage is strictly a function of the ASR, and the corresponding degradation rate at constant current density is a function of the ASR and the operating current density. Therefore, the constant current degradation rate is confounded by the operating conditions.

Equation 3.2

$$DegradationRate_{V=const} = \left(1 - \frac{ASR_0}{ASR_1}\right)$$

$$DegradationRate_{J=const} = \left(\frac{J\left(ASR_1 - ASR_0\right)}{OCV - J \times ASR_0}\right)$$

Thus, in order to quantify and understand degradation rates, the area specific resistance (ASR), is the most useful metric.

3.5.3 Development of experimental and processing capabilities

Performance degradation of SOFC systems due to chemical and electrochemical interactions on the cathode side of the cell in contact with chromia-forming ferritic steel interconnects have been the focus of many recent studies [for example: 9,10]. The transportation of volatile Cr- species into the SOFC cathodes through vapor-phase processes and its deleterious interaction with the SOFC cathode materials, also known as chromia poisoning, have been recognized widely as one of the main challenges of long-term and reliable application of these systems [11]. Moderate performance improvements have been reported in various SOFC systems using specially designed interconnect alloys that limit the volatility of their chromia scale. In addition overlay protective coatings of conductive perovskite and spinel oxides have been developed and successfully demonstrated on metallic interconnects on the cathode side of SOFCs [12,13]. Some of these coatings have been shown to effectively reduce the volatilization of the chromia scale to negligible values. Despite these improvements and a body of literature studying the performance of SOFCs with metallic interconnects, little is known and/or agreed upon on the exact nature of degradation processes operative in SOFC cathodes in contact with chromia-forming interconnect alloys. One particular point of contention appears to be the contribution of ohmic and non-ohmic (polarization, chemical interactions, and etc.) processes to the degradation of SOFC cathodes in contact with the interconnect material.

Thus, both electrochemical and non-electrochemical approaches are adopted to characterize SOFC degradation. The former enables identifying the mechanisms leading to performance degradation of LSCF cathode-based SOFCs under realistic operating conditions, and the latter offers simplified and clean measurements that aid in quantification of the contribution from specific isolated degradation mechanisms. Combined, the information gathered from both approaches enables the determination of an ASR breakdown, a key tool for understanding the total ASR as a sum of individual ohmic and polarization contributions associated with specific mechanisms.

3.5.3.1 Contact resistance measurement / off-line ASR test

In an attempt to gain insight into the contributions of various ohmic (e.g., growth of the oxide scale and interaction/reaction layers at the interface between the metal interconnect and the SOFC cathode) and non-ohmic (destruction of active sites for oxygen reduction within the cathode due to reaction with Cr-vapor) mechanisms to the degradation of cathode, emphasis is given to a combination of SOFC button cell testing and off-line ASR experiments using test specimens that simulate the configuration of the cathode side of the same button cells. Such off-line tests have been used recently in the literature to evaluate the interfacial ASR and the effectiveness of over-lay coatings applied to metallic interconnects for application on the cathode side of SOFC cells [12]. It is envisioned that a quantitative comparison of the results from the two sets of experiments in conjunction with the existing models would furnish understanding of the

degradation processes that contribute to the ASR increase of the SOFC cathodes.

A contact resistance test was designed to measure ohmic ASR as a function of time. The ohmic contribution of the metal interconnect (including potential oxide formation), MCO coating, cathode bond-paste, cathode, and their interactions, can be analyzed using an off-line testing configuration. The sandwiched test specimen can replicate all or part of the SOFC cathode side, and be tested under electrical loads at temperatures representative of the electrochemical experiments. A comparison of the ohmic ASRs determined from the off-line tests with the ohmic ASR from SOFC button cell tests will provide insight into the ohmic and polarization contributions to the degradation of SOFCs.

Objectives

- Study the increase of ohmic ASR as a function of time due to metal interconnect, cathode bond-paste and resulting interactions using a simulated off-line test configuration.

- Compare the stack-up of ohmic ASR from the off-line tests with those of the ohmic ASR from SOFC button cell tests under the same test conditions to gain insight into the contributions of ohmic and non-ohmic processes to the degradation of SOFC systems.

-Compare and rank various bond-paste and over-lay coating compositions for application onto GE-13 and E-Brite alloys in contact with LSCF cathodes using the test results.

Setup

The test specimen configuration selected for this purpose is shown in Figure 3.52. It is similar to the specimen geometry used by PNNL [12] in their studies of protective spinel coatings on steel interconnect. The sandwiched test specimen structure replicates part of or the entire cathode side of the SOFC cell. The testing under electrical loads (constant current or constant voltage) at elevated temperatures resembles those of the electrochemical experiments involving button cells.

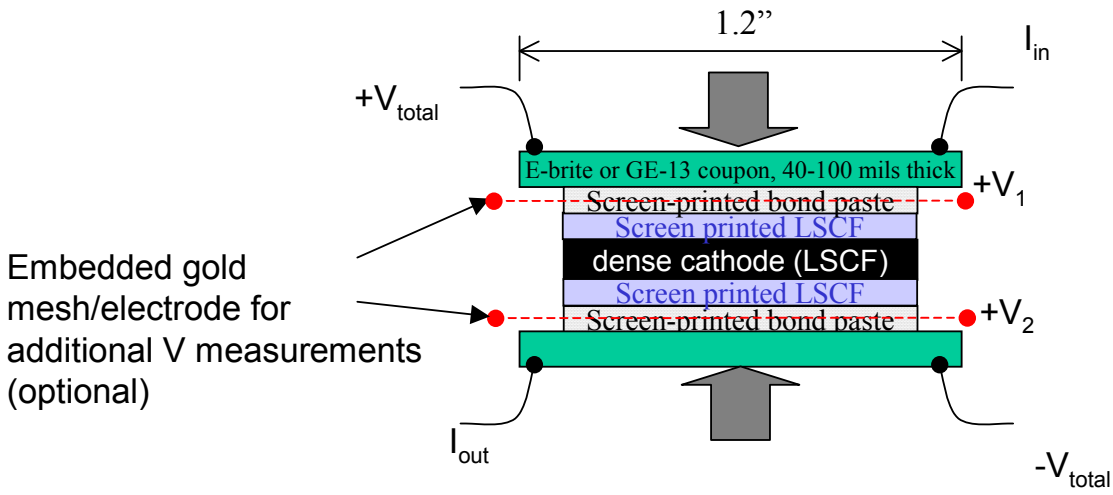

Figure 3.52 Schematic of test specimen configuration for off-line ASR testing. The metallic coupons are 1.2” x 1.2”. The cross-section of the test area is approximately 1.0” x 1.0”.

Test specimens are fabricated by applying the ceramic layers onto metallic coupons of GE-13 and E-Brite alloys using screen-printing process. The test specimens are installed on a multi-racked fixture capable of holding up to 2 specimens on each level within the hot-zone of a vertical furnace. The test setup is shown in Figure 3.53.

a) b)

Figure 3.53 Test setup for off-line ASR testing. a) Test stand that can accommodate 6 samples (2 per level). b) A single level showing thermocouples and electrical connections.

Proper electrical contacts are made using short lead wires (Pt or thermocouple grade type-K lead wires) spot-welded onto either sides of the specimens for independent four-point resistance measurements. Additional voltage-

measurement electrodes (gold mesh) are being considered for intermediate placement within the sandwiched structure as shown in Figure 3.52. This would facilitate additional local ASR measurements that could help with the partitioning of the contributions of the interfaces located between the two measurement points, e.g., metal/bond-paste interface and/or cathode-bond-paste/cathode interface, and etc. However, it is noted that for the typical thicknesses (20μm-50μm) of the ceramic layers within the structure shown the placement and isolation from electrical shorts of the intermediate electrodes are somewhat challenging.

In addition to the direct measurement of the resistances of the samples and their evolutions with time, impedance spectroscopic measurements are also being used to estimate the ohmic ASR behavior of these samples at discrete time intervals. The spectroscopic measurements are used in an attempt to establish confidence in ohmic ASR measurements using this method as well as to observe whether formation of interfacial reaction layers (ie, $SrCrO_4$ at the interface between the chromia scale and the LSC bond-paste) could potentially contribute to any capacitive effects which could give rise to a polarization loop in the impedance spectrum. It is to be noted that the impedance spectra collected to date on these samples do not show any polarization loops. The data is indicative of good agreement between the ASR values measured for the same sample using the two different techniques. Post-test examinations are conducted on all the test specimens to compare their microstructures.

3.5.3.2 Wet hydrogen contact resistance measurement

Experimental results have indicated a possible degradation contribution from the anode current collector. The specific mechanisms, however, are not yet fully understood. Thus, a test to isolate these mechanisms to allow systematic study is desired. Building on the success of the contact measurement tests, an apparatus for doing the same measurements in a wet hydrogen environment was constructed. This test simulates typical SOFC anode conditions, allowing isolation of the porous nickel to anode current collector interactions that would be attributed to the source of degradation.

Test Stand Description

The test stand consists of 4 main components:

1) Sample holder
2) Alumina containment tube
3) High temperature furnace, and
4) Steam injection humidifier
5) Sample holder

Sample Holder

The sample holder consists of a ceramic platform to support the samples, current and voltage measurement wires, gas input plumbing and a high temperature seal to contain the humid hydrogen environment. These components are shown in Figure 3.54.

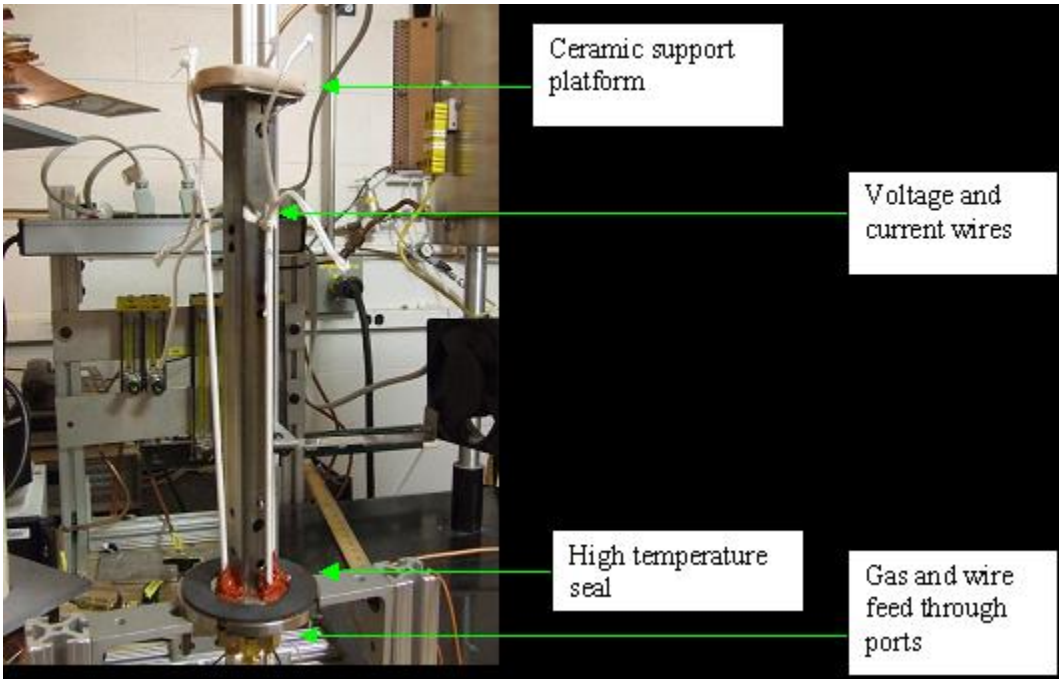

Figure 3.54 Sample holder for wet hydrogen contact resistance testing.

Alumina Containment Tube

The alumina containment tube will preserve the wet hydrogen environment inside the furnace. Cooling devices at either end help maintain the integrity of the seals during operation. The tube will also provide extra stability for the sample holder and provide a safe path to vent the hydrogen. The alumina containment tube is shown in Figure 3.55.

Figure 3.55 Alumina support tube for wet hydrogen contact resistance testing.

High Temperature Furnace

The furnace is a vertical three zone clam-shell design capable of heating to 1200ºC (Figure 3.56). It is suspended off the bench to allow the samples, while on the sample holder to be centered in the hot zone.

Figure 3.56 High temperature furnace for wet hydrogen contact resistance testing.

Humidifier

The humidifier, shown in Figure 3.4, is a steam injection unit capable of providing up to saturated levels of humidification at the desired hydrogen flow rate of 5 liters per minute. It has a heated gas line that will travel to the test stand to prevent condensation in the line.

Figure 3.57 Steam injection humidifier for wet hydrogen contact resistance testing.

It is important to study the materials in question in an environment that is as close as possible to the one that they experience during typical SOFC operation. This test will provide us with the ability to understand the nickel to anode current collector interactions and how they evolve at temperature over time.

Sample fabrication and testing conditions

Two configurations were tested for ohmic ASR degradation to determine if geometry effects were present. First, a sandwiched GE13L-Ni-GE13L sample was made using 1" GE13L polished squares, and ohmic ASR was measured. Sample fabrication, testing details, and results were included in previous reports.

The second sample configuration was a 1" GE13L polished plate-Ni-Ni mesh square. A schematic of the configuration is shown in Figure 3.58. First, approximately 0.06 g/cm^2 (wet weight) of NiO anode bonding paste was applied in multiple coatings on the GE13L substrate, and dried. The mesh was then embedded into additional NiO anode bonding paste (approximately 0.04 g/cm^2). The total amount of NiO was slightly less than used on a typical SOFC 1" button test. After complete drying, the sample was loaded onto the ceramic support platform in the test rig, and the voltage and current wires were spot welded to the GE13L and Ni mesh enabling 4-point resistance measurements.

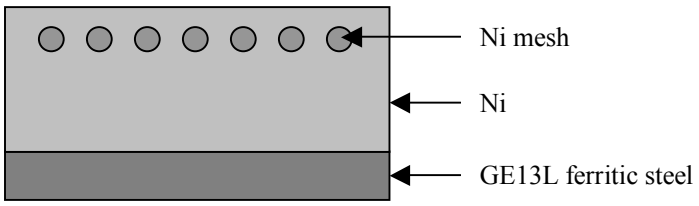

Figure 3.58 A schematic of the GE13L – Ni – Ni mesh sample.

Once the alumina tube was sealed, the sample was heated to 800^{o}C, at which point dry H_2 was introduced at approximately 3.5 L/min to reduce the NiO bond layer. After reduction, the humidifier was set so that the total flow was nominally 50% H_2O (to mimic a reasonably high operating SOFC fuel utilization), and the current was set to 3.2 A (0.5 A/cm^2). Voltage was monitored to determine the sample ASR.

3.5.3.3 Button cell testing

A number of modifications have been carried out on 1" SOFC button cell testing (6-gun) rigs. These modifications have been necessary to improve the quality of the data and to extend the length of test time. These modifications include: increasing the capacity of the humidifiers from 2 to 15 liters, heating the humidified fuel lines from the humidifier to the cells and using to ceramic weights and quartz air tubes to remove potential degradation accelerants. These were carried out to improve the quality of the ac impedance data, to further reduce electrical noise on the test data and to reduce the chances of premature reduction due to residual hydrogen in the gas system.

Fuel system and humidification

This program has historically used humidifiers designed to carry enough water for 300 hours. This clearly is not enough for degradation testing where the baseline will become 500 hours with the option to run several thousand. Thus, the 2-liter humidifiers have been replaced with 15-liter units that should permit testing to ~2000 hours at a 3 mol percent steam level. Additionally, a bypass system has been designed and implemented, enabling the ability to run dry fuel if desired. This is primarily useful for diagnosis reasons when water is suspected to be accumulating in the system. As water condensation is a potential problem, heated fuel lines have been added between the humidifier and the test rig.

The fuel system was modified to incorporate heating all the way from the humidifier. These improvements included insulating the separate gas feed lines to the individual cells and monitoring the temperature to be maintained above that of the humidifier. The exhaust has been made more direct and exhausts further into the hot-zone of the furnace. These modifications are aimed at preventing water condensation problems.

A fuel/air manifold has been developed along with some test procedure changes to improve the quality of the tests. The manifold is a rigid plate attached to the furnace stand with gas bulkhead fittings allowing gas lines to be attached at either side. This enables the test stand to be held firm while gas lines are attached and detached at the other side manifold without translating any of the movement onto the test stand. This modification allows simpler implementation of a procedural change to provide flowing air to both the cathode and anode side of the fuel cells on heat up. Thus eliminating the chance of premature anode reduction and ensuring all organics are safely carried away during burnout.

Ceramic weights and quartz air tubes

Button cells require a mechanical load to minimize contact resistance and maximize repeatability. Traditionally, stainless steel weights have been used. However, the chromium from the steel at high temperature is a potentially uncontrolled degradation mechanism. Thus, transitioning to ceramic weights should minimize this issue. Another potential source of chromium is in the air delivery system, which is again constructed from a stainless steel. To address this issue, the program is transitioning the air system to quartz tubes (Figure 3.59).

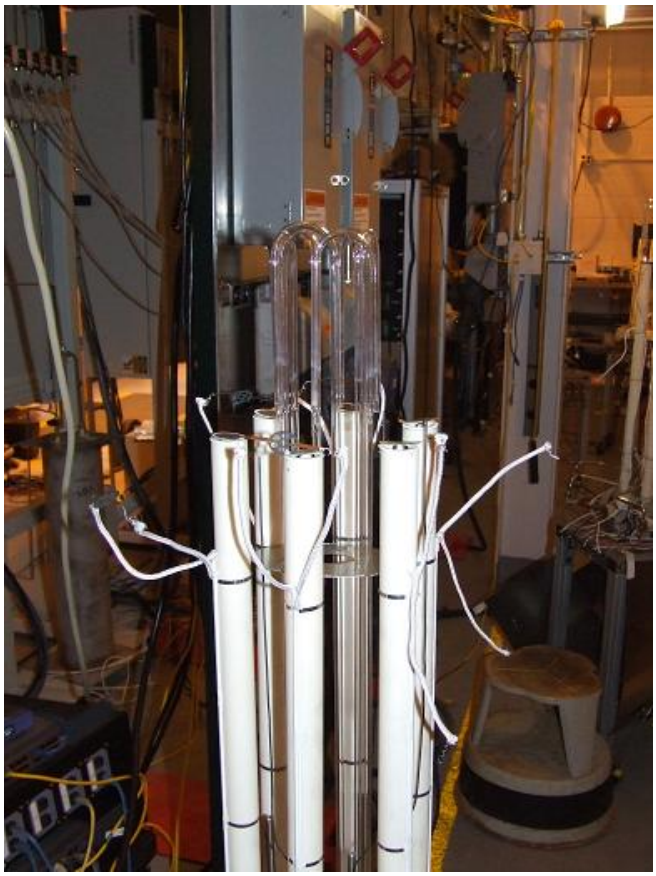

Figure 3.59 Quartz air delivery tubes

Wiring

Previously, the platinum wires from the cell only ran to the edge of the furnace hot zone and were extended to a connection panel via copper wires. Though economical, this was shown to create high frequency artifacts in the AC impedance scan. Therefore, the platinum wires were extended directly to the connection panel eliminating the copper wires (Figure 3.60). Additionally, the impedance instrument test wires were replaced, from a single 4 conductor shielded cable, with 4 independently shielded cables. This was done to further isolate the wires from crosstalk and the improved impedance curves can be seen in Figure 3.61.

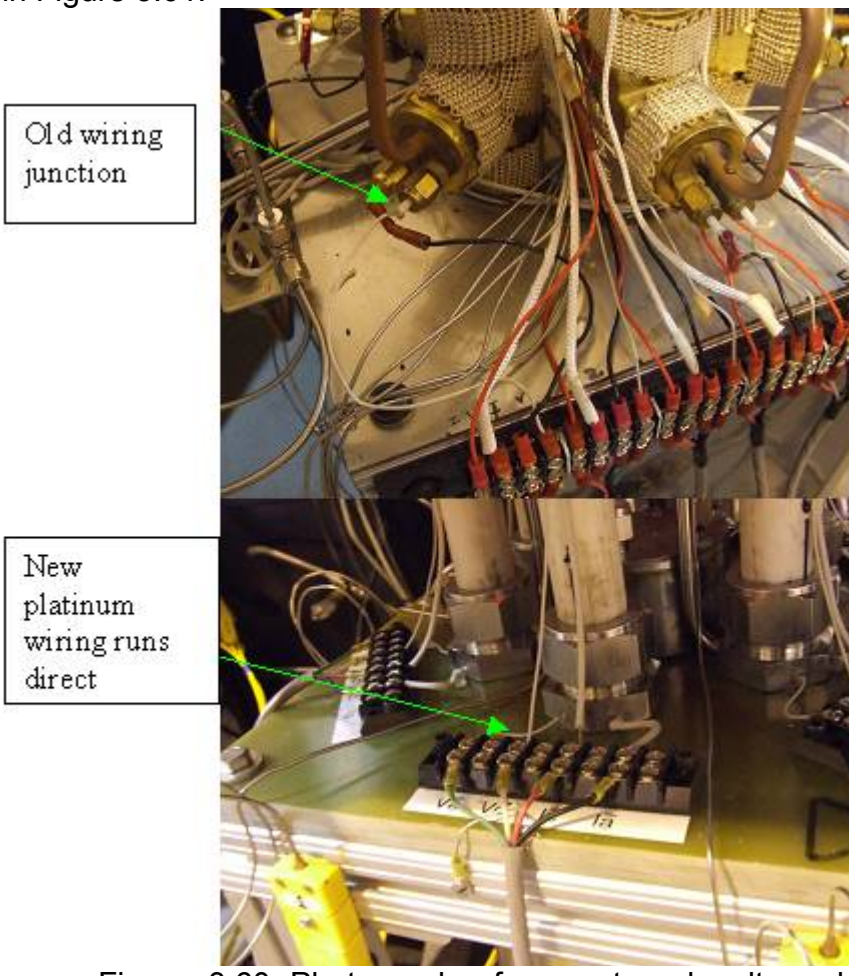

Figure 3.60 Photograph of current and voltage lead wiring for button cell testing.

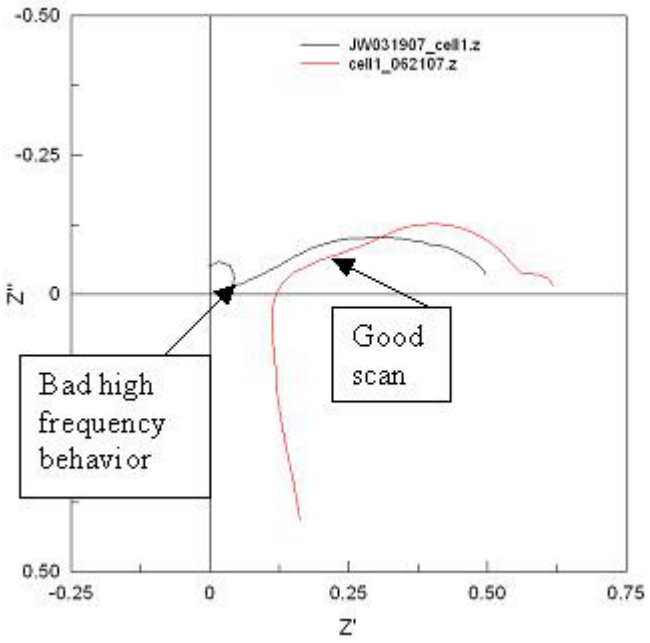

Figure 3.61 Improved AC impedance curves with wiring improvements.

3.5.3.4 25 cm^2 ceramic test vehicle

In order to accurately measure SOFC performance under realistic conditions, an all-ceramic (99.9% alumina) test vehicle was developed. This test vehicle is named the Browaller in honor of Ken Browall who recently retired from GE Global Research. Such a test vehicle provides known boundary conditions during cell operation. Therefore, accurate measurement of the degradation impact of single variable testing can be performed. Additionally, the data from this test vehicle can be used to determine the ASR stack-up.

The ceramic test vehicle (CTV) is pictured in Figure 3.62. The CTV is designed as a reusable test vehicle for testing sintered solid oxide fuel cells (SOFC) at temperatures around 800°C. It consists of four major parts: an Anode Alumina Support (AAS), a Cathode Alumina Support (CAS), an Anode Flow Field (AFF), and a Cathode Flow Field (CFF). All parts are made from 99.99% alumina.

Experimental setup

The actual Browaller setup in the furnace is shown in Figure 3.62. Fuel and air are supplied via ceramic tubes sealed to the Anode Alumina Support (AAS) and Cathode Alumina Support (CAS), respectively. The cell, sandwiched between the CAS and AAS, is glass sealed.

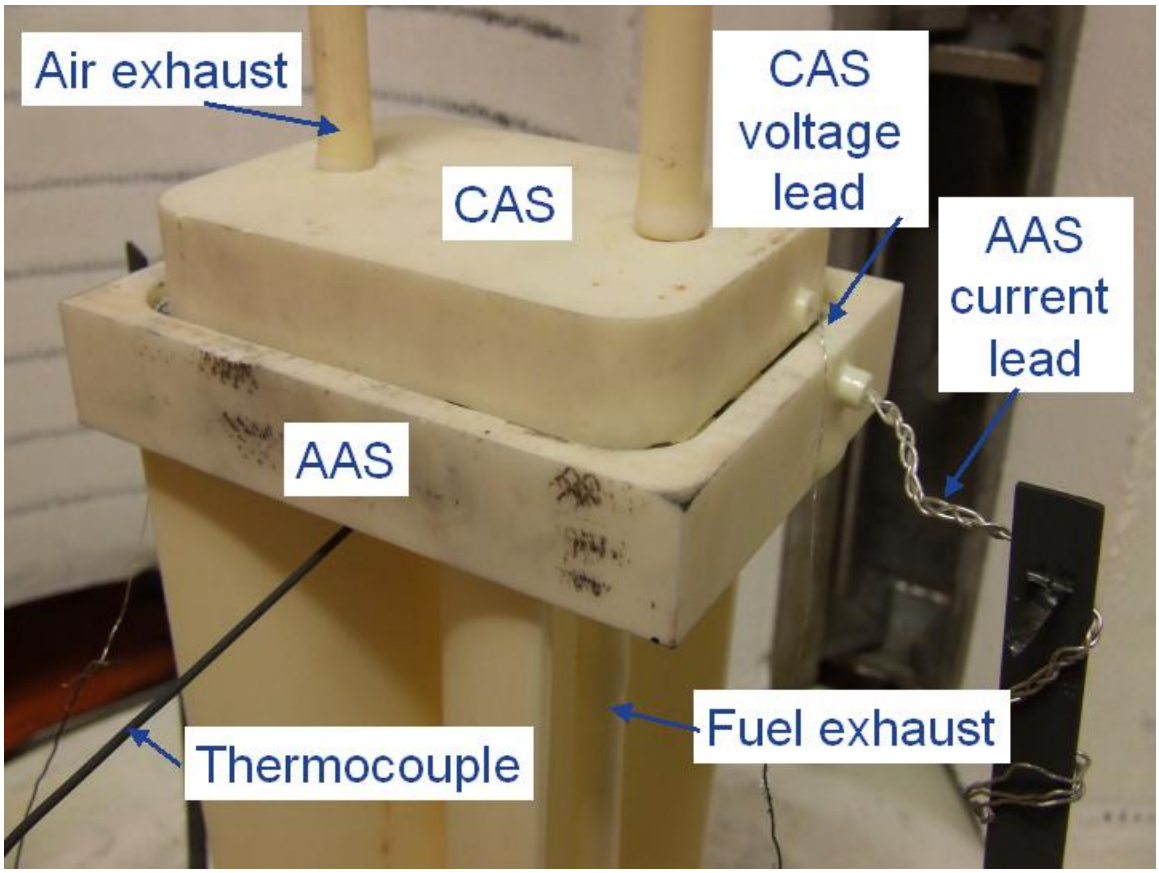

Figure 3.62 Browaller ceramic test vehicle in furnace after test.

Browaller work expanded the laboratory's testing capability by building and troubleshooting a new test stand. The new capacity allows for the testing of a total of three Browaller cells simultaneously.

Five cells were tested in early 2008. Statistical performance data for the five cells are shown in Table 3.10. All cells were traditional anode supported cells with in-situ, 2-phase, LSCF/GDC cathodes.

Table 3.10: Mean and standard deviation for Browaller cells 11 – 15.

	OCV (V)	Initial PD @ 0.7V (W/cm^2)	Initial ASR (Ω-cm^2)
Mean	1.06	1.07	174.0
Standard Deviation	0.01	0.01	7.0

The corresponding start of test power curves are shown in Figure 3.63. The high degree of repeatability is verification that the 25 cm^2 test vehicle is a robust vehicle for studying performance and degradation of representative-area SOFCs under representative conditions.

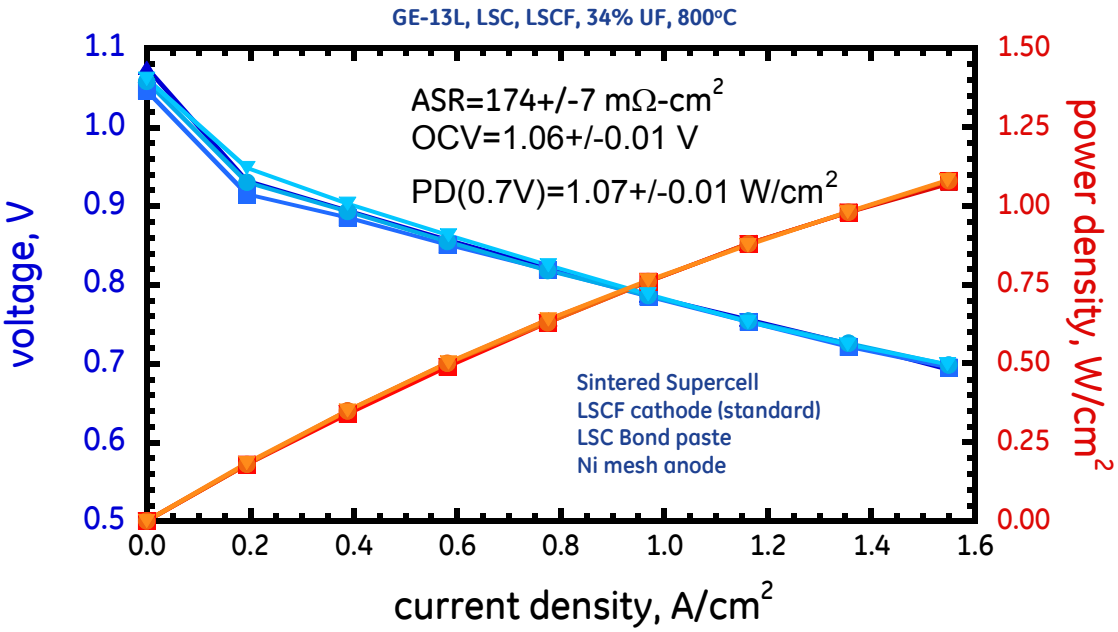

Figure 3.63 Power curves from five identical 25cm^2 cells showing good repeatability for the test rig.

3.5.4 Inherent stability of materials set

In order to elucidate specific degradation mechanisms, the inherent electrochemical stability of the materials set must be known. Given the complexity of an operating SOFC, understanding the stability of specific layers and interfaces can be, at the very least, elusive. Therefore, combinations of contact resistance measurement and button cell testing were used to understand this stability.

Gold is considered to be the preferred material for idealized current collection as it has been shown to remain inert during testing and does not influence the electrical or catalytic performance of SOFCs operating at 800°C. Historically, platinum was used and has been found to influence both the electrical and catalytic performance of SOFCs. Therefore, evaluation of the inherent stability of the materials set typically employed gold as the current collector.

3.5.4.1 Contact resistance with gold current collector

Figure 3.64 shows the evolution of ASR as a function of time for contact resistance coupons using gold current collectors in contact with LSC bond paste (red line), LSCF cathode (blue line) and a stack-up of both LSC and LSCF (green line). All were tested at 800°C and driven with 0.5 A/cm^2. As can be seen in Figure 3.64, there is no measurable ohmic degradation of the stack-up of LSC

and LSCF when in contact with gold interconnects. The conclusion to be drawn is that the stability of the LSC bond paste and LSCF cathode is excellent.

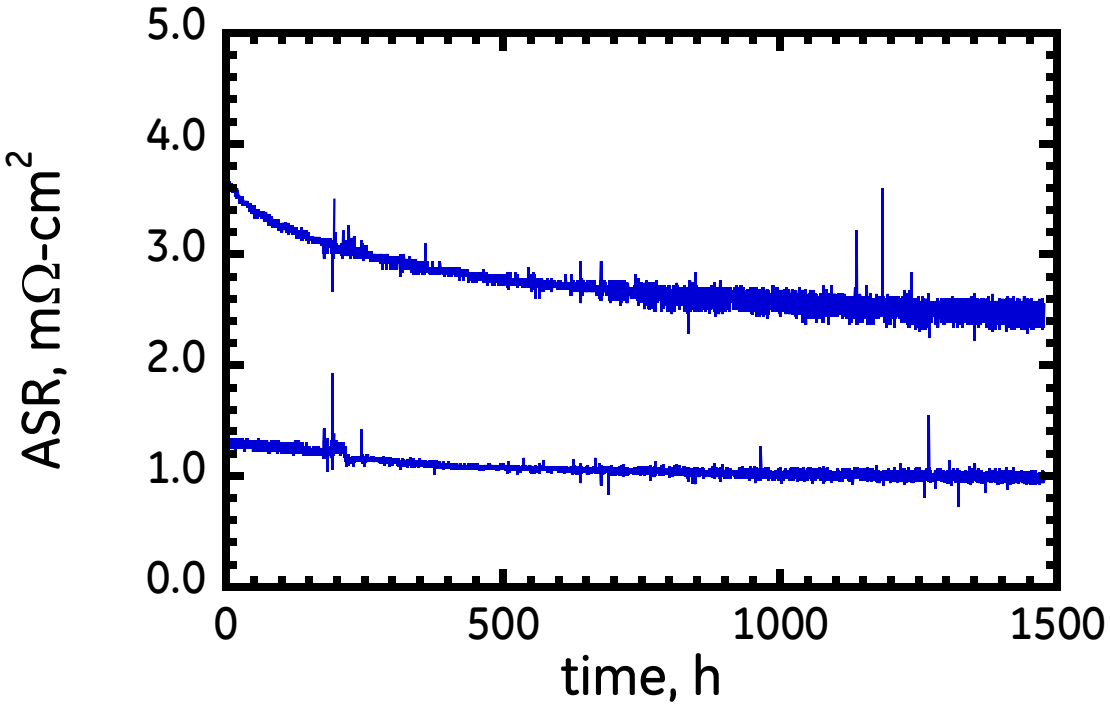

Figure 3.64. ASR evolution with time for stack-up of LSC and LSCF. All were tested on gold interconnects with 1 psi load and 0.5 A/cm^2 at 800^{o}C.

3.5.4.2 Electrochemical stability during button cell testing (gold mesh)

Given the exceptional ohmic stability of the cathode and bond paste shown above. The next logical evaluation is the electrochemical stability of the system operating as a fuel cell. The performance data is shown in Figure 3.65 for a pair of button cells with gold mesh cathode current collectors, nickel anode current collectors for the LSCF and LSC system shown above. These tests were performed at 800^{o}C under an applied load of 1.25A/cm^2. The data plotted is collected during periodic power curves at 0.7V.

The power density of this system is excellent, with both cells performing between 2.25 and 2.50 W/cm^2 at 0.7V and ASRs between 115 and 125 mΩ-cm^2. The change in performance is indicated in the figure and is essentially 'flat' indicating no performance loss over the duration of the 1000hr test.

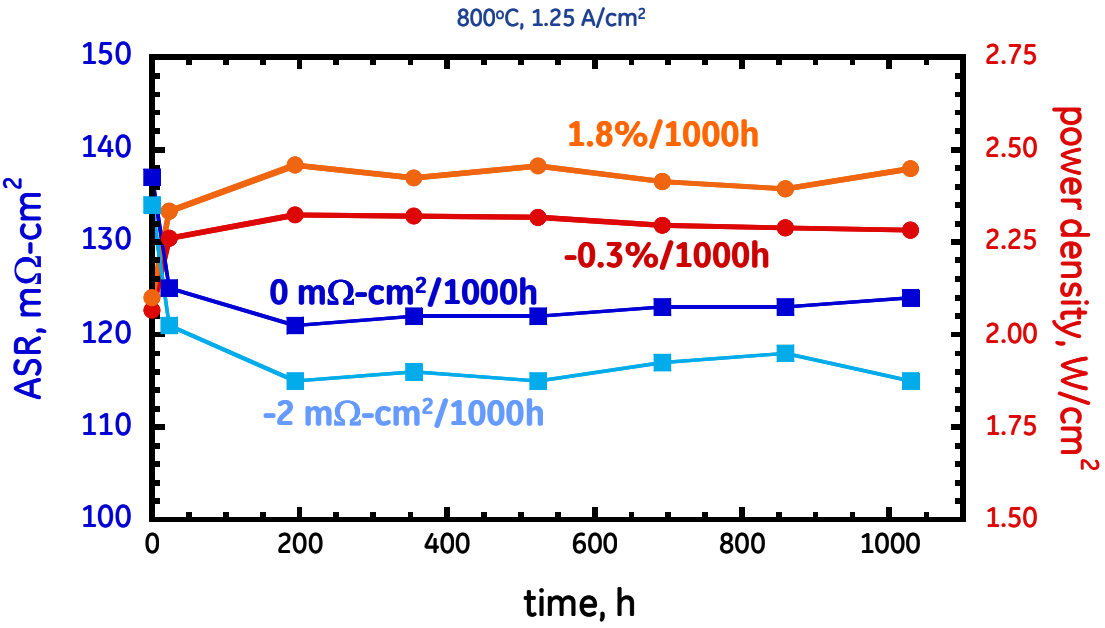

Figure 3.65 ASR and power density as a function of time for a button cell test at 800°C and 1.25A/cm^2 with gold mesh cathode current collector and nickel anode current collector. Performance data taken during power curves at 0.7V.

Therefore, the high-impact degradation mechanisms are generally associated with the implementation of ferritic stainless steel cathode interconnects. These interconnects introduce chemical species that can be detrimental to cell performance as well as a change in the mechanical boundary conditions supplied by the inherent constraints imparted by their specific geometries.

3.5.4.3 Contact resistance with ferritic stainless steel (GE-13L)

Given the exceptional ohmic and polarization stability of the cathode and bond paste shown in the sections above, the next logical step is to evaluate the ohmic stability of these systems using a representative ferritic stainless steel interconnect, GE-13L. It is well known that the thermally grown oxide, chromia, on ferritic stainless steel, interacts with strontium containing perovskites to form an electrically insulating phase, strontium chromate. The commonly accepted interconnect barrier coating to prevent this interaction, as well as the volatilization of chromium, is the $(Mn,Co)_3O_4$ spinel coating.

Thus, Figure 3.66 shows the evolution of ASR as a function of time for bare and $(Mn,Co)_3O_4$ coated GE13L in contact with LSC bond paste. The coated GE-13L with LSC indicates some degree of degradation, in comparision to the gold baseline, however these values are only ~4 mΩ-cm^2/1000h.

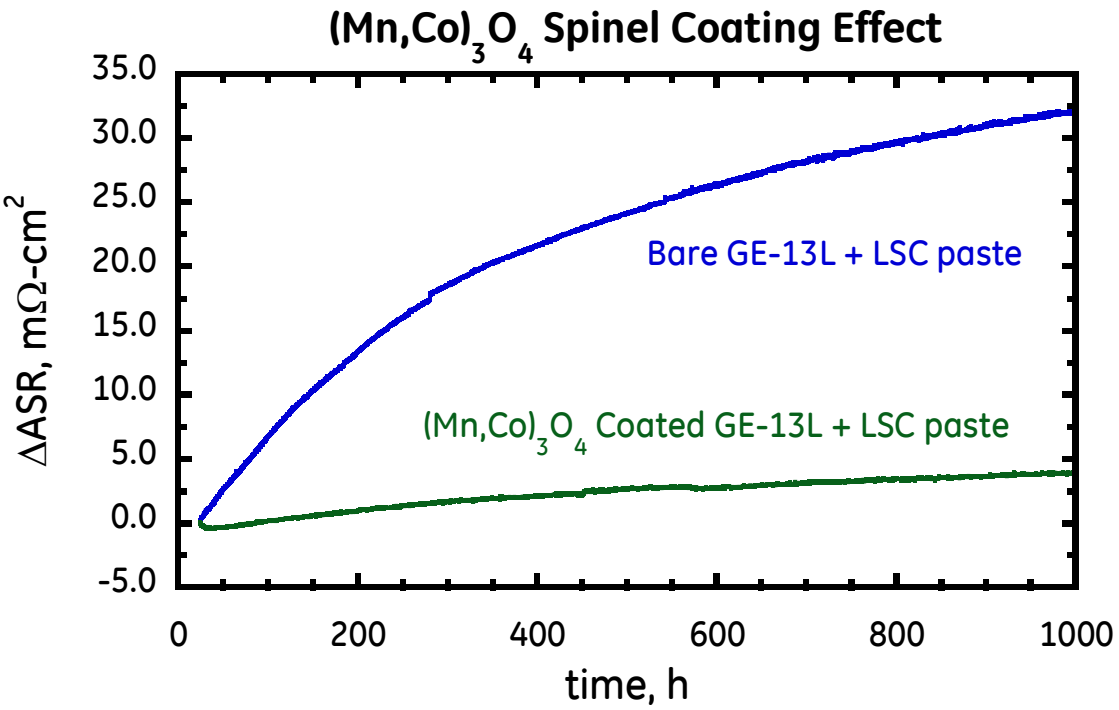

Figure 3.66. ASR evolution with time for bare and $(Mn,Co)_3O_4$ coated GE13L with LSC bond paste at 800°C, 0.5 A/cm^2 and 1 psi load.

It is not anticipated that an ohmic contribution of ~4 mΩ-cm^2/1000h would significantly impact the degradation behavior of SOFCs and is deemed to be acceptable. Additionally, given the parabolic nature of this degradation, the presumed mechanism is the thermally grown chromia layer on the ferritic stainless steel interconnect and is accepted as a generally unavoidable and acceptable contribution to degradation.

3.5.4.4 Anode contact resistance with ferritic stainless steel (GE-13L)

Though the project was defined to specifically identify and resolve cathode-side degradation mechanisms, understanding potential degradation contributions from the anode is important.

Two anode contact resistance measurement tests were performed with different geometries to represent an actual SOFC anode in service. In one configuration, two sheets of ferritic stainless steel were contacted by a NiO paste. In the other configuration, one of the sheets was replaced by a nickel mesh. The concern with the complete sheet configuration was that the system was not optimized for oxygen gas diffusion and full reduction of the NiO paste may not be achievable. In addition, the Ni mesh current collector was chosen to determine if a difference in compliancy contributed to mechanical degradation, such as loss of contact surface caused by delamination. There are three potential mechanisms for

delamination to occur: the difference in thermal expansion between nickel and GE13L (a ferritic stainless steel) during heat up; the large volume change associated with the reduction of NiO to Ni (~41%); and the sintering shrinkage of the Ni layer at operating temperature.

The collected ASR data, normalized to account for both GE13L surface interfaces, is shown in Figure 3.67 for both configurations. The first few hundred hours of the GE13L-Ni-GE13L test, water management and testing issues prevented the collection of meaningful data. At around 350 hrs, the voltage signal stabilized, then steadily increased throughout the test until it was stopped at around 800 hrs. For the 500 hrs of testing, the ASR (for total contact area of Ni with GE13L) increase was approximately 11 $m\Omega$-cm^2 / 1000 hrs. The ohmic ASR of the second sample, GE13L-Ni-Ni mesh, is also plotted in Figure 3.67. At around 300 hrs, the H_2 was turned off due to unavoidable laboratory maintenance. Therefore, for approximately 40 hrs, the test was idle under dry N_2. Fortunately, the test did not seem to be affected by the brief lack of H_2, aside from a slight increase in ASR (which eventually subsided to former ASR values). Under similar testing conditions, the sample shows very different ASR behavior over time than the GE13L-Ni-GE13L sample. A very slight decrease was actually observed over the course of the test (-0.2 $m\Omega$-cm^2 / 1000 hrs), showing essentially no degradation.

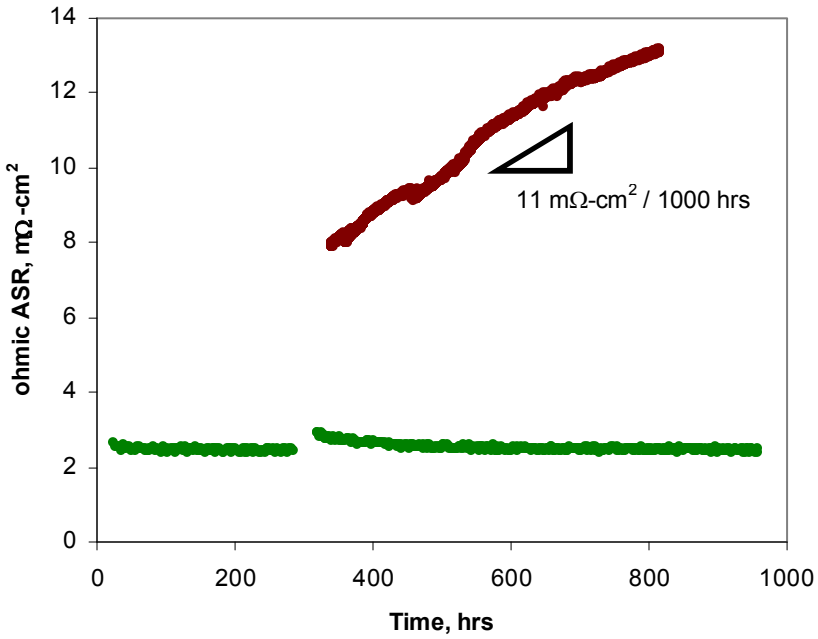

Figure 3.67 The ohmic ASR of the representative anode contact sample plotted as a function of time. The GE13L-Ni-GE13L (red) is plotted with the GE13L-Ni-Ni mesh (green) sample. The samples

were exposed to 6.0 L/min of a mixture of 50% H_2 and 50% H_2O at 800°C, with an applied current density of 0.5 A/cm^2.

The GE13L-Ni-Ni mesh sample demonstrates feasibility of the inherent materials stability in 50% H_2O / H_2 at 800°C. The Ellingham diagram predicts Cr_2O_3 product to form under these conditions; however, it seems that the Cr_2O_3 scale growth does not impact the electrical path in the anode. In contrast, the GE13L-Ni-GE13L sample shows significant degradation. Although repeats should be done to confirm, it suggests that sample geometry has a significant impact on degradation behavior. Because chemical stability was shown to be feasible in the GE13L-Ni-Ni mesh sample, the sample geometry may be enhancing certain degradation mechanisms, such as delamination at the interfaces or Cr_2O_3 growth. Regardless, if metallurgical contact is established between the nickel anode and the ferritic stainless steel current collector, ohmic degradation would expected to be minimal or absent. The geometry of the contact between the interconnect and the anode may play a significant role in the quality of the interface.

3.5.5 Dominant degradation mechanisms and mitigation strategies

3.5.5.1 Strontium chromate reaction phase formation

The formation of strontium chromate has long been identified as a critical degradation mechanism in SOFCs [14,15]. This phase can form via solid state diffusion and subsequent reaction between the thermally grown chromia on the ferritic stainless steel interconnect and the adjacent contacting perovskite layer containing strontium. Additionally, strontium chromate formation can occur via vapor phase transport of chromium species to regions of the SOFC containing perovskites with strontium.

<u>Strontium chromate reaction phase mechanism identification</u>

Two button cell tests were performed in order to understand the impact of strontium chromate formation on performance during electrochemical testing.

GE13L perforated plates without a protective coating were used as cathode side current collectors. The GE13L perforated pates were attached to the cathode side using wet LSC bond paste. The cells were mounted to the six-gun test rig using Aremco cement and reduced at 800°C in H_2-rich atmosphere. Electrochemical performance was measured at 800°C, flowing 200 sccm H_2 with 3% H_2O under 0.7V constant voltage. One cell failed during assembling process, five cells were tested under constant voltage condition for 450 hours, as shown in Figure 3.68. Two cells degraded sharply after the first 50 hours. High ohmic resistance obtained from AC impedance measurement suggested that the current collectors might lose contact with the electrodes during test. The initial

and final power density and the degradation rate up to 1000h are listed in Table 3.11.

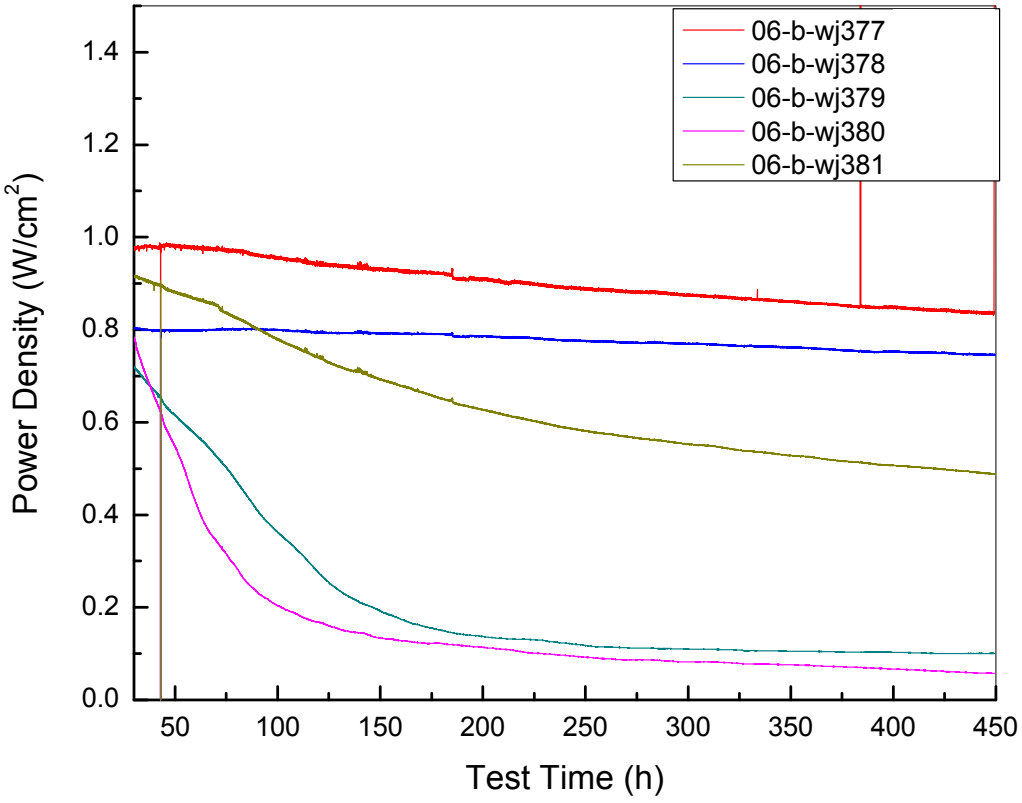

Figure 3.68 Cell performance of uncoated GE13L perforated plate, 800°C, 0.7V for 450h.

Table 3.11 Performance summary of uncoated GE13L perforated plate over 450h.

Sample	Initial PD (W/cm2)	Final PD (W/cm2)	Degradation (%)_1000h
06-b-wj377	0.982	0.837	32.8
06-b-wj378	0.798	0.745	14.8
06-b-wj381	0.88	0.488	99.0

The GE13L/bond paste interface microstructure and corresponding EDS spectra are shown in Figure 3.69. A 3~4 micron thick (Sr, Cr)-rich continuous phase was formed at the LSC/GE13L interface, which is likely the insulating $SrCrO_4$ phase based on previous study.

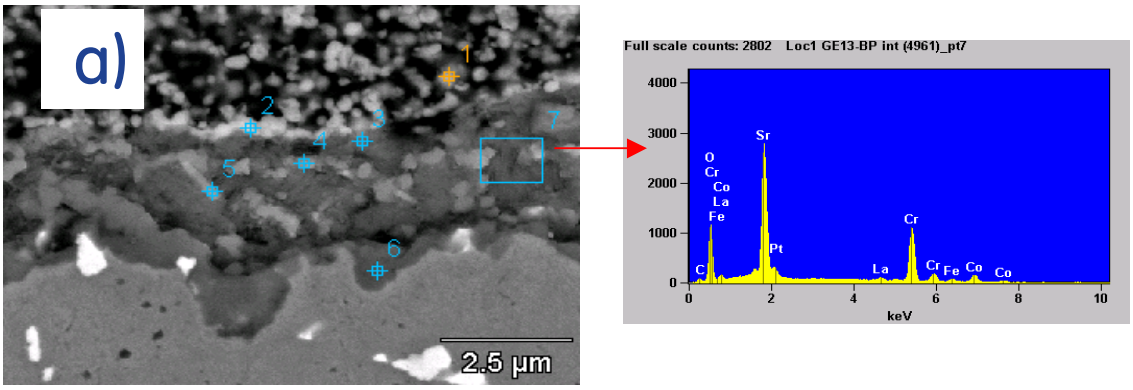

Figure 3.69 Cross-sectional micrographs of LSC bond paste on bare GE13L perforated plate and corresponding EDS spectra after testing at 800°C for 450h.

In summary, the postmortem analyses on this button cell test indicates the conclusion that a dense protective coating on the cathode current collector is critical in order to prevent Cr reaction with the LSC bond paste layer.

Mitigation of strontium chromate formation

Previous work has shown that Cr migration from the interconnect into the cathode-side materials can be greatly reduced when using a $(Mn,Co)_3O_4$ (MCO)-coated interconnect to reduce diffusion and volatilization of Cr species [16,17,18].

It is desirable, then, to examine the interactions of the MCO with both the interconnect and cathode materials. Specific focus areas for this work include reactions between the cathode-side ferritic steel interconnect alloy with the protective MCO coating, and between the MCO coating and the LSC cathode bonding layer.

If the MCO coating is too porous or too thin, a series of reactions are observed involving the chromia scale, the MCO coating and the LSC bond paste. The most egregious of these is $SrCrO_4$ phase formation adjacent to the chromia-MCO interface and well into the MCO coating itself, as evidenced by the TEM results in Figure 3.70. This reaction is facilitated by the interdiffusion of Sr (from the LSC) and Cr (from the chromia scale) through the porous MCO, and is highly undesirable due to its intrinsic resistivity. The density of the MCO coating is actually an important parameter in the long-term stability of the cathode side. A dense, functional coating would ideally prevent 1) oxidation of the interconnect, to minimize resistive chromia scale formation; 2) Cr volatilization, in the form of $CrO_2(OH)_2$, and diffusion from the interconnect to the LSC and LSCF, thus inhibiting chromium poisoning reactions elsewhere in the cathode region; 3) Sr passage from the LSC to the chromia scale, thereby mitigating resistive $SrCrO_4$ formation.

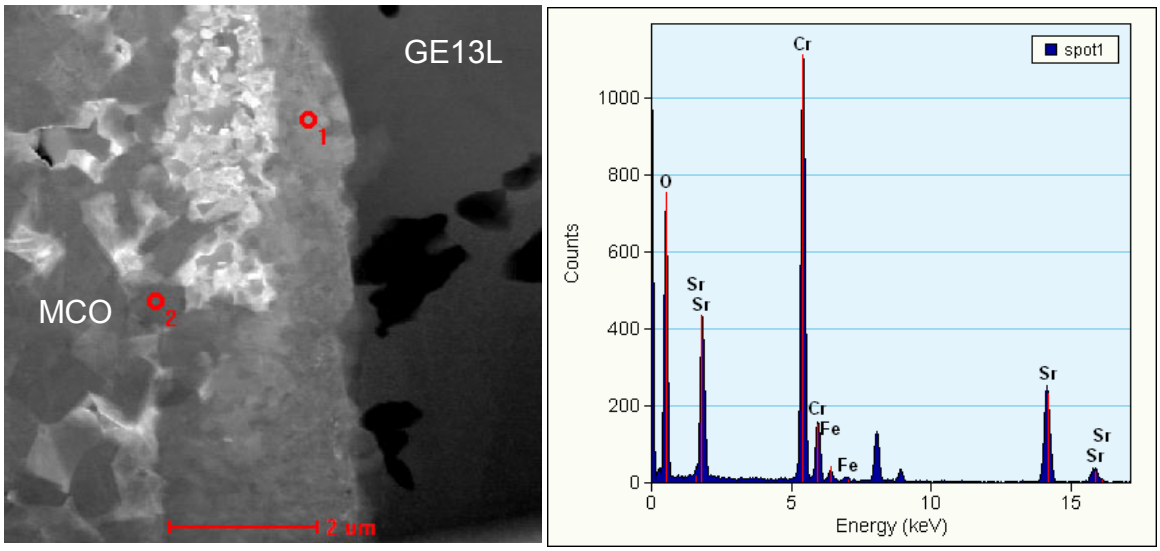

Figure 3.70 (a) Dark-field STEM image showing reaction product formation between MCO coating (left) and GE13 interconnect (right). (b) EDS spectrum from reaction product (spot 1) indicates $SrCrO_4$ formation.

3.5.5.2 Thermally grown silica

Several key requirements for the current collector is that the thermally grown oxide be electrically conductive, the thermal expansion coefficient of the current collector must closely match that of the electrolyte and the current collector material must be low-cost. Hence, ferritic stainless steel with a thermally grown chromia scale is typically selected. However, the formation of thermally grown surface oxides with conductivities less than chromia are highly detrimental. Two such oxides are silica and alumina. In particular, silicon typically is present in steel alloys as a contaminant from the processing and is very difficult to cost-effectively remove.

Silica mechanism identification

TEM studies reveal appreciable (100 nm thick) amorphous SiO_2 scale formation between Ebrite™ interconnect and the chromia scale, as shown in Figure 3.71a. Pockets of SiO_2 are also found between grain boundaries of the chromia scale (Figure 3.71c and d). The formation of a highly insulating phase such as SiO_2, even at 100 nm thickness, is a major concern because of the consequential increase in the ohmic ASR. The insulating SiO_2 scale is believed to form when residual Si impurities in the Ebrite™ (~0.1-0.2 wt%) segregate to the interconnect surface during alloy processing and oxidize to form a thin silica scale. This resistive layer could be minimized if not prevented by eliminating the Si impurity concentration in the base alloy, or by incorporating alloying elements that form stable silicides. Both approaches are being investigated currently. Nonetheless, understanding the tolerance towards Si impurity concentrations is important for

interconnect alloy selection and material specification, as it will ultimately determine if special processing techniques are required to eliminate Si from the melt.

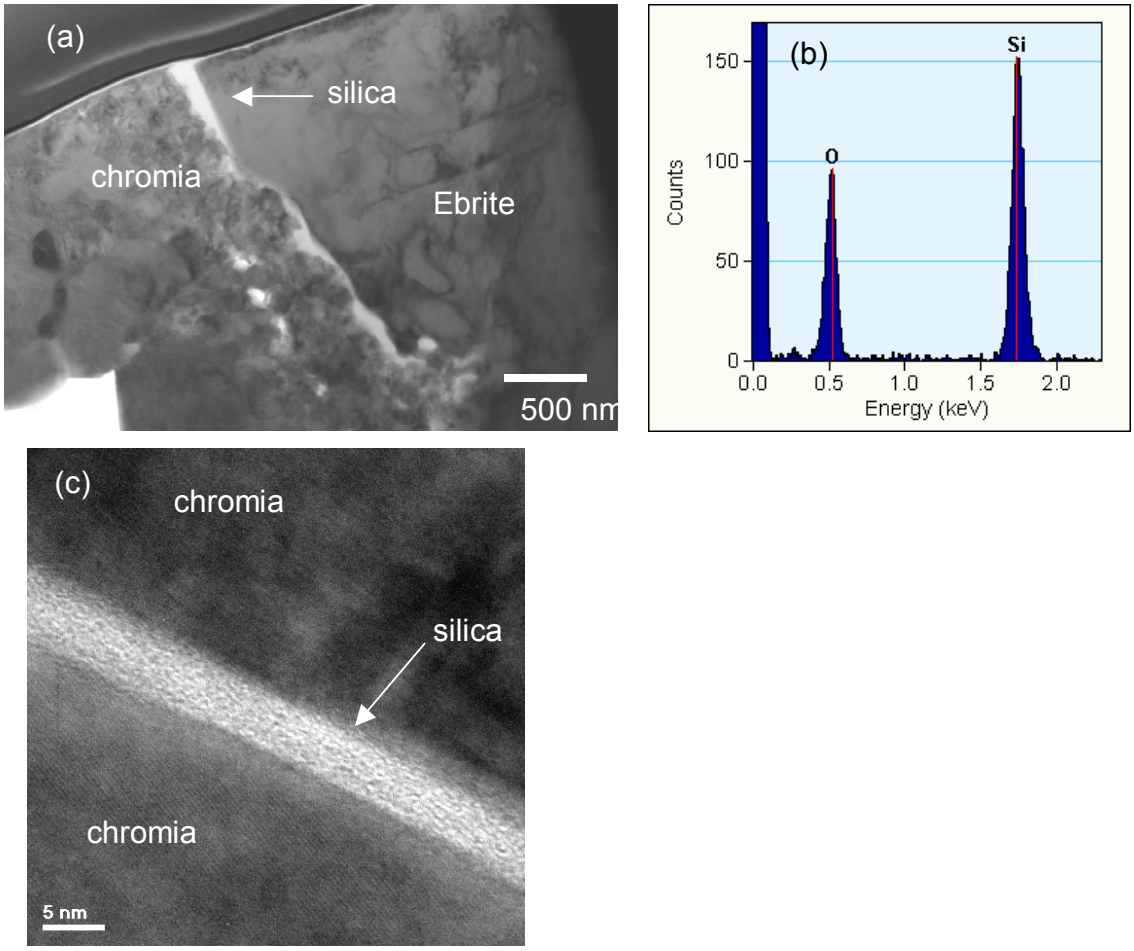

Figure 3.71 (a) Bright-field TEM image shows 50-100 nm thick amorphous silica film (arrowed) between Ebrite interconnect (right) and chromia scale (left). (b) EDS spectrum confirms SiO_2 film composition. (c) Amorphous silica films can also be seen wetting grain boundaries in the polycrystalline chromia scale.

Silica formation mechanism mitigation

From the results presented above, the most logical approach to mitigating the formation of silica at the ferritic stainless steel / chromia interface is to minimize the free silicon content of the alloy. Several different approaches can be envisioned and work is underway under the SECA program to evaluate these approaches.

In the meantime, the GE alloy GE-13L will be used for testing as it was designed with less than 0.02 wt % Si and will therefore not incorporate silica into the thermally grown oxide. The use of E-Brite has been suspended due to the high silicon content of the alloy.

Additionally, the use of AL441HP is promising and will be discussed later in this document.

3.5.5.3 LSCF cathode and LSC cathode bond layer stability

As previously mentioned above, structural related mechanisms, including *in-situ* sintering and coarsening of layers have been identified as potential degradation sources. Structural degradation mechanisms can be caused by the coefficient of thermal expansion (CTE) mismatch between component layers and *in-situ* sintering of the electrode and bond paste layers

Cathode stability mechanism identification

AC impedance spectroscopy (IS) has proven to be useful for identifying mechanism during SOFC operation. IS is most useful for determining ohmic ASR contributions to the total ASR of the SOFC. Polarization ASR can then be determined from the difference of the ohmic and total ASR values. Initial results on both one-inch button cells and large 25 cm^2 SOFCs showed significant performance degradation (> 100mΩ-cm^2/khr) during the life of operation. As mentioned previously, the performance degradation of LSCF cathodes has been a concern in the SOFC community, and therefore was considered as a potential cause for high (and sometimes catastrophic) degradation rates.

One-inch button SOFC tests conducted in early 2007 showed a majority of the samples with very high degradation (>100mΩ-cm^2/khr). Figure 3.72 is an example of a button cell test with high degrading samples, except for one. The cells had LSCF-based cathodes, with LSC based bonding paste to connect to the coated ferritic steel cathode interconnect.

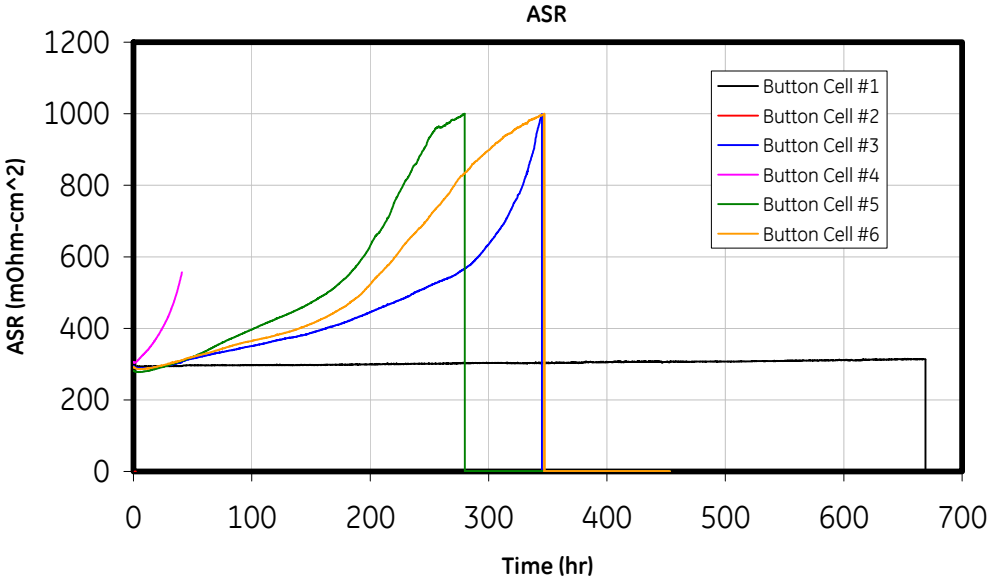

Figure 3.72 Total cell ASR under constant current test condition with MCO coated GE-13L cathode IC.

Cathode instability mitigation

In 2006 a stabilized LSCF-based cathode was used for SOFC performance and degradation testing. Low degradation rates were observed on several cells without catastrophic degradation occurring. A comprehensive study of cathode composition, cathode microstructure evolution over long operation period and the impact on performance was carried out.

A button cell test was operated to look at the stability of a LSCF-based cathode. One-inch diameter super cell bilayers were used for this test. Electrical attachment was made on the cathode side by bonding a $(Mn,Co)_3O_4$ coated, LSC pre-bonded GE-13L perforated plate with LSC bond paste and heat treated in the cell testing rig in-situ at 800°C.

Five cells survived the test as shown in Figure 3.73. All five cells showed consistently low degradation rate (4.5±1.9% per 1000 hour in terms of power density) over the ~600-hour testing period without catastrophic degradation (Figure 3.74). Both ohmic (Figure 3.75) and polarization (Figure 3.76) ASR measured by AC impedance were plotted. All five cells demonstrated gradually increasing ohmic ASR over time while the polarization ASR had a much smaller increase. This is an indication that the performance degradation was largely due to the formation of less-conductive phases, instead of cathode degradation.

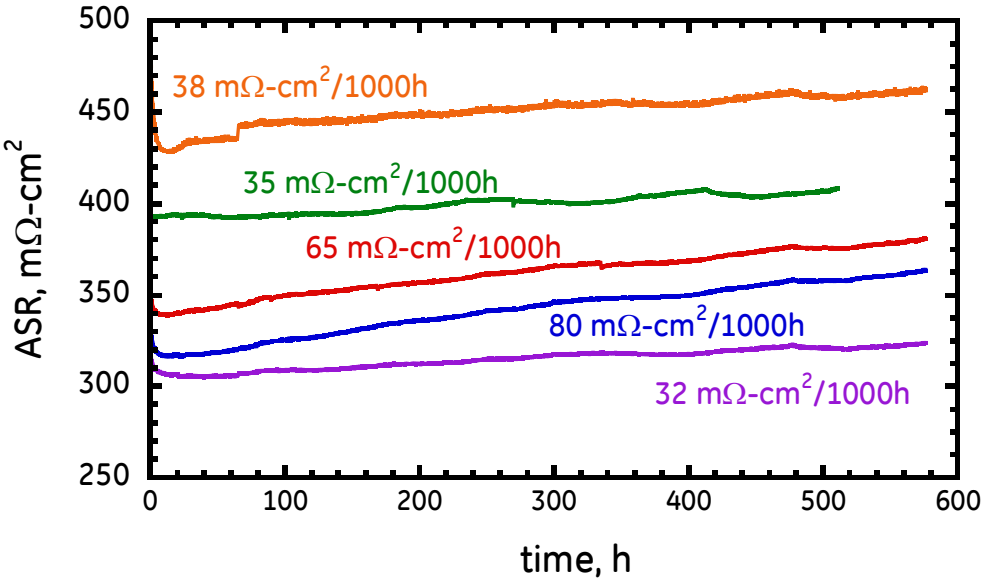

Figure 3.73. ASR evolution during testing with an average degradation rate of 50+/-21 mΩ-cm^2/1000h.

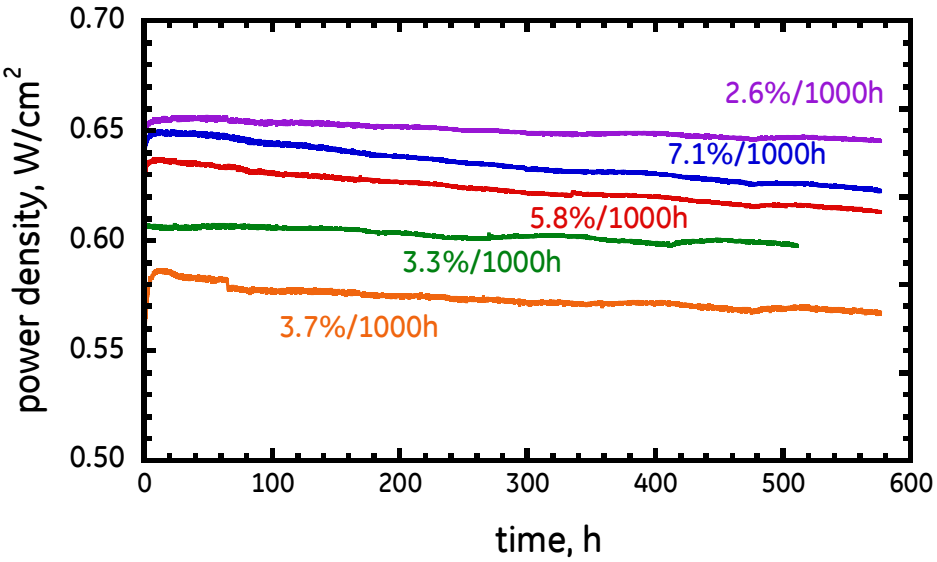

Figure 3.74. Power density evolution during testing with an average degradation rate of 4.5+/-1.9%/1000h.

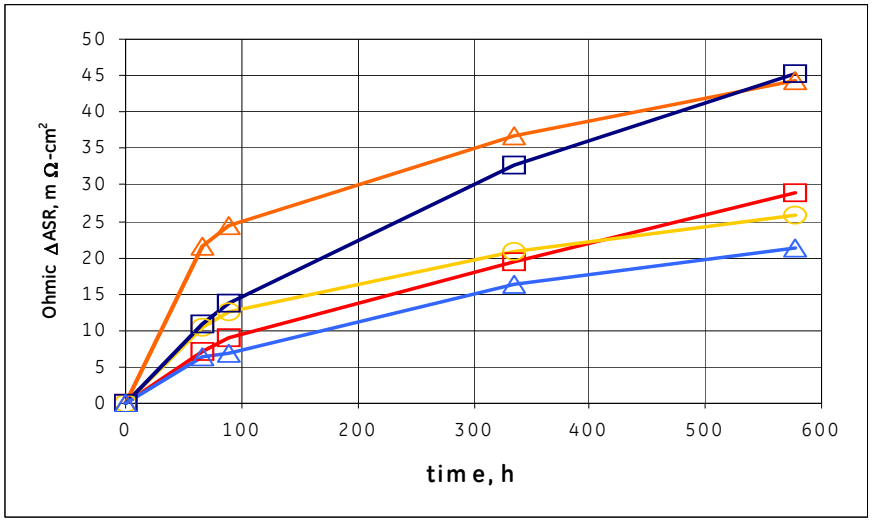

Figure 3.75. Ohmic degradation as a function of time as determined by impedance spectroscopy.

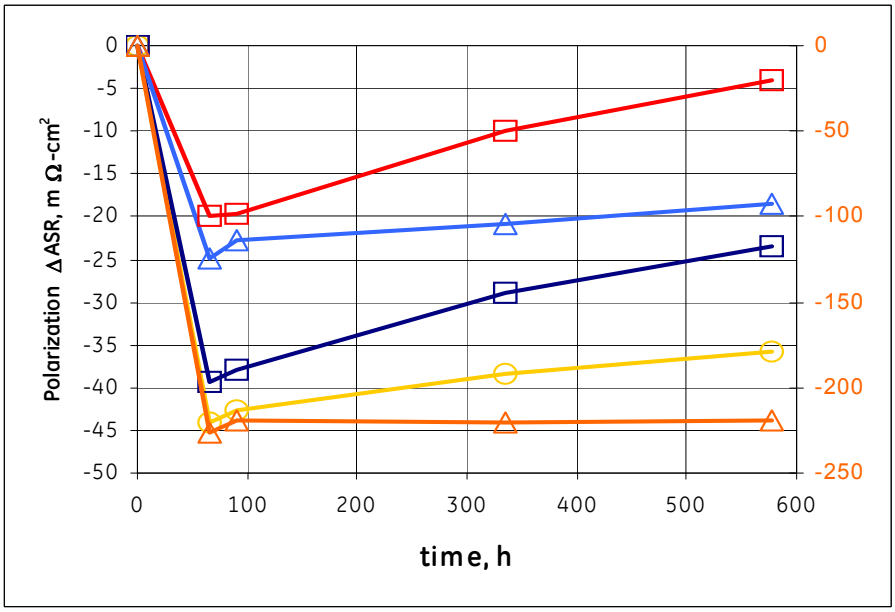

Figure 3.76. Polarization degradation as a function of time as determined by subtracting the ohmic ASR from the total ASR at 0.7V.

The overall conclusion is that the stabilized LSCF-based cathode effectively reduced performance degradation.

3.5.6 Cost reduction and performance evolution

3.5.6.1 Low-cost interconnect alloy

Allegheny Ludlum stainless AL 441HP™ alloy is a heat resisting ferritic grade that provides good oxidation and corrosion resistance for applications like automotive exhaust system components. Ferritic steels are not inherently strong at elevated temperatures, but niobium additions coupled with appropriate solution annealing markedly improve long-time creep rupture strength properties. AL 441HP alloy is dual stabilized with niobium and titanium to provide good weld ductility and resistance to intergranular corrosion in the weld heat affected zone. Table 3.12 shows the nominal composition of this alloy. The cost of E-BRITE® alloy, also from Allegheny Ludlum, specially developed for the interconnect applications in solid oxide fuel cells, is significantly more expensive than 441 HP.

Table 3.12 Nominal composition of Allegheny Ludlum stainless AL 441HP™ alloy

Alloy	Cr	Nb	Ni	Ti	Si	Mn	C	N	P	Fe
441 HP	18	0.5	0.3	0.22	0.34	0.35	0.009	0.014	0.023	Bal.

Figure 3.77 compares the offline ASR measurement results of 441 HP with that of GE-13L and the superior performance of 441 HP is intriguing considering the fact that it also contains Si (~0.34% by weight), which is known to form a silicon oxide layer that degrades the ASR in the case of E-BRITE.

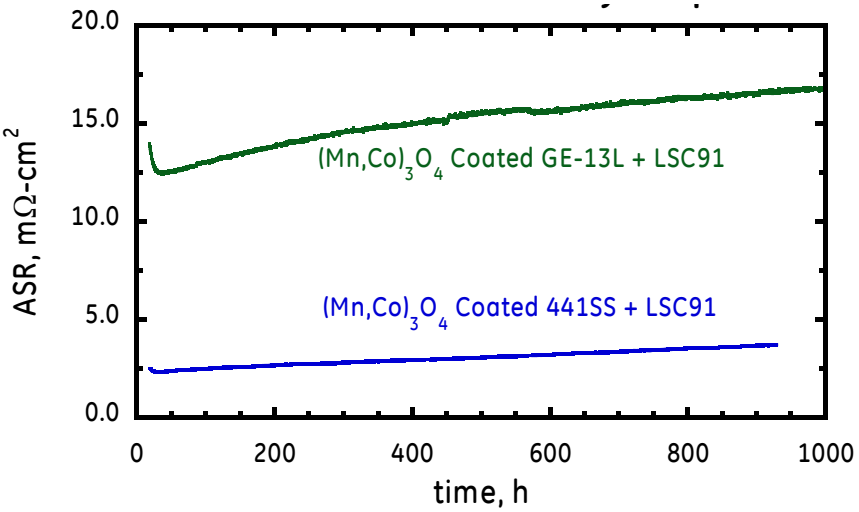

Figure 3.77 Offline ASR measurement results of 441 HP™ and GE-13L.

3.5.6.2 Performance evolution

The improvement of cell performance has not been a primary goal of this program. However, a steady improvement of performance has ensued over the years as shown in Figure 3.78. The increase in performance is attributed to a change in cathodes from LSM to LSCF in 2005 in addition to a growing

experience base that has served to optimize cell construction for both performance and degradation.

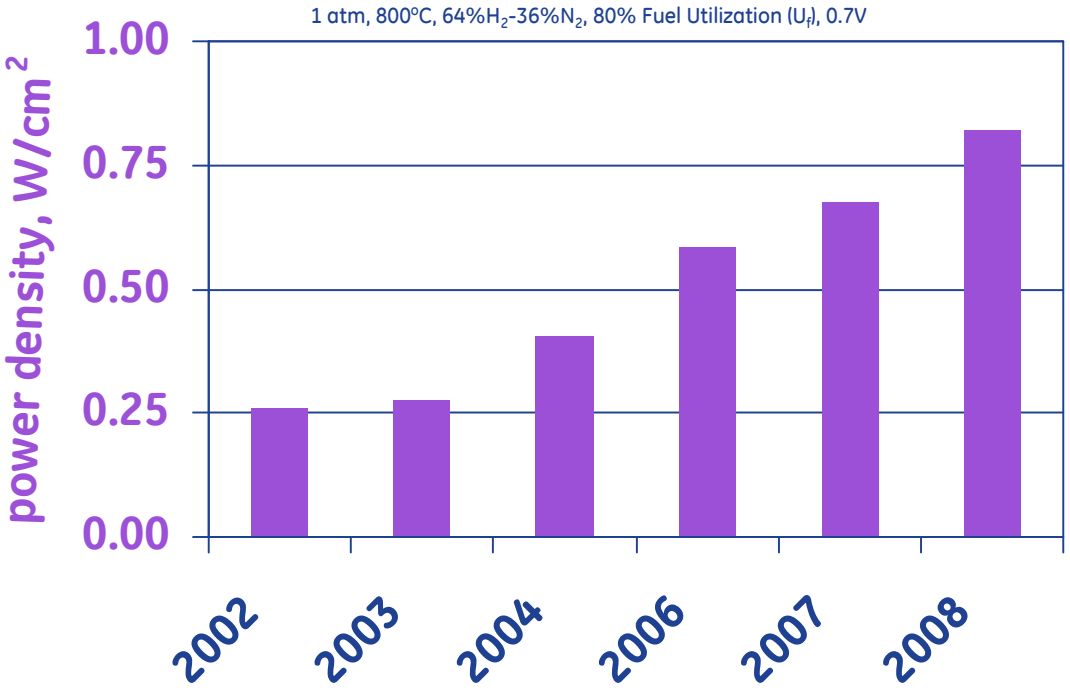

Figure 3.78 Performance evolution of SOFCs at GE Global Research.

3.5.7 Conclusions and future work

3.5.7.1 End of program status

When combined, the degradation mitigation approaches described above are very encouraging. The culmination of these efforts resulted in testing on the 25 cm^2 cell in the ceramic test vehicle. The performance and testing conditions of BTV11 is shown in Figure 3.79. Minor test stand failures affected the performance of the cell around 430 hours and 830 hours, therefore a time average ASR degradation was calculated at 15 $m\Omega\text{-}cm^2$/1000h with a corresponding PD degradation of 2.2%/1000h.

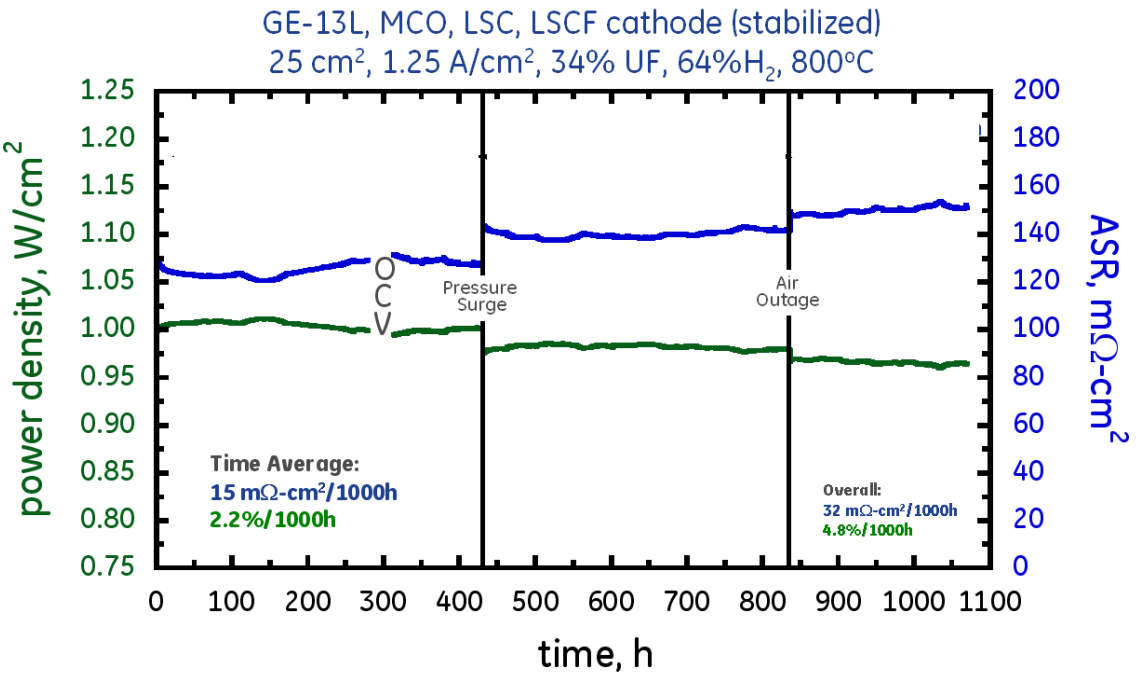

Figure 3.79. Degradation data for BTV11 with stabilized LSCF cathode. Minor test stand failures affected the performance at ~430 and ~830 hours.

However, attempts to repeat the success of BTV11 varied. ASR degradation curves for subsequent cells are plotted in Figure 3.80. The resulting improvement can be seen in BTV13. Though not a repeat of BTV11, initial performance of BTV13 fell in line with the statistical averages. The degradation curve for BTV13 shows a slight slope increase from BTV11 and therefore was terminated at 500 hours to attempt another repeat. BTV14 initial performance was similar to that for BTV13. Though degradation data showed a measurable decrease in slope when compared to BTV13, it was not a true repeat of BTV11.

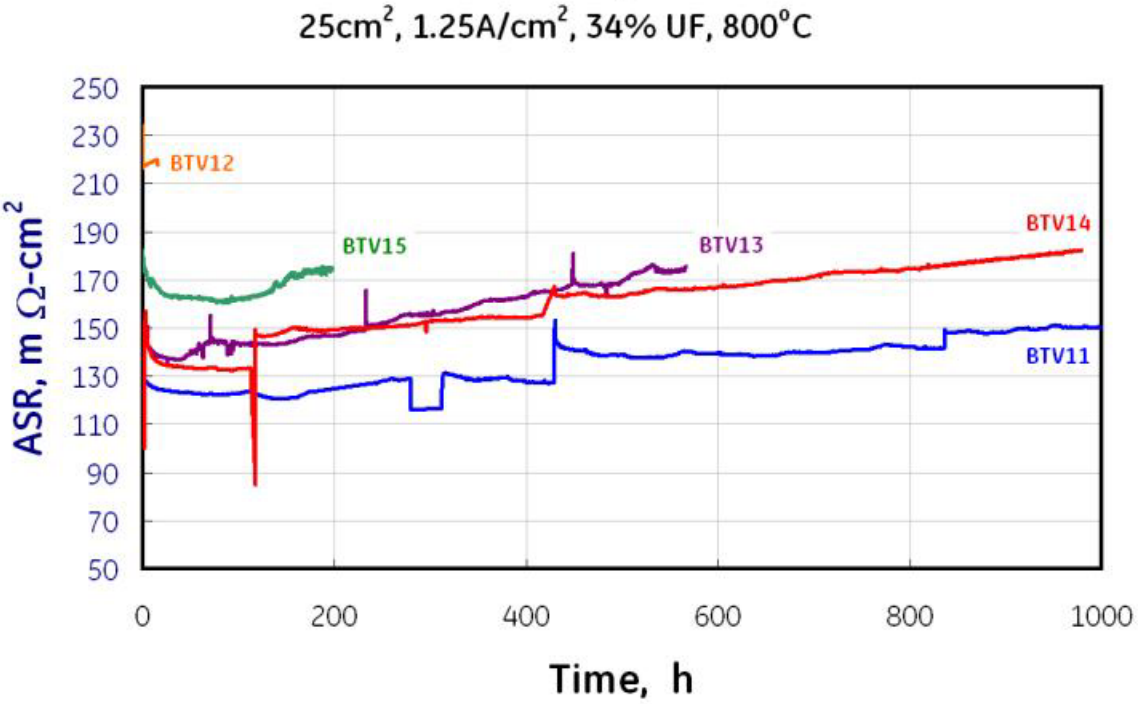

Figure 3.80 Degradation summary for Q1 Browaller cells. All cells were traditional anode supported cells with stabilized LSCF cathodes.

Initial performance shows itself to be highly repeatable. However, degradation performance still suffers from some variation. The current hypothesis as to the failure to directly repeat the degradation results of BTV11 is the failure to obtain a consistent $(Mn,Co)_3O_4$ coating (in terms of thickness, density, and coverage) on the metal substrate.

Though the degradation rate for BTV11 shows a significant reduction, there is room for improvement. Clearly, the interconnect coating is critical.

3.5.7.2 Future work

The mitigation of performance degradation of LSCF cathode-based SOFCs is a challenging, but not insurmountable task. The results from this project indicate a path towards this end. However, several outstanding issues remain:

1. The interconnect chromium barrier coatings need to be further evaluated and optimized, with focus on $(Mn,Co)_3O_4$ spinel, for thin and dense coatings to mitigate the well-known chromium poisoning degradation mechanism.

2. Predictive modeling will be required to estimate performance at times not readily achievable during laboratory testing. These models must

incorporate the sintering kinetics of the porous structures in addition to the mass transport of chromium into the cathode. Detailed knowledge of the active degradation mechanisms will need to be known. Significant effort to experimentally determine the appropriate data will be required.

3. Degradation mechanisms at the stack level must be identified and mitigated. In addition, a significant amount of effort will need to be dedicated to the engineering of the assembly of the cells to ensure low degradation interfaces.

4 REFERENCES

1 Rigdon, R. et al, GE Energy and Bechtel's IGCC Reference Plant Offering, presented at the Gasification Technologies Council Conference, October 2005

2 S. Companari and P. Lora, 2004, Fuel Cells, 2005, 5, No1

3 Y.Teraoka, T.Nobunaga, K.Okamoto, N.Miura, N.Yamazoe, Solid State Ionics 48 (1991) 207

4 L.W.Tai, M.M.Nasrallah, H.U.Anderson, D.M.Sparlin, S.R.Sehlin, Solid State Ionics 76 (1995) 259

5 W.J.Quadakkers, J.P.Abellan, V.Shemet, L.Singheiser, "Metallic Interconnectors for Solid Oxide Fuel Cells- A Review" 2003

6 J.Guan, Y.Liu, P.Lamber, S.Zecevic, S.Taylor, "Evaluation of Performance Degradation of Solid Oxide Fuel Cell Modules and Short Stacks", GE report 2007GRC508

7 H.Nabielek, K.Hilpert, E.Konysheva, F.Tietz, I.C.Vinke, E.Wessel, M.Zahid, "Correlation between chromium Evaporation from SOFC Ferritic Steel Interconnects and Cell Degradation", P1003-Nabielek

8 SECA Coal-Based System Program Quarterly Progress Report, Jul-Sep 2007

9 K. Hilpert, D. Das, M. Miller, D.H. Peck and R. Weiss, J. Electroch. Soc., 143, 3462 (1996)

10 Y. Matsuzaki and I. Yasuda, J. Electrochem. Soc., 148, A126 (2001)

11 M. Stanislowski,z E. Wessel, K. Hilpert, T. Markus, and L. Singheiser, J. Electrochem. Soc., 154, A295 (2007)

12 Z. Yang, G. Xia and J.W. Stevenson, J. Electrochem. Soc., 8, A168 (2005)

13 Z. Yang, X. Li, G.D. Maupin, P. Singh, S.P. Simmer, J.W. Stevenson, G. Xia and X. Zhou, "Properties of (Mn,Co)3O4 spinel protection layers for SOFC interconnects," submitted (2007)

14 Kofstad P, Bredesen R. High temperature corrosion in SOFC environments. Solid State Ionics 1992;52:69.

15 Simner SP, Hardy JS, Stevenson JW. Sintering and Properties of Mixed Lanthanide Chromites. Journal of The Electrochemical Society 2001;148:A351.

16 Larring and Norby, "Spinel and Perovskite Functional Layers Between Plansee Metallic Interconnect (Cr-5 wt % Fe-1 wt % Y_2O_3) and Ceramic $(La_{0.85}Sr_{0.15})_{0.91}MnO_3$ Cathode Materials for Solid Oxide Fuel Cells," *Journal of the Electrochemical Society*, **147** 3251 (2000).

17 Chen, Hui, Jacobson, Visco, and De Jonghe, "Protective Coating on Stainless Steel Interconnect for SOFCs: Oxidation Kinetics and Electrical Properties," *Solid State Ionics*, **176** 425 (2005).

18 Yang, Xia and Stevenson, "Thermal Growth and Performance of Manganese Cobaltite Spinel Protection Layers on Ferritic Stainless Steel SOFC Interconnects," *Journal of the Electrochemical Society*, **152** A1896 (2005).